The influence of oxygen vacancies on domain patterns in ferroelectric perovskites

Thesis by

Yu Xiao

In Partial Fulfillment of the Requirements

for the Degree of

Doctor of Philosophy

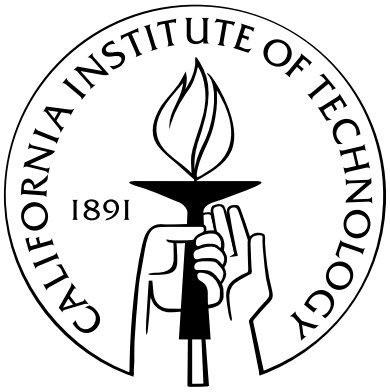

California Institute of Technology

Pasadena, California

2004

(Defended September 29th, 2004)

To my dear grandmother

Acknowledgements

I take this opportunity to thank all the people who have helped me and who continue to inspire me.

My advisor, Kaushik Bhattacharya, is the most influential person in my academic life. He has guided me through the academic challenges and supported me in every aspect of my research and professional endeavors. He seems to have the magic power to grasp the essentials and make complicated things simple. He has also taught me to aim high, to be persevering, and above all, to embrace scientific challenges with passion and enthusiasm. I thank him for his insight, guidance and caring support, and for so much I have learned from him. I shall always look up to him for inspiration.

I am truly grateful to Professor Jim Knowles, who has shown an avid interest in my work and guided me patiently at the very beginning of my academic adventure. I am also deeply indebted to Professor Michael Ortiz and Professor Guruswami Ravichandran for their immense help during the course of my PhD work. The computational mechanics class I took from Professor Ortiz is probably the toughest class I have ever taken. However, it prepared me well to carry the simulation in my own work, and is worth every bit of effort I put into. Professor Ravichandran has always been there for me when I needed help, offering me experienced advice with dedication. I will never forget his kindness and encouragement. I am also grateful to Professor David Goodwin and Professor Nadia Lapusta for serving in my thesis committee and for their constructive comments. I also want to thank Professor Vivek Shenoy for clarifying many questions when I first started this work. His work with Kaushik has provided the starting point for this thesis.

Sincere appreciation is extended to Yi-chung Shu and Jiangyu Li for their constant interests in my work and their invaluable friendships over the years. I also thank Gal deBotton for discussing and reviewing early versions of this thesis, and for his generous advice and encouragement. Many thanks are also due to Michel Perez for sharing his

expertise in diffusion, Prashant Purohit in mechanics, and Michel Tanguay in simulation and other technical issues.

I thank all the members in the ferroelectric group for showing me different aspects in different disciplines. Especially, I want to thank Arash Yavari, Doron Shilo, Qingsong Zhang, Rongjing Zhang and Wei Zhang. The collaboration with them has been very enjoyable and fruitful.

My thanks also go to the current and former members in Kaushik's group, with whom I have fond memories and from whom I have learned much and received a lot of help. Arash, Amir, Alex, Isaac, Kaushik D, Lixiu, Patrick, Prashant and Sam, thank you!

I also want to thank my friends, Jing, Pauline, Ran, Fuling, Sijia, Jun, Ying, Ming, and Qing, for sharing my joy and sadness, and offering instant help whenever needed. I treasure every minute I have spent with them. As to little Cathy, Vivian, Tianxing and Shuangshuang, thank you all for showing me the vitality of new life and bringing me so much joy and love.

Finally, I would like to give my special thanks to my family for their unconditional love and for always believing in me. I am especially grateful to my husband Hui, who has been my best friend, my 24/7 tech support, and above all, my source of happiness. I am lucky to have him as husband.

Abstract

This thesis investigates the role of oxygen vacancies in determining ferroelectric properties and domain patterns of ferroelectric perovskites. Being non-polar (paraelectric) above their Curie temperature but spontaneously polarized (ferroelectric) below it, ferroelectric perovskites offer a tantalizing potential for applications: large actuation through domain switching and memory storage via switchable electric polarization. Oxygen vacancies, commonly present and mobile at high temperature, are the primary defects and thus play a central role in these applications.

We develop a model that combines the ferroelectric and semiconducting nature of ferroelectric perovskites. Oxygen vacancies act as n-type dopants and thus affect the semiconducting properties. We show that the ferroelectric and semiconducting features interact and lead to the formation of depletion layers near the electrodes and double layers at the 90° domain walls. We find a potential drop across 90° domain walls even in a perfect crystal. This potential drop marks the essential difference between a 90° and a 180° domain wall, drives the formation of a space charge double layer in a doped crystal, promotes electronic charge injection and trapping, and leads to the redistribution of oxygen vacancies at 90° domain walls. The rearrangement of oxygen vacancies near 90° domain walls may form a basis for domain memory and provides a potentially new mechanism for large electrostriction.

We also rigorously justify the continuum theory by calculating the Coulomb energy of a spontaneously polarized solid starting from a periodic distribution of charges based on the classical interpretation of ferroelectrics and with a definite choice of polarization per unit cell. We prove that in the limit where the size of the body is large compared to the unit cell, the energy of Coulombic interactions may be approximated by a sum of a local part and a nonlocal part. The local part depends on the lattice structure, but is different from the Lorentz formula for a lattice of dipoles. The nonlocal part is identical to the Lorentz formula.

Contents

List of Figures

Chapter 1

Introduction

Ferroelectric ceramics have long been used as sensors and actuators for their piezoelectric properties. They have remained the mainstay of solid-state actuators for their linear, high-frequency, and low-hysteresis characteristics. However, the strain and displacement generated by these actuators are usually small, limited to a maximum strain of 0.15% (Park and Shrout, 1997). This has led to some clever designs through which relatively large displacement can be generated. One example is the RAINBOW (Reduced and Internally Biased Oxide Wafer) actuator: a bending mode actuator comprised of an active (piezoelectric) and a passive (paraelectric) layer obtained by selectively reducing oxygen from one side of the otherwise piezoelectric material. However, this increased displacement usually comes at the expense of force, and despite ingenious designs, current piezoelectric actuators are inherently limited.

It has recently been recognized that large strain actuation can be achieved through electrostriction in ferroelectric single crystals. Park and Shrout (1997) have reported an ultrahigh strain up to 1.7% in relaxor based ferroelectric single crystals like PMN-PT. It was believed that PMN-PT lies near its morphotropic phase boundary (MPB) between rhombohedral and tetragonal phases. Under strong electric field, a rhombohedral to tetragonal phase transition is induced and an ultra high strain with minimum hysteresis is obtained*.

Another way to achieve large actuation in ferroelectric single crystals was proposed by Shu and Bhattacharya (2001) and it exploits domain switching via suitable electromechanical loading. A ferroelctric crystal is non-polar (paraelectric) above its Curie temperature, but spontaneously polarized (ferroelectric) below the Curie temperature. Along with the

*Recent studies show that the high actuation generated by relaxor ferroelectrics may involve complex nanosclale structures: local displacive disorder, short-range compositional order have been revealed (Egami et al., 1997, 1998).

spontaneous polarization, large distortion also occurs. Typically, there is also a reduction of crystal symmetry at Curie temperature. This gives rise to symmetry-related variants: crystallographically and energetically identical states that are oriented differently with respect to the parent non-poplar state. These variants can coexist as domains separated by domain walls. As an example, barium titanate ($BaTiO_3$), the most extensively investigated ferroelectric material, is cubic and non-polar above its Curie temperature (120°C), and is tetragonal and spontaneously polarized along $\langle 100 \rangle$ direction at room temperature. Since it arises from cubic phase at high temperature, it can be polarized and distorted along any one of its six "pseudo-cubic" directions at room temperature. We thus have six variants of the polarized state, and they form patterns involving 180^o and 90^o domain walls.

Since symmetry-related variants are energy-equivalent, it is possible to switch one domain to another by suitable electromechanical loading. Such a switch is accompanied by a change in distortion and can form the basis for large actuation. Shu and Bhattacharya (2001) showed that such a program was viable through a nucleation and growth mechanism with an electromechanical loading consisting of a constant compressive stress and bipolar cyclic electric field. Briefly, the stress favors (biases) one variant while the field favors another. So the cyclic electric field in the presence of stress gives rise to repeatable switching. Strain as high as 1% in $BaTiO_3$ and 6% in $PbTiO_3$ was predicted, and has been experimentally validated by Burcsu et al. (2000, 2004) in $BaTiO_3$.

Apart from demonstrating large electrostriction, the experiments of Burcsu et al. (2000, 2004) produced two noteworthy observations. First, the resistance of the ferroelectric crystal to dielectric breakdown (where it changes from an insulator to a conductor) depended critically on the electrodes. Specimens with silver paste broke down after a couple of cycles whereas specimens with platinum electrodes underwent numerous cycles with no breakdown. This observation compels one to reexamine the classical treatment of ferroelectrics as insulating dielectrics, and provides a motivation for this thesis. Second, the experiment demonstrated significant hysteresis. This aspect was further studied by Zhang (2004b) through detailed observations of the inner-loops. The established phase field models (e.g., Ahluwalia and Cao, 1991; Zhang and Bhattacharya, 2004a,b) reproduce the overall hysteretic response, but are unable to capture all the details. The experiments display a pronounced stick-slip (rate independent) character, but the simulations are more smooth (rate dependent). This shows that defects and pinning play an important role in ferroelectrics. Indeed, oxygen

vacancies are very common defects in ferroelectric perovskites and they have relatively high mobility and interesting electrical properties. Shilo et al. (2004) recently studied the domain wall structure using atomic force microscopy. An interesting finding is the strong evidence of defect trapping at 90° domain walls in lead titanate ($PbTiO_3$). This provides yet another motivation for the work described in this thesis.

The role of defects has also been highlighted by the recent experiments of Ren (2004) that promise another mechanism of large strain actuation. In Ren's experiment, a $BaTiO_3$ single crystal which contains a small amount of Fe^{3+} and O^{2-} vacancies was cooled down through the Curie temperature (128°C) to form a fine pattern of 90° and 180° domains. Before cooling down to the room temperature, the specimen was aged at 80°C for five days. At room temperature, when the aged specimen was subjected to a bipolar electric field, it showed an interesting double P-E (polarization vs. electric field) hysteresis loop, instead of the usual single loop. Consequently, large actuation was generated even by a monopolar field without any mechanical loading. In order to explain the experimental results, Ren argues that during the aging process, "defect dipoles" align with the spontaneous polarization in each unit cell through oxygen vacancy diffusion in order to reach the energy minimum state. In other words, the material develops a memory for the domain pattern during aging via oxygen diffusion. When a large enough electric field is applied to the aged and cooled specimen, the spontaneous polarization aligns with the external field through 90° domain switching. This switching is accompanied by large strain. However, the defect dipoles remain unchanged since oxygen vacancy diffusion is limited at room temperature. When the external applied field is removed, the specimen undergoes a reverse 90° domain switch so that the defect dipoles and the spontaneous polarization can align again and restore the original domain pattern. This experimental observation reported by Ren (2004) is very promising, since it may lead to a wide range of applications where mechanical loading is prohibited. Providing a concrete mechanism to the observations of Ren (2004) provides further motivation for this thesis.

Besides the large actuation promised by ferroelectric single crystals, an even more promising application for ferroelectric material is the potential use of ferroelectric thin films in non-volatile or high density memory applications. This, however, is impeded by ferroelectric fatigue and dielectric breakdown. Ferroelectric fatigue is defined as the loss of switchable polarization under bipolar switchings, and has received considerable attention in

recent years. Various interlinked mechanisms have been postulated based on substantial experimental data, but a definitive understanding is yet to emerge (Scott, 2000; Damjanovic, 1998; Tagantsev et al., 2001; Shaw et al., 2000).

Interestingly, lead zirconate titanate (PZT) with conductive oxide electrodes, YBCO/ PZT/YBCO (Ramesh et al., 1992), and strontium bismuth tantalate with platinum electrodes, Pt/SBT/Pt (De Araujo et al., 1995), make almost fatigue-free capacitors compared to the pronounced fatigue in Pt/PZT/Pt capacitors. The fact that the use of oxide electrodes in PZT dramatically improves its performance, and that SBT which has a complicated oxide-perovskite layer structure has low fatigue suggests a link between oxygen vacancies and fatigue. In addition, oxygen vacancies are indeed the most mobile ionic defects in perovskite materials, and oxygen vacancy redistribution during polarization fatigue has also been reported (Scott et al., 1991; Sanchez et al., 1991). However, many experimental results also show that electronic charge injection may play an equally or even more important role in ferroelectric fatigue. However, these two mechanisms, electronic and ionic charges (oxygen vacancy) trapping, are yet to be fully developed as the very reasons for their occurrence and their relations are still debated (Warren et al., 1994, 1995; Gütter et al., 1995; Cillessen et al., 1997; Du and Chen, 1998; Nagaraj et al., 2001; Nuffer et al., 2001). Most explanations are essentially phenomenological; a systematic and quantitative model is still missing.

Motivated by all these reasons, this thesis aims at systematically investigating the role of oxygen vacancies in determining ferroelectric properties, domain patterns, electric fatigue and field-induced actuation in ferroelectric perovskites. The key step – and departure from prior work – is to treat ferroelectric perovskites as polarizable semiconducting solids through the introduction of space charges. It is well known that ferroelectric perovskites are wide band-gap semiconductors (Scott et al., 1999; Moulson and Herbert, 2003): the band-gap for $BaTiO_3$ is about 3.0 eV, and $PbZr_{0.40}Ti_{0.60}O_3$ is 3.4 eV[†]. Oxygen vacancies are donors or n-type dopants that are mobile at high temperature. Yet virtually all continuum treatments of ferroelectric materials (e.g., Devonshire, 1954; Ahluwalia and Cao, 1991, 2001; Zhang and Bhattacharya, 2004a,b) assume them to be dielectrics or insulators. There are a few recent exceptions: however, they either treat the polarization distribution as frozen and calculate

[†]Unlike typical semiconductors such as silicon and germanium, the precise band structures for oxide semiconductors are hard to get because sufficiently precise physical and chemical characterization of the materials is often extremely difficult (Moulson and Herbert, 2003).

the space charges (Watanabe and Sawamura, 1997; Watanabe, 1998a,b,c) or they treat the space charges as frozen and calculate the polarization (Tagantsev et al., 1995b; Bratkovsky and Levanyuk, 2000). However, the polarization and space charges (i.e., the ferroelectric and semiconducting aspects of ferroelectric perovskites) interact through the electrostatic potential. Therefore they require an uniform treatment, and this thesis is the first work to do so.

This unified model provides us with unique insights into the behavior of ferroelectric perovskites. It allows us to study the space charge distribution near electrodes and near domain walls. It points out differences between 180^o and 90^o domain walls. It provides an insight into the redistribution of dopants including oxygen vacancies. And through all of these, it provides us a new understanding to the practical problems of fatigue and domain wall pinning.

The thesis is organized into seven chapters. In Chapter 2, we review some basic properties of ferroelectric perovskites with $BaTiO_3$ as a typical example. For readers who are not familiar with semiconductors, we also introduce some basic concepts.

We set up the continuum theory for ferroelectric semiconducting solids in Chapter 3. Built on the preliminary ideas of Shenoy and Bhattacharya (2004), and strongly influenced by the fundamental work of Toupin (1956) and Brown (1966), the theoretical framework presented in this chapter, is an extension to the one proposed by Shu and Bhattacharya (2001), and also those used in the study of ferromagnetic shape-memory alloys (James, 2002; James and Kinderlehrer, 1990; DeSimone and Podio-Guidugli, 1996). The most significant difference is that we now treat ferroelectric perovskites as polarizable semiconducting solids doped with oxygen vacancies. We construct a detailed kinematic description of such a solid. We then calculate the dissipation associated with any process that respects balance laws, and this allows us to identify the dynamic (force) quantities conjugate to the kinematic variables. Combined with constitutive equations, we obtain the governing equations. These are summarized in Section 3.5, along with a specialization to a number of simplified circumstances.

Chapters 4 and 5 employ these equations to model a ferroelectric film/slab with shorted top and bottom electrodes, specifically, to a $Pt/BaTiO_3/Pt$ structure. The normalization of system equations and the selection of material parameters are covered in Section 4.1; the equations for the diffusion of oxygen vacancies are covered in Section 4.2. Through finite

element simulation, we obtain full field solutions in Section 5.1.1 for perfect crystals and in Section 5.1.2 for crystals doped with oxygen vacancies. Besides the detailed polarization and stress/strain profiles, the solutions show the formation of depletion layers near electrodes and the complex electrical state prevailing near 90^o domain walls. These two issues are investigated further in Sections 5.2 and 5.3 through detailed numerical and analytical studies of simplified one-dimensional models. The most important finding is the potential drop across 90^o domain walls even in a perfect crystal, which marks the essential difference between 90^o domain walls and 180^o domain walls. This potential drop drives the formation of a space charge double layer in a doped crystal, promotes electronic charge injection and trapping and the accumulation of oxygen vacancies at the domain walls.

Chapter 6 is devoted to the Coulomb energy generated by a spontaneously polarized solid. Starting from a periodic distribution of charges based on the classical interpretation of the ferroelectric and with a definite choice of polarization per unit cell, we rigorously justify the continuum theory of Chapter 3. The main result is a theorem which states that in the limit where the size of the body is large compared to the unit cell, the energy of Coulombic interactions can be approximated by a sum of a local part and a nonlocal part. The local part depends on the lattice structure, but is different from the Lorentz formula for a lattice of dipoles. However, because it can be incorporated into a local energy density functional, we do not see the explicit manifestation of this difference. The nonlocal part is identical to the Lorentz formula.

This thesis is by no means the end of the story. There are still numerous interesting and open problems surrounding ferroelectric perovskites, both in the theoretical and in the application aspects. In Chapter 7, we discuss some of the possible directions. In fact, encountering new problems and new phenomena daily is the most pleasing and exciting aspect of working on this thesis, and makes the long journey a truly worthy one.

Chapter 2

Background

2.1 Ferroelectricity in Perovskites

Barium titanate ($BaTiO_3$), which we have discussed briefly in Chapter 1, is only one member of a large group of compounds called the perovskite family, of which the parent member is the mineral $CaTiO_3$, called perovskite (Jona and Shirane, 1993). The general formula of these compounds is ABO_3, where A is a monovalent, divalent or trivalent metal and B a pentavalent, tetravelent or trivalent element, respectively. The ABO_3 formula implies that perovskite compounds are double oxides. Besides $BaTiO_3$, perovskites like lead titanate ($PbTiO_3$), potassium niobate ($KNbO_3$) and potassium tantalate ($KTaO_3$) also show significant ferroelectric activity. In addition, many of their solid solutions are also ferroelectrics. A widely used example is PZT, a solid solution of lead titanate ($PbTiO_3$) and lead zirconate ($PbZrO_3$). It is $\langle 100 \rangle$ polarized tetragonal in Ti-rich region and $\langle 111 \rangle$ polarized rhombohedral in Zr-rich region.

In order to understand the origin of ferroelectricity exhibited by ferroelectric perovskites, let us take a look of the prototypical ferroelectric perovskite, $BaTiO_3$. Fig. 2.1 shows various crystalline phases of $BaTiO_3$ at different temperatures: cubic and non-polar above its Curie temperature (120°C), $\langle 100 \rangle$ polarized tetragonal at room temperature, $\langle 110 \rangle$ polarized orthorhombic under 5°C, and $\langle 111 \rangle$ polarized rhombohedral below -90°C. Fig. 2.2 shows the crystal structures of $BaTiO_3$ in their cubic and tetragonal phase. As shown schematically in the figure, when $BaTiO_3$ is cooled down through the Curie temperature, the Ba and Ti sublattices shift upward relatively to the negatively charged oxygens, generating a polarization (net dipole moment per unit volume) of $0.26 C/m^2$. This shift breaks the cubic symmetry into a tetragonal phase and results six symmetry-related and crystallographically-equivalent

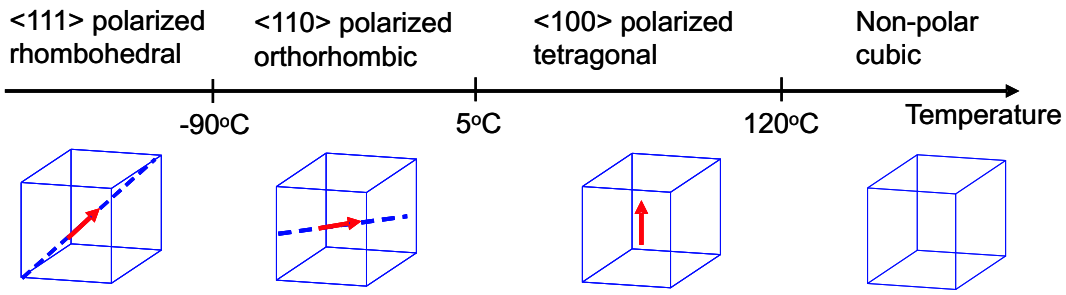

Figure 2.1: Various crystalline phases of $BaTiO_3$.

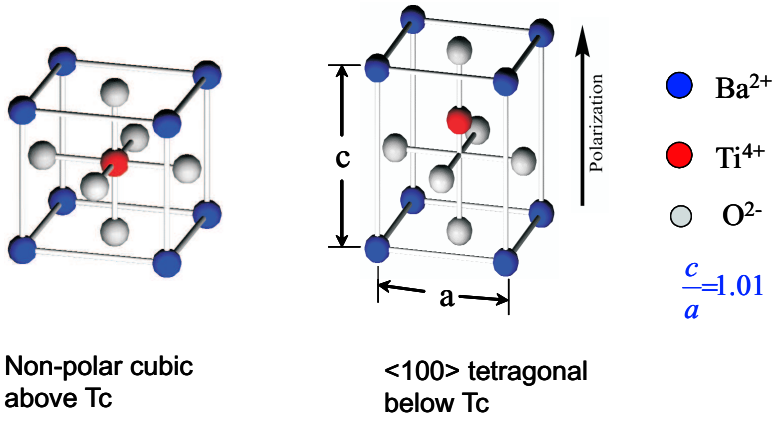

Figure 2.2: Crystal structures of $BaTiO_3$ in their cubic and tetragonal phases.

variants, as shown in Fig. 2.3(a).

If we choose the cubic non-polar phase at Curie temperature as the reference configuration, we can represent the different states of crystals by $(\mathbf{F}, \mathbf{p})$ where $\mathbf{F}$ is the deformation gradient and $\mathbf{p}$ the polarization. According to the polar decomposition theorem, we can always decompose $\mathbf{F}$ as a stretch/shear $\mathbf{U}$ followed by a rotation $\mathbf{Q}$, i.e, $\mathbf{F} = \mathbf{QU}$ where $\mathbf{U}$ being positive-definite and symmetric, is called the *transformation matrix*. This decomposition is unique. Thus, the cubic phase of $BaTiO_3$ is represented by $(\mathbf{I}, 0)$, and the six variants of the tetragonal phase are represented by $(\mathbf{U}_i, \pm\mathbf{p}_i)$, $i = 1, 2, 3$ with

$$\mathbf{U}_1 = \begin{pmatrix} \beta & 0 & 0 \\ 0 & \alpha & 0 \\ 0 & 0 & \alpha \end{pmatrix} \quad , \mathbf{U}_2 = \begin{pmatrix} \alpha & 0 & 0 \\ 0 & \beta & 0 \\ 0 & 0 & \alpha \end{pmatrix} \quad , \mathbf{U}_3 = \begin{pmatrix} \alpha & 0 & 0 \\ 0 & \alpha & 0 \\ 0 & 0 & \beta \end{pmatrix} \tag{2.1}$$

and

$$\mathbf{p}_1 = p_0\{1, 0, 0\}, \quad \mathbf{p}_2 = p_0\{0, 1, 0\}, \quad \mathbf{p}_3 = p_0\{0, 0, 1\}. \tag{2.2}$$

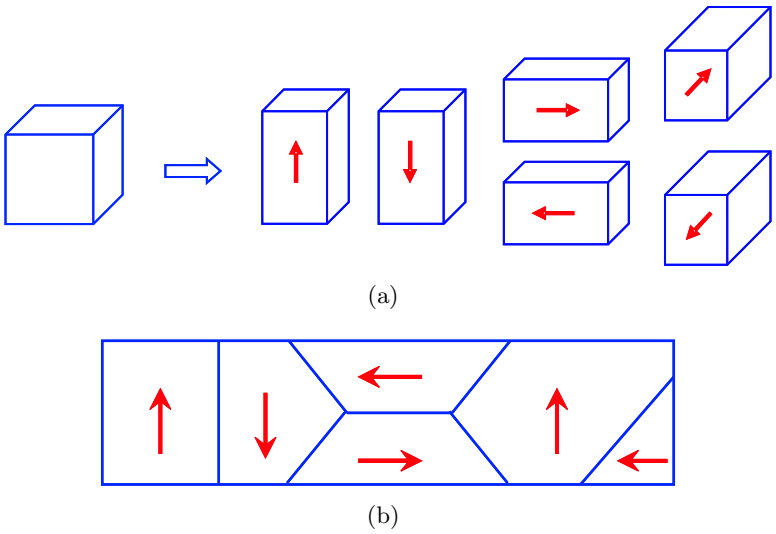

(a)

(b)

Figure 2.3: (a) Six variants of $BaTiO_3$ at room temperature. (b) Domains separated by domain walls.

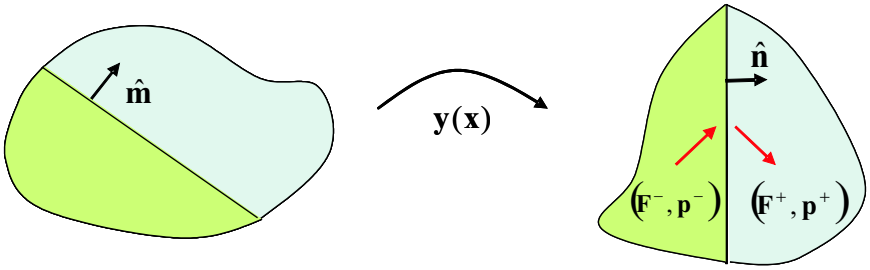

Figure 2.4: Compatibility condition.

where $\alpha = 0.9958$, $\beta = 1.0067$ and $p_0 = 0.26\,\mathrm{C/m^2}$ (Mitsui et al., 1981).

These variants can coexist as domains separated by domain walls as schematically shown by Fig. 2.3(b). The formation of domain walls is by no means arbitrary. Instead, an energy minimizing domain wall between variants i and j, i.e., an interface separating regions of deformation gradient and polarization $(\mathbf{F}^-, \mathbf{p}^-)$ and $(\mathbf{F}^+, \mathbf{p}^+)$ shown in Fig. 2.4 with $\mathbf{F}^- = \mathbf{Q}^-\mathbf{U}_i$, $\mathbf{p}^- = \mathbf{Q}^-\mathbf{p}_i$, $\mathbf{F}^+ = \mathbf{Q}^+\mathbf{U}_j$ and $\mathbf{p}^+ = \mathbf{Q}^+\mathbf{p}_j$ for some rotation $\mathbf{Q}^-$ and $\mathbf{Q}^+$ must satisfy two compatibility conditions (Shu and Bhattacharya, 2001):

$$\mathbf{F}^+ - \mathbf{F}^- = \mathbf{a} \otimes \hat{\mathbf{m}}, \tag{2.3}$$

$$(\mathbf{p}^+ - \mathbf{p}^-) \cdot \hat{\mathbf{n}} = 0 \tag{2.4}$$

where $\hat{\mathbf{m}}$, $\hat{\mathbf{n}}$ are the normal to the interface in the reference and the current configuration respectively, and $\mathbf{a}$ an arbitrary vector.

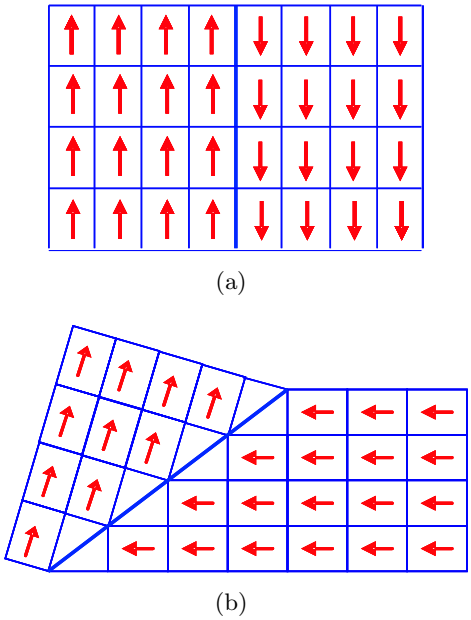

(a)

(b)

Figure 2.5: Schematic domain walls in $BaTiO_3$ at room temperature: an 180° domain wall (a) and a 90° domain wall (b).

The first condition is the mechanical compatibility condition also known as Hadamard's jump condition, it ensures the continuity or the coherence of the interface. The second is the electrical compatibility condition which ensures that no bound charge exists in the domain walls. Shu and Bhattacharya (2001)* proved that the 180° and 90° domain walls are the only two types of domain walls that satisfy these two compatibility conditions simultaneously during the paraelectric to a $\langle 100 \rangle$ polarized ferroelectric phase transition. Fig. 2.5 shows the schematic domain walls in $BaTiO_3$ at room temperature. A polarized light optical micrographs of domain patterns in $BaTiO_3$ single crystal is shown in Fig. 2.6 (Burcsu, 2001).

2.2 Perovskites As a Wide Band-Gap Semiconductor

To introduce a semiconductor, it is necessary to provide a short review of the electronic structure of solids. This is determined from quantum mechanics, by solving Schrödinger's equation. This is an eigenvalue problem and the eigenvalues are labelled the *energy states* and the eigenfunctions the *orbitals*. At zero temperature, the states are occupied by the electrons starting from the lowest state till all the electrons are exhausted (there is an

*Also see DeSimone and James (2002) for a similar result in ferromagnetic shape memory alloys.

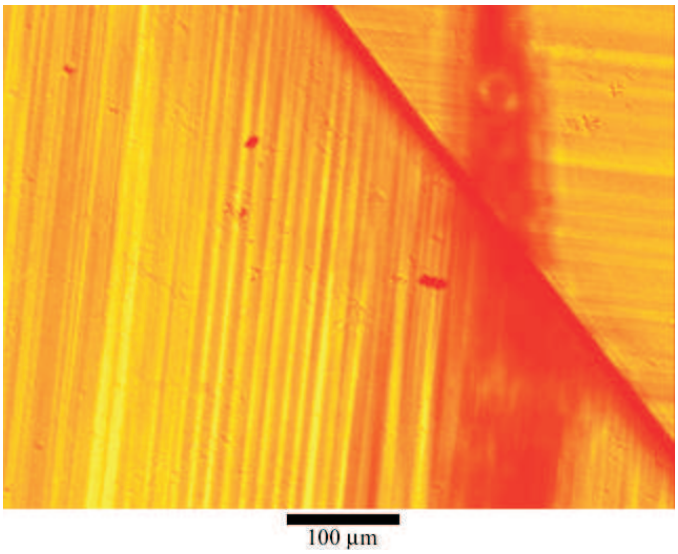

Figure 2.6: Polarized light optical micrographs of domain patterns in $BaTiO_3$ single crystal (Burcsu, 2001).

infinity of admissible states but only a finite number of electrons). The energy state up to which they are occupied is called the *Fermi level*, E_{fm}. This has a negative value signifying that the electron has an incentive to occupy this state, and its magnitude – interpreted as the work function necessary to remove an electron from the solid – is called the *work function*, ϕ_M.

Broadly speaking, there are two types of orbitals in a crystal (periodic solid): the *valence state* or *valence band* that is localized and the *conduction state* or *conduction band* that is completely delocalized. Electrons in the conduction band can freely be transported across the crystal and are responsible for its electrical conductivity. Typically the valence band has lower energy than the conduction band, and there is a gap between them which is called the *band gap*, E_g. If this gap is zero, and if the Fermi level includes portions of the conduction band, then the solid is a conductor. If on the other hand, the band gap is not zero and the Fermi level is below the conduction band, the solid is an insulator.

At finite temperature and in the presence of defects (dopants), electrons can be excited to cross the band gap from the valance band to the conduction band even in an insulator. Such a solid acquires some conductivity and is called a semiconductor. Clearly, there is no sharp distinction between an insulator and a semiconductor. An insulator at low temperature can become a semiconductor at a high temperature, it all depends on the energy gap, the temperature and the impurity level. Roughly speaking, the energy gap in most important

semiconductors is less than 2 eV and frequently as low as a few tenths of an electron volt (Ashcroft and Mermin, 1976). For example, at room temperature, silicon and germanium, the most widely used semiconductors have an energy gap of 1.12 eV and 0.66 eV respectively (Sze, 1981).

Ferroelectric perovskites are insulators in general. For example, the band gap for $BaTiO_3$ is 3.0 eV, and $PbZr_{0.40}Ti_{0.60}O_3$ is 3.4 eV (Scott et al., 1999). However, because large amount of impurities typically exists in perovskites, they become semiconductors and in order to investigate some properties concerning impurities or defects, it is crucial to treat them as such (Scott, 2000; Scott et al., 1999). In the continuum theory we develop, this means that we introduce a new kinematic quantity, the space-charge density.

Oxygen vacancies as n-type dopants $BaTiO_3$ and PZT are typically p-type semiconductors in bulk if undoped (Scott, 2000). This is because there is always a greater abundance of impurities such as Na, Al, Fe, Mg in the starting growth materials than there are high-valence impurities. These impurities are almost always substitutional in ABO_3 perovskites, with Na^{+1} going in for Ba^{+2} or Pb^{+2}, Al^{+3}, Fe^{+3} or Mg^{+2} for Ti^{+4}.

This can be changed in thin films by surface donor states, which are apt to create n-type inversion layers near the surface. It is known that the diffusion of electrode materials into the semiconducting dielectric films can produce an n-type surface layer on an otherwise p-type semiconductors, and this is the process that may occur in many ferroelectric memory films, including PZT/Pt, SBT/Pt and BST[†]/Pt.

It is also possible to prepare n-type ferroelectric perovskites in bulk by growing specimen in an oxygen-poor atmosphere. This is typically the case in thin films where oxygen loss at high temperature is quenched into the room temperature. When oxygen is lost, it exits the crystal as neutral O_2, leaving behind two electrons as illustrated in Fig. 2.7. The vacancy thus behaves as a donor with a binding energy of 1.0 eV (Waser, 1991; Zhang, 2004a). At room temperature, many of these electrons are thermally freed from the vacancy sites to form an n-type semiconductors. Oxygen vacancies can also become mobile at high temperature. Therefore we introduce the concentration of oxygen vacancies as an additional kinematic quantity in the continuum model developed in Chapter 3.

Metal-semiconductor junction When two metals with different Fermi levels or work functions are brought into contact, the electrons move from the surface of one to the

[†]Barium strontium titanate $Ba_xSr_{1-x}TiO_3$.

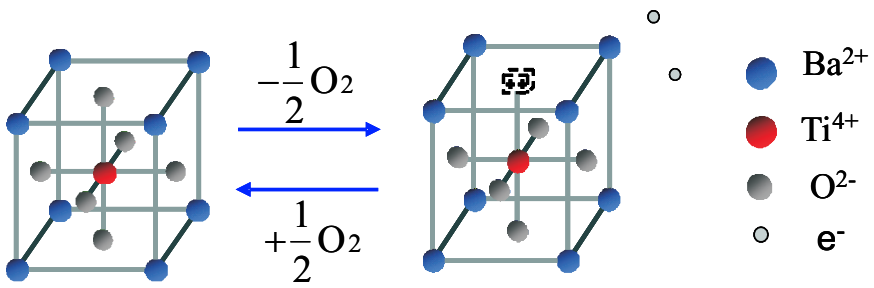

Figure 2.7: Formation of oxygen vacancies.

surface of the other till they reach the same chemical potential (matched Fermi levels) on both sides. The surface charges on each metal gives rise to a potential in the interior that uniformly shifts all of the bulk levels together with the chemical potential. Since the shift is uniform, the bulk properties in the interior are unaffected (Ashcroft and Mermin, 1976).

Similarly, when one metal and one semiconductor with different Fermi levels are put together, the electrons in the metal and the free carriers in the semiconductor redistribute themselves near the interface, so that when equilibrium is reached, the Fermi level on both sides are the same. However, compared to metals which have large amount of electrons, semiconductors usually have only limited free carriers. Hence, a certain region in the semiconductor in the vicinity of the junction will be practically depleted of mobile carriers. This region is called *depletion region* or *depletion layer*, its width is called *depletion layer width*. All the potential drops/raises caused by charge redistribution therefore takes place in the semiconductor, mostly in the depletion region. This changes the band structure, known as *band-bending*. Nevertheless, like metals, this potential does not affect the bulk properties of the semiconductor far away from the contact interface.

To understand the orders of magnitude, we take a quick heuristic look at the situation when Platinum and $BaTiO_3$ crystal with n-type doping are brought together. Fig. 2.8 is the energy diagram before and after contact is made. The Fermi level E_{fm}^{Pt} of Platinum is $-5.3\,\text{eV}$, corresponding to ϕ_M of $5.3\,\text{V}$. The constants of the band structure of $BaTiO_3$ are chosen to be (Scott, 2000): $E_c = -3.6\,\text{eV}$, $E_d = -4.0\,\text{eV}$, $E_a = -6.2\,\text{eV}$, $E_v = -6.6\,\text{eV}$, where E_c is the energy at the bottom of the conduction band, E_v the energy on the top of the valence band, E_d, E_a the donor and acceptor level respectively. After contact is made, the electrons from the conduction band cross over into Pt in search of lower energy. The outcome is a *built-in potential* in the $BaTiO_3$ side, and a potential barrier between Platinum

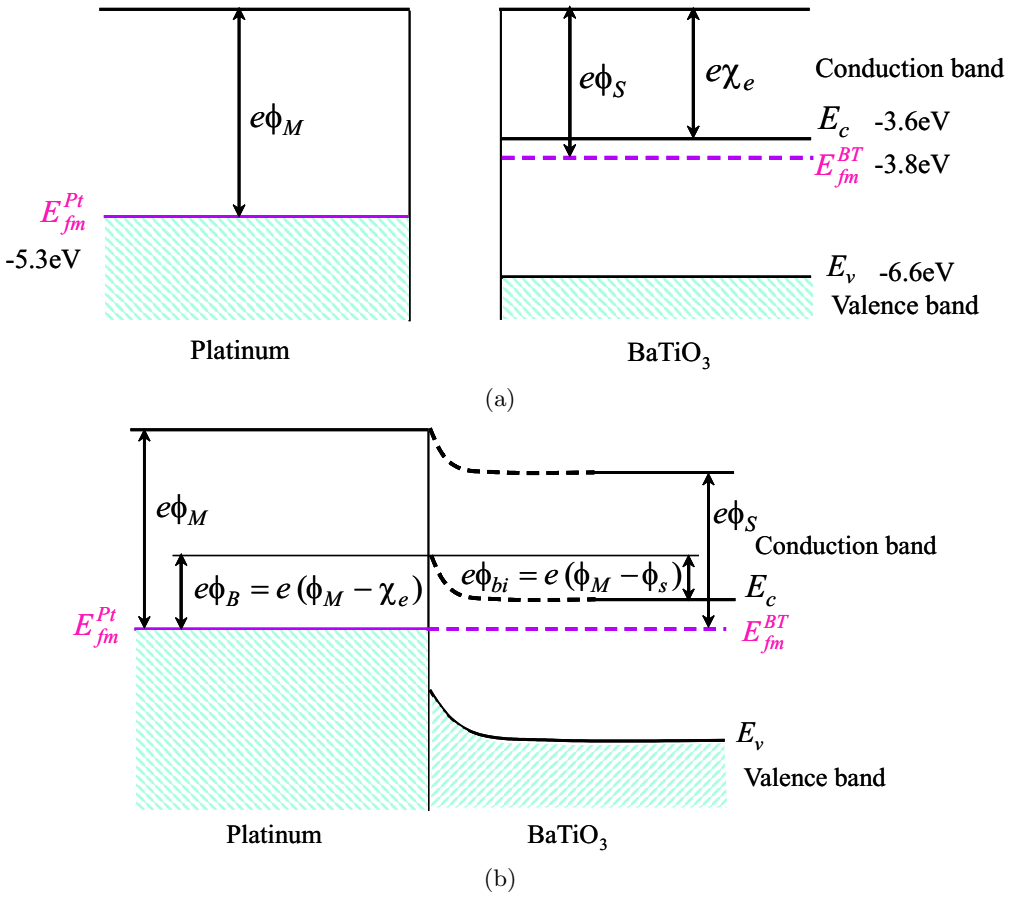

Figure 2.8: Energy diagrams for a junction between Pt and n-type $BaTiO_3$ before contact (a) and after contact (b).

and $BaTiO_3$ crystal. This barrier is called *Schottky barrier*. From Fig. 2.8, we notice that the barrier in the Platinum side is higher than the one in $BaTiO_3$ side.

The Schottky barrier height, ϕ_B, is defined as the potential difference between the Fermi energy of the metal and the band edge where the majority carriers reside (Solymar and Walsh, 1984), which is the conduction band in our case. Therefore,

$$\phi_B = \phi_M - \chi_e = 1.7\,\mathrm{V}, \tag{2.5}$$

where χ_e is the electron affinity of $BaTiO_3$, and it is equal to $|E_c|/e$. This barrier has to be overcame before any leakage current into the ferroelectric. This points to the importance of the choice of electrode through its work function. The higher the work function, the higher is the Schottky barrier.

The built-in potential, ϕ_{bi}, is equal to potential difference between the Fermi levels of

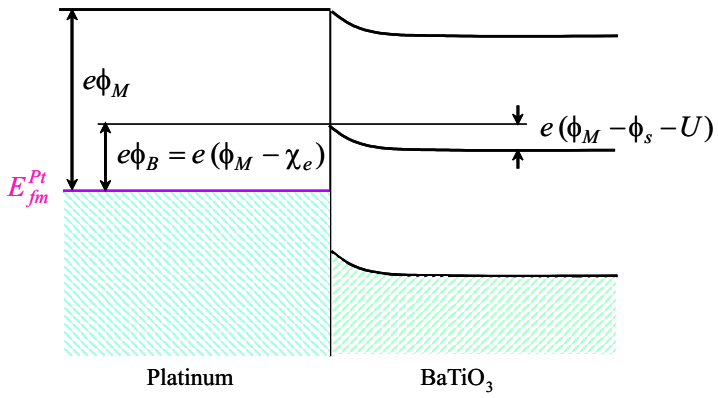

Figure 2.9: The junction of Fig. 2.8 under forward bias. The potential barrier for electrons on the semiconductor side is reduced by eU.

both sides before contact, i.e.,

$$\phi_{bi} = \frac{E_{fm}^{BT} - E_{fm}^{Pt}}{e} \approx \frac{1}{2e}(E_c + E_d - 2E_{fm}^{Pt}) = 1.5\,\mathrm{V}. \tag{2.6}$$

The last equality comes from the fact (Ashcroft and Mermin, 1976) that

$$E_{fm}^{BT} \approx \frac{E_c + E_d}{2} = -3.8\,\mathrm{eV} \tag{2.7}$$

for n-type dominant semiconductors.

In light of the built-in potential in the interior, we have a large gradient (electric field) near the electrode. This field, may drive the diffusion of oxygen vacancies.

Finally, in equilibrium, the number of electrons crossing over the barrier from both sides is the same. When a forward potential is applied, the electrons from $BaTiO_3$ into Platinum will increase exponentially, while the electron current from Platinum to $BaTiO_3$ remains the same (Fig. 2.9), that is, the junction acts like a rectifier. The junctions of this kind are usually referred to as *Schottky barrier diodes* or *Schottky diodes*[‡]. However, a Schottky barrier can be transformed to an Ohmic contact if there is a heavily doped region near the interface such that the depletion layer becomes thin enough to allow electrons tunnel through the barrier (Fig. 2.10). In this case, the interface becomes conductive.

[‡]However, the name *Schottky* comes from another effect called *Schottky effect* which deals with the image-force-induced lowering of potential barriers (Solymar and Walsh, 1984).

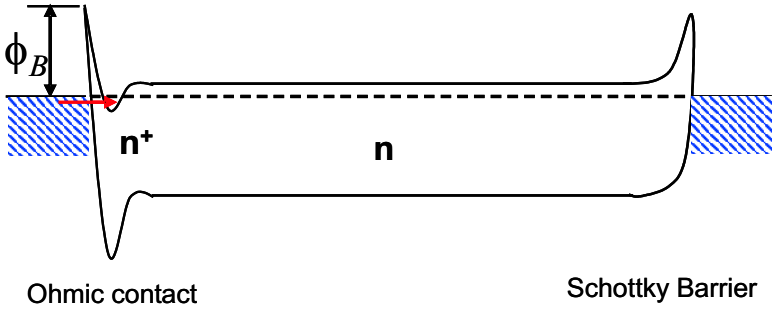

Figure 2.10: Ohmic contact vs. Schottky barrier

2.3 Ferroelectric Fatigue in Ferroelectric Thin Films

Ferroelectric fatigue is defined as the loss of switchable polarization with increasing number of bipolar switchings as shown in Fig. 2.11. It is one of the two critical issues (the other is dielectric breakdown) which has hindered the commercialization of ferroelectric memory devices, and therefore received considerable attention in the last decade. A large number of experiments have been conducted to investigate the possible cause of fatigue. Based on experimental observations, various mechanisms have been postulated, many of them interlinked. Yet none are unanimously accepted. Here, we give a brief review of the existing experiments mainly concerning two microscopic mechanisms: *electronic* and *ionic charge trapping*.[§] For more detailed discussion, see Scott (2000), Damjanovic (1998), Shaw et al. (2000) and Tagantsev et al. (2001).

Electrons and holes injected from the electrodes into the ferroelectric film can be trapped at deep levels and become immobilized producing simple charge defects. Fatigue mechanisms involving the injection/trapping of electrons/holes are called *electronic charge trapping mechanism*. Since oxygen vacancies are the most mobile ionic defects in perovskites, fatigue mechanisms involving redistribution of oxygen vacancies are called *ionic charge trapping mechanism*.

The strongest evidence for ionic charge trapping is the discovery of the almost fatigue-free YBCO/PZT/YBCO (Ramesh et al., 1992) and Pt/SBT/Pt (De Araujo et al., 1995) capacitors compared to the pronounced fatigue in Pt/PZT/Pt capacitors. The fact that the use of oxide electrodes in PZT dramatically improves its performance, and that SBT

[§]We focus on electric fatigue here, for mechanical fatigue caused by microcracking, please refer to Lynch et al. (1995); Lynch (1998); Park and Sun (1995); Kim and Jiang (1996); Zhu and Yang (1999); McMeeking (2001); Arias et al. (2004).

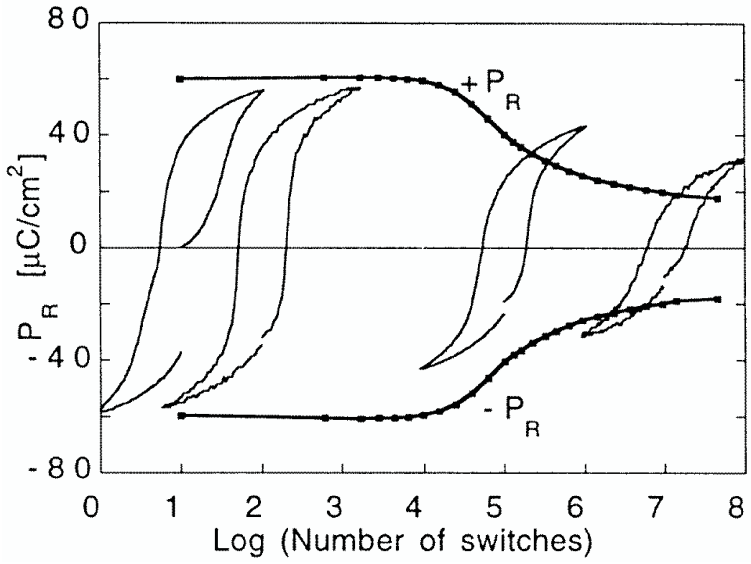

Figure 2.11: Ferroelectric fatigue (Damjanovic, 1998).

which has a complicated oxide-perovskite layer structure has low fatigue suggests a link between oxygen vacancies and fatigue. In addition, oxygen vacancy redistribution during polarization fatigue has also been reported (Scott et al., 1991; Sanchez et al., 1991).

Warren et al. (1994) conducted a series experiments on PZT thin films under different conditions: 1) an ultra violet light (UV)/bias combination; 2) a temperature/bias combination; 3) electrical fatigue. Their results show that switching polarization can be suppressed by any of these processes and can all be partially restored by an UV/saturating bias combination. In the case of UV/bias combination, the suppression of switchable polarization is maximized by partially switching the film with a bias near the switching threshold and by illuminating with band-gap light (whose frequency is such that its energy is equal to E_g). Since large amount of electrons can be generated either by band-gap light or by thermal activation, they argued that these three different fatigue are essentially the same in mechanism: the electrons generated either by optical, thermal, or electrical process may get trapped in the domain walls where they are energetically favorable, therefore the main mechanism for ferroelectric fatigue is domain wall pinning caused by electronic charge trapping. The fact all three fatigue can be partially restored by UV/bias combination is explained as the recombination of trapped charges in domain walls with holes generated by UV illumination. They concluded that ionic defects such as oxygen vacancies may only peripherally involved in the ferroelectric fatigue in Pt/PZT/Pt capacitors.

In a later work, Warren et al. (1995) also conducted their experiments in a reduced annealing (oxygen deficient) process. They found that oxygen-poor annealing can also cause suppression of switchable polarization, and this suppression can not be restored by UV/bias combination but can be restored by an oxygen-rich re-annealing. Based on this discovery, they felt that oxygen vacancy also play a role in ferroelectric fatigue.

Another experiment that favors oxygen vacancy mechanism was reported by Gütter et al. (1995). They found that fatigue leads to changes in phonon frequencies and Raman cross sections in $PbZr_{0.48}TiO_3$. Simultaneously, a characteristic IR absorption band near $4000\,cm^{-1}$ shifts towards higher energies. The results indicate that fatigue in PZT can be related to an increase of the local lattice distortion and a formation of defects both caused by oxygen loss from the samples.

Cillessen et al. (1997) reported a significant thickness dependence of switching voltage in MgO/LSCO/PZT/Au capacitor, while MgO/LSCO/PZT/LSCO/Ag (heteroepitaxial) and Si/LSCO/PZT/LSCO/Ag (textured film) showed no such dependence. A simple injection model (capacitor with a nonlinear resistor) was proposed, the fact it successfully fits the experimental data supports the electronic charge trapping mechanism.

Du and Chen (1998) reported that an Pt/p-Si/PZT/Pt or Pt/SiO_2/PZT/Pt structure can mitigate the fatigue, while Pt/n-Si/PZT/Pt can not. Based on their results, they support the electronic charge injection mechanism.

Nagaraj et al. (2001) conducted an investigation on PNZT with different electrodes: Pt, LSCO and SRO. They found that LSCO/PNZT/LSCO and SRO/PNZT/SRO capacitors show much superior performance than Pt/PNZT/Pt capacitors. Further, Pt/PNZT/Pt has significant leakage current relaxation while LSCO/PNZT/LSCO and SRO/PNZT/SRO do not. The direct implication of their results is that electronic charges are trapped inside the films, which may account for the fatigue of Pt/PNZT/Pt.

A strong opposition of oxygen vacancy as a fatigue mechanism was voiced by Nuffer et al. (2001), based on their result that no significant amount of oxygen is released from PZT during field cycling.

As to the role of domain walls in ferroelectric fatigue, Jang and Yoon (1999) investigated the performance of capacitors made of various stacking sequences of sol-gel prepared PZT/PZ layers (PZ is anti-ferroelectric). The results show that capacitors with only two PZ layers (PZ1/PZ5/PZ1) maintain single hysteresis loop, while show almost no fatigue. The

results was interpreted as less stress and less defects in domain walls can improve fatigue performance since antiferroelectrics comprise of mainly 180° domains.

In addition, Bornand et al. (2000) also reported orientation dependence of fatigue behavior in relaxor ferroelectric-$PbTiO_3$ thin films. It was found that highly <001> pseudo-cubic oriented PYbN-PT/SRO/LAO have better fatigue resistance than highly ⟨111⟩ pseudo-cubic oriented PYbN-PT/SRO/STO films. They argued that the difference between domain structures in those materials is the reason for this difference.

Besides the experimental efforts, researchers have also begun to conduct first principle or Monte Carlo simulation concerning the role of oxygen vacancies on domain wall pinning. He and Vanderbilt (2003) investigated the interaction of oxygen vacancies and 180° domain walls in tetragonal $PbTiO_3$ using density-functional theory. Their calculations show that the vacancies do have a lower formation energy in domain walls than in the bulk, and thus can be trapped in domain walls. Similarly, Calleja et al. (2003) conducted a Monte Carlo simulation on 90° domain walls in orthorhombic $CaTiO_3$, the binding energy of an oxygen vacancies in the domain wall with respect to the bulk is calculated to be about 1.2 eV smaller. Both of the calculations indicatd that oxygen vacancy may be a reason of domain main wall pinning.

Alternatively, Brennan (1993) proposed: defects (most likely, oxygen vacancies) generate field energy, therefore are more likely to induce tail to tail domain walls. The compensation of the Coulomb potential of a vacancy by the opposing domains makes the site less attractive to ions of the same species, at the same time, defects of the same type tends to align together to share a domain walls in order to reduce the energy. However, this model is still in scenario stage, more quantitative models are needed.

At the macroscopic level, blocking layer model (Larsen et al., 1994), passive layer model (Tagantsev et al., 1995a), seeds inhibition (Colla et al., 1998) and domain wall pinning (Colla et al., 1998) have been proposed. Unfortunately none of them are comprehensive and able to capture all the phenomena accompanied with ferroelectric fatigue.

Chapter 3

Continuum Model

In this chapter, we present a comprehensive continuum model that treats ferroelectrics as a deformable, polarizable and (wide band-gap) semiconducting solids where oxygen vacancies act as donors. Polarizable means that the material may be spontaneously polarized and semiconducting means that the solid may be charged.

We introduce the kinematics in Section 3.1. In Section 3.2, we discuss space charge density in semiconducting solids. We introduce the electrostatic theory for ferroelectrics in Section 3.3. We introduce the concept of Maxwell stress and derive various jump conditions in an electrostatic field containing deformable polarizable bodies.

In Section 3.4, we calculate the rate of the dissipation of the whole system in any process. We then show that this can be written as a sum of products of conjugate pairs - generalized velocity (time rate of change of some quantity or flux of some quantity) times a generalized force (a quantity that depends on the state and not the rate of the change of the state).

Following arguments similar to those of Coleman and Noll (1963), we can use the dissipation inequality (second law of thermodynamics) to write down the governing equations in Section 3.5 with defects, free charges, polarization, electric potential and elastic deformation as variables without making any a priori assumptions on the space charge distribution and the polarization.

We conclude this chapter with a discussion of special cases.

3.1 Kinematics

Consider a ferroelectric semiconducting crystal in an external field shown in Fig. 3.1. It occupies a region $\Omega \subset \mathbb{R}^3$ in the reference configuration. A deformation $\mathbf{y} : \Omega \to \mathbb{R}^3$ brings

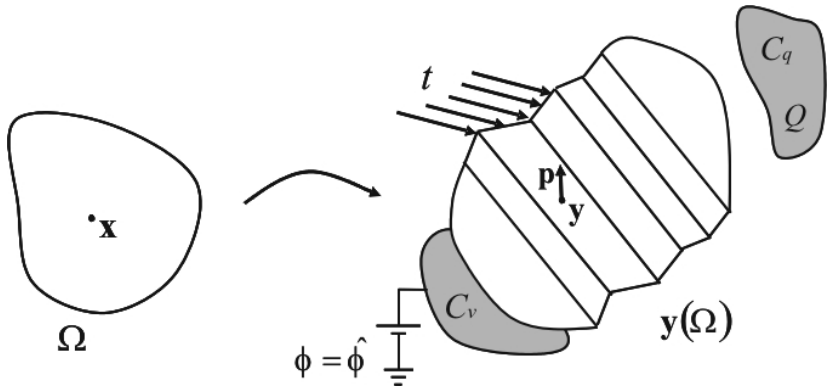

Figure 3.1: A ferroelectric semiconducting system in an external field generated by conductors C_q and C_v: C_q with fixed charge Q is fixed in space by external forces, while C_v with fixed potential deforms with the ferroelectric body Ω.

it to the proximity of electrodes $C_v \subset \mathbb{R}^3$ with fixed potential $\hat{\phi}$ and $C_q \subset \mathbb{R}^3$ with fixed charge Q under the action of traction $\mathbf{t}$. The deformation gradient is $\mathbf{F} = \nabla_{\mathbf{x}}\mathbf{y}$, and we assume that the deformation is invertible and $J = \det \mathbf{F} > 0$ almost everywhere in Ω.

We find it convenient to choose the undistorted non-polar phase at Curie temperature as our reference configuration. We invoke the Cauchy-Born rule (Ericksen, 1984) here, which states that the overall distortion of the lattice follows the macroscopic deformation gradient, or

$$\mathbf{e}_i = \nabla_{\mathbf{x}}\mathbf{y}\, \mathbf{e}_i^0, \quad i = 1, 2, 3 \tag{3.1}$$

where $\mathbf{e}_i$ are $\mathbf{e}_i^0$ are the lattice vectors in the reference and current configuration respectively.

We denote by $\mathbf{p} : \mathbf{y}(\Omega) \to \mathbb{R}^3$ the polarization of ferroelectric material per unit deformed volume, and by $\mathbf{p}_0 : \Omega \to \mathbb{R}^3$ the polarization per unit undeformed volume. We have

$$\mathbf{p}_0(\mathbf{x}) = (\det \nabla_{\mathbf{x}}\mathbf{y}(\mathbf{x}))\mathbf{p}(\mathbf{y}(\mathbf{x}))\ . \tag{3.2}$$

We shall make the following assumption for later. The conductor C_q is fixed in space but the conductor C_v deforms with the body with negligible elastic energy. This is reasonable since electrodes are usually very thin compared to the body.

3.2 Space Charge Density in Semiconducting Solids

The total charge density at any point in a semiconductor in current configuration is (Ashcroft and Mermin, 1976)

$$\rho = e\left(zN_d - z'N_a - n_d - n_c + p_a + p_v\right) \tag{3.3}$$

where N_d is the density of donors (number per unit deformed volume), N_a the density of acceptors, n_d the density of electrons in donor's level, n_c the density of electrons in conduction band, p_a the density of holes in acceptor's level, p_v the density of holes in valence band, z and z' the valency of donors and acceptors respectively, and e the coulomb charge per electron.

We assume that oxygen vacancies are the dominant impurities in the semiconductor being considered*. Since oxygen vacancies act as donors, we may set $N_a = p_a = 0$ in Eq. (3.3). Further, electrons and holes have much higher mobility than defects, so we group defect-based charges and electronic charges separately. Thus,

$$\rho = e(zN_d - n_d - n_c + p_v) = ezN_d + \rho_c \tag{3.4}$$

with

$$\rho_c = e(-n_d + p_v - n_c)\ . \tag{3.5}$$

We call ρ_c *free charge density*.

We define the counterparts of N_d, ρ, ρ_c in the reference configuration as N_{d0}, ρ_0, ρ_{c0} (number per unit undeformed volume) respectively. Assuming that no oxygen vacancies or charges are generated in the interior, we have the following conservation principles:

$$\dot{N}_{d0} = -\nabla_{\mathbf{x}} \cdot \mathbf{J}_{N_{d0}}, \tag{3.6}$$

$$\dot{\rho}_{c0} = -\nabla_{\mathbf{x}} \cdot \mathbf{J}_{\rho_{c0}} \tag{3.7}$$

where $\mathbf{J}_{N_{d0}}$ and $\mathbf{J}_{\rho_{c0}}$ are the flux of defects and free charges in the reference configuration respectively.

We point out here that the dot on N_{d0} and ρ_{c0} denotes the *material time derivative* of

*We could proceed analogously for any other dopants.

N_{d0} and ρ_{c0} respectively. For any variable ξ defined on $\mathbf{y}(\Omega)$,

$$\dot{\xi}(\mathbf{y}(\mathbf{x},t),t) = \frac{\partial \xi(\mathbf{y}(\mathbf{x},t),t)}{\partial t}\bigg|_{\mathbf{x}} = \frac{\partial \xi(\mathbf{y},t)}{\partial t}\bigg|_{\mathbf{y}} + \mathbf{v}\cdot\nabla_{\mathbf{y}}\xi(\mathbf{y},t) \tag{3.8}$$

where we call $\frac{\partial \xi(\mathbf{y},t)}{\partial t}|_{\mathbf{y}}$ the *spatial time derivative* of ξ and denote it as $\overset{o}{\xi}$.

3.3 Electric Field

The polarization and the space charges in the ferroelectric body as well as the charges on the surfaces of conductors generate an electric field in all space. The electrostatic potential ϕ at any point in $\mathbb{R}^3$ is obtained by solving Maxwell equation:

$$\begin{aligned} \nabla_{\mathbf{y}}\cdot(-\epsilon_0\nabla_{\mathbf{y}}\phi + \mathbf{p}\,\chi(\mathbf{y}(\Omega,t))) &= \rho\chi(\mathbf{y}(\Omega,t)) \qquad \text{in } \mathbb{R}^3\backslash(C_v\cup C_q), \\ \nabla_{\mathbf{y}}\phi &= 0 \qquad \text{on } C_v\cup C_q \end{aligned} \tag{3.9}$$

subject to

$$\begin{aligned} \int_{\partial C_q}\frac{\partial\phi}{\partial\hat{\mathbf{n}}}\,dS_y &= -\frac{Q}{\epsilon_0}, \\ \phi &= \hat{\phi} \qquad \text{on } C_v, \\ \phi &\to 0 \qquad \text{as } |\mathbf{y}|\to\infty, \end{aligned} \tag{3.10}$$

where ϵ_0 is the permittivity coefficient of the free space, and χ_D is the characteristic function of domain D.

Precisely, $\phi\in H^1(\mathbb{R}^3)$ satisfies the following:

$$-\int_{\mathbf{R}^3}(-\epsilon_0\nabla_{\mathbf{y}}\phi + \mathbf{p}\,\chi(\mathbf{y}(\Omega))\cdot\nabla\psi\,dy = \int_{\mathbf{y}(\Omega)}\rho\,\psi\,dy + \int_{\partial C_v\cup\partial C_q}\sigma\,\psi\,dS_y. \tag{3.11}$$

$$\int_{\partial C_q}\sigma\,dS_y = Q \qquad \text{on } C_q, \tag{3.12}$$

$$\phi = \hat{\phi} \qquad \text{on } C_v \tag{3.13}$$

for each $\psi\in H^1(\mathbb{R}^3)$, where $\sigma:\partial C_v\cup\partial C_q\to\mathbb{R}$ measurable is the surface charge density on

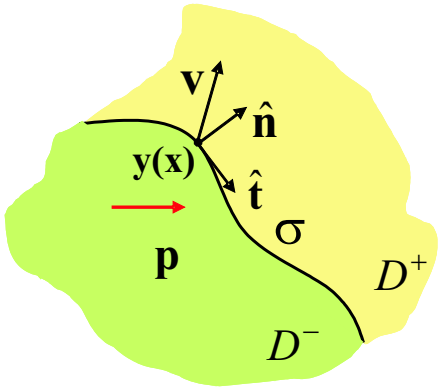

Figure 3.2: An interface separating D^- from D^+ in an electric field. D^- is a dielectric or ferroelectric body with polarization $\mathbf{p}$; D^+ can be a conductor or vacuum; σ is the surface charge density on the interface; $\hat{\mathbf{n}}$ is the unit norm of interface, pointing to D^+ from D^-; and $\mathbf{v}$ is the velocity of a material point on the interface.

the interface, and it is defined as

$$\sigma = [\![-\epsilon_0 \nabla_{\mathbf{y}} \phi + \mathbf{p}\, \chi(\mathbf{y}(\Omega)]\!] \cdot \hat{\mathbf{n}}. \tag{3.14}$$

Here $[\![\ ]\!]$ denotes the jump across an interface: $[\![\xi]\!] = \xi^+ - \xi^-$, with ξ being some variable defined in both domains; $\hat{\mathbf{n}}$ is the unit norm of the interface, pointing to D^+ from D^-.

Although ϕ is continuous in $\mathbb{R}^3$, other quantities like $\nabla_{\mathbf{y}}\phi$ can be discontinuous across some interfaces, as Eq. (3.14) shows. Here we discuss some jump conditions in a more general setting for later use. In particular, we shall be interested in time-dependent processes. So the polarization $\mathbf{p}$ and the deformation $\mathbf{y}$ could depend on time, and we solve Eq. (3.11)-(3.13) at each time to find the electric potential.

The jump condition across any interface separating D^+ and D^- is (Fig. 3.2),

$$[\![-\epsilon_0 \nabla_{\mathbf{y}} \phi + \mathbf{p}]\!] \cdot \hat{\mathbf{n}} = \sigma\ . \tag{3.15}$$

If we assume as shown in Fig. 3.2 that $\mathbf{p} = 0$ in D^+, and if $\mathbf{p}$ denotes the polarization in D^- (for example, D^+ can be a conductor or vacuum and D^- a dielectric or ferroelectric body), then Eq. (3.15) can be rewritten as

$$[\![\nabla_{\mathbf{y}} \phi]\!] \cdot \hat{\mathbf{n}} = -\frac{1}{\epsilon_0} \mathbf{p} \cdot \hat{\mathbf{n}} - \frac{\sigma}{\epsilon_0}\ . \tag{3.16}$$

Now, let $\hat{\mathbf{y}}(\alpha)$ be a curve on the interface at time t_0 parameterized by α. We have, from the continuity of ϕ,

$$\phi^-(\hat{\mathbf{y}}(\alpha)) = \phi^+(\hat{\mathbf{y}}(\alpha)) \ . \tag{3.17}$$

Differentiating it with respect to α, we have

$$[\![\nabla_{\mathbf{y}}\phi]\!] \cdot \frac{\partial \hat{\mathbf{y}}}{\partial \alpha} = 0. \tag{3.18}$$

Since this holds for any curve on the interface, we obtain continuity of $\nabla_{\mathbf{y}}\phi$ along the tangent, i.e.,

$$[\![\nabla_{\mathbf{y}}\phi]\!] \cdot \hat{\mathbf{t}} = 0, \quad \forall \quad \hat{\mathbf{n}} \cdot \hat{\mathbf{t}} = 0. \tag{3.19}$$

Combining this with Eq. (3.16), we obtain

$$[\![\nabla_{\mathbf{y}}\phi]\!] = -\left(\frac{1}{\epsilon_0}\mathbf{p} \cdot \hat{\mathbf{n}} + \frac{\sigma}{\epsilon_0}\right)\hat{\mathbf{n}} \ . \tag{3.20}$$

Now consider a material point $\mathbf{x}$ on the interface. Let us assume that the interface does not propagate in the reference configuration, so that particle velocity remains continuous across the interface. Since electric potential ϕ is continuous, we have

$$\phi^-(\mathbf{y}(\mathbf{x},t),t) = \phi^+(\mathbf{y}(\mathbf{x},t),t), \tag{3.21}$$

so that

$$\dot{\overline{\phi^-(\mathbf{y}(\mathbf{x},t),t)}} = \dot{\overline{\phi^+(\mathbf{y}(\mathbf{x},t),t)}}, \tag{3.22}$$

or,

$$\overset{o}{\phi}{}^- + \nabla_{\mathbf{y}}\phi^- \cdot \mathbf{v} = \overset{o}{\phi}{}^+ + \nabla_{\mathbf{y}}\phi^+ \cdot \mathbf{v} \ . \tag{3.23}$$

We point out that $\dot{\phi}$ here denotes the material time derivative of ϕ, and $\overset{o}{\phi}$ denotes the spatial time derivative of ϕ. Hence,

$$[\![\overset{o}{\phi}]\!] = -[\![\nabla_{\mathbf{y}}\phi]\!] \cdot \mathbf{v} \tag{3.24}$$

where $\mathbf{v}$ is the particle velocity of the material point $\mathbf{x}$.

Plug Eq. (3.20) into Eq. (3.24) to find

$$\overset{o}{[\![\phi]\!]} = \frac{1}{\epsilon_0}(\mathbf{p}\cdot\hat{\mathbf{n}})(\mathbf{v}\cdot\hat{\mathbf{n}}) + \frac{\sigma}{\epsilon_0}(\mathbf{v}\cdot\hat{\mathbf{n}})\ . \tag{3.25}$$

Another important quantity we will use later is that of the *Maxwell stress tensor* defined as

$$\mathbf{T}_{\mathrm{M}} = \mathbf{E}\otimes\mathbf{D} - \frac{\epsilon_0}{2}\mathbf{E}\cdot\mathbf{E}\,\mathbf{I} \tag{3.26}$$

where $\mathbf{E} = -\nabla_{\mathbf{y}}\phi$ is the electric field and $\mathbf{D} = \epsilon_0\mathbf{E} + \mathbf{p}\chi(\Omega^-)$ is the electric displacement.

The discontinuity of $\mathbf{E}$ or $\mathbf{D}$ across an interface leads to the discontinuity of $\mathbf{T}_{\mathrm{M}}$. By a direct calculation on an interface as above between a ferroelectric and vacuum or a conductor, we have

$$\begin{aligned}
[\![\mathbf{T}_{\mathrm{M}}\hat{\mathbf{n}}]\!] &= [\![(\mathbf{E}\otimes\mathbf{D} - \frac{\epsilon_0}{2}\mathbf{E}\cdot\mathbf{E}\,\mathbf{I})\cdot\hat{\mathbf{n}}]\!] \\
&= \langle\mathbf{E}\rangle\,[\![\mathbf{D}\cdot\hat{\mathbf{n}}]\!] + [\![\mathbf{E}]\!]\,\langle\mathbf{D}\rangle\cdot\hat{\mathbf{n}} - \epsilon_0(\langle\mathbf{E}\rangle\cdot[\![\mathbf{E}]\!])\hat{\mathbf{n}} \\
&= \langle\mathbf{E}\rangle\sigma + [\![\mathbf{E}]\!]\left(\epsilon_0\langle\mathbf{E}\rangle\cdot\hat{\mathbf{n}} + \frac{1}{2}\mathbf{p}\cdot\hat{\mathbf{n}}\right) - \epsilon_0(\langle\mathbf{E}\rangle\cdot[\![\mathbf{E}]\!])\hat{\mathbf{n}} \\
&= \left(\mathbf{E}^- + \frac{[\![\mathbf{E}]\!]}{2}\right)\sigma + \epsilon_0[\![\mathbf{E}]\!]\langle\mathbf{E}\rangle\cdot\hat{\mathbf{n}} + \frac{1}{2}(\mathbf{p}\cdot\hat{\mathbf{n}})[\![\mathbf{E}]\!] - \epsilon_0\langle\mathbf{E}\rangle\cdot((([\![\mathbf{E}]\!]\cdot\hat{\mathbf{n}})\,\hat{\mathbf{n}})\,\hat{\mathbf{n}} \\
&= \left(\mathbf{E}^- + \frac{[\![\mathbf{E}]\!]}{2}\right)\sigma + \frac{1}{2}(\mathbf{p}\cdot\hat{\mathbf{n}})[\![\mathbf{E}]\!] \\
&= \mathbf{E}^-\sigma + \frac{1}{2\epsilon_0}(\mathbf{p}\cdot\hat{\mathbf{n}} + \sigma)^2\hat{\mathbf{n}}\ .
\end{aligned} \tag{3.27}$$

The second equality uses the identity

$$[\![\phi\,\psi]\!] = [\![\phi]\!]\langle\psi\rangle + \langle\phi\rangle[\![\psi]\!] \tag{3.28}$$

where

$$\langle\phi\rangle = \frac{\phi^+ + \phi^-}{2} \tag{3.29}$$

is the average of the limiting values of a discontinuous quantity ϕ. The third recalls the definition of $\mathbf{D}$ and the assumption that $\mathbf{p} = 0$ on D^+ and the fourth the continuity of $\mathbf{E} = -\nabla_{\mathbf{y}}\phi$ along the tangential direction. The last equality is obtained by using Eq. (3.20).

3.4 Rate of Dissipation of the System

The rate of dissipation of the whole system $\mathcal{D}$ is defined as the difference between the rate of external working $\mathcal{F}$ and the rate of the change of the total energy $d\mathcal{E}/dt$:

$$\mathcal{D} = \mathcal{F} - \frac{d\mathcal{E}}{dt} \, . \tag{3.30}$$

3.4.1 Rate of External Working

The rate of external working $\mathcal{F}$ should include the mechanical work done by external forces, the electric work done by the electrodes, and the chemical energy flux from C_v into Ω:

$$\begin{aligned} \mathcal{F} = \hat{\phi} \frac{d}{dt} \int_{\mathbf{y}(\partial C_v)} \sigma \, dS_y + \int_{\mathbf{y}(\partial_s \Omega)} \mathbf{t} \cdot \dot{\mathbf{y}} \, dS_y \\ - \int_{\partial\Omega} \mu_{N_{d0}} \mathbf{J}_{N_{d0}} \cdot \hat{\mathbf{m}} \, dS_x - \int_{\partial\Omega} \mu_{\rho_{c0}} \mathbf{J}_{\rho_{c0}} \cdot \hat{\mathbf{m}} \, dS_x \end{aligned} \tag{3.31}$$

where $\mu_{N_{d0}}$ and $\mu_{\rho_{c0}}$ are respectively the chemical potential carried by the flux of the oxygen vacancies N_{d0} and that of charges ρ_{c0}, dS_y and dS_x are the differential area in the current and reference configuration respectively, $\hat{\mathbf{m}}$ the normal to surface in the reference configuration, and $\hat{\mathbf{n}}$ its counterpart in the current configuration.

Using the divergence theorem and Eq. (3.6) and (3.7), we can rewrite $\mathcal{F}$ as

$$\begin{aligned} \mathcal{F} = \hat{\phi} \frac{d}{dt} \int_{\mathbf{y}(\partial C_v)} \sigma \, dS_y + \int_{\mathbf{y}(\partial_s \Omega)} \mathbf{t} \cdot \dot{\mathbf{y}} \, dS_y \\ - \int_{\Omega} \left(\nabla_{\mathbf{x}} \mu_{N_{d0}} \cdot \mathbf{J}_{N_{d0}} + \nabla_{\mathbf{x}} \mu_{\rho_{c0}} \cdot \mathbf{J}_{\rho_{c0}} \right) \, dx \\ + \int_{\Omega} \left(\mu_{N_{d0}} \dot{N}_{d0} + \mu_{\rho_{c0}} \dot{\rho}_{c0} \right) \, dx \, . \end{aligned} \tag{3.32}$$

3.4.2 Total Energy of the System

The total energy of the system consists of two parts: the energy stored in the ferroelectric material and the electrostatic field energy generated by external and internal sources, i.e.,

$$\mathcal{E} = \int_{\Omega} W_0 \, dx + \frac{\epsilon_0}{2} \int_{\mathbb{R}^3} |\nabla \phi|^2 \, dx \, . \tag{3.33}$$

We will justify this statement and discuss related issues in Chapter 6. Here, W_0 is the stored energy per unit reference volume in the ferroelectric material. We make the con-

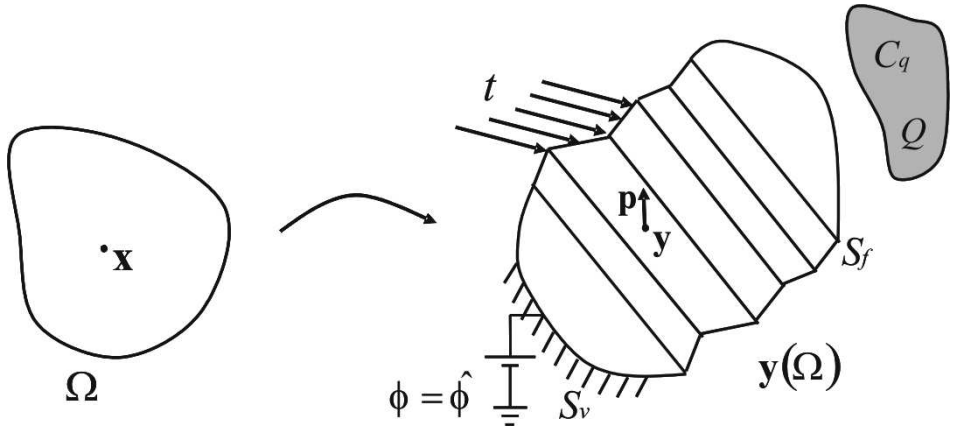

Figure 3.3: A simplified version of Fig 3.1: S_v is the part of $\partial\mathbf{y}(\Omega)$ with fixed potential.

stitutive assumption that it depends on defect density N_{d0}, free charge density ρ_{c0}, polarization $\mathbf{p}_0$, polarization gradient $\nabla_{\mathbf{x}}\mathbf{p}_0$, and deformation gradient $\nabla_{\mathbf{x}}\mathbf{y}$, i.e., $W_0 = W_0(N_{d0}, \rho_{c0}, \mathbf{p}_0, \nabla_{\mathbf{x}}\mathbf{p}_0, \nabla_{\mathbf{x}}\mathbf{y})$. We require the stored energy density W_0 to satisfy frame indifference and material symmetry.

Recall that the electrical potential ϕ is obtained by solving Eq. (3.9) and its boundary conditions (Eq. (3.10)). Recall also the assumption that C_q is fixed and C_v deformable with zero elastic energy. A better way to picture this is Fig. 3.3, where we idealize C_v as an interface $S_v = \mathbf{y}(S_{v0})$ between the vacuum and semiconductor $\mathbf{y}(\Omega)$ on which the potential is fixed. We also denote $S_f = \partial\mathbf{y}(\Omega)\backslash S_v$ as the interface where $\mathbf{y}(\Omega)$ has direct contact with vacuum.

3.4.3 Rate of Change of Total Energy

The rate of change of total energy in Eq. (3.30) is,

$$\frac{d\mathcal{E}}{dt} = \int_\Omega \dot{W}_0\, dx + \frac{d}{dt}\left[\frac{1}{2}\int_{\mathbb{R}^3} \epsilon_0 |\nabla_y \phi|^2\, dy\right] . \tag{3.34}$$

We can directly calculate the first term on the right-hand side of Eq. (3.34),

$$\begin{aligned}
&\int_\Omega \dot{W}_0(N_{d0}, \rho_{c0}, \mathbf{p}_0, \nabla_{\mathbf{x}}\mathbf{p}_0, \nabla_{\mathbf{x}}\mathbf{y})\, dx \\
&= \int_\Omega \left(\frac{\partial W_0}{\partial N_{d0}}\dot{N}_{d0} + \frac{\partial W_0}{\partial \rho_{c0}}\dot{\rho}_{c0}\right) dx \\
&\quad + \int_\Omega \left\{\frac{\partial W_0}{\partial \mathbf{p}_0}\cdot\dot{\mathbf{p}}_0 - \left[\nabla_{\mathbf{x}}\cdot\left(\frac{\partial W_0}{\partial \nabla_{\mathbf{x}}\mathbf{p}_0}\right)\right]\cdot\dot{\mathbf{p}}_0\right\} dx + \int_{\partial\Omega}\left(\frac{\partial W_0}{\partial \nabla_{\mathbf{x}}\mathbf{p}_0}\hat{\mathbf{m}}\right)\cdot\dot{\mathbf{p}}_0\, dS_x
\end{aligned}$$

$$-\int_{\mathbf{y}(\Omega)}\left[\nabla_{\mathbf{y}}\cdot\left(\frac{1}{J}\frac{\partial W_0}{\partial \mathbf{F}}\mathbf{F}^T\right)\right]\cdot\mathbf{v}\,dy+\int_{\partial\mathbf{y}(\Omega)}\left(\frac{1}{J}\frac{\partial W_0}{\partial \mathbf{F}}\mathbf{F}^T\hat{\mathbf{n}}\right)\cdot\mathbf{v}\,dy\,. \tag{3.35}$$

We have used the divergence theorem in the reference configuration to obtain the second and third integral on the right, and the divergence theorem in the current configuration to obtain the last two integrals. We clarify using indicial notation that

$$\begin{aligned}
\left[\nabla_{\mathbf{x}}\cdot\left(\frac{\partial W_0}{\partial\nabla_{\mathbf{x}}\mathbf{p}_0}\right)\right]\cdot\dot{\mathbf{p}}_0&=\left(\frac{\partial W_0}{\partial p_{0I,J}}\right)_{,J}\dot{p}_{0I},\\
\left(\frac{\partial W_0}{\partial\nabla_{\mathbf{x}}\mathbf{p}_0}\hat{\mathbf{m}}\right)\cdot\dot{\mathbf{p}}_0&=\frac{\partial W_0}{\partial p_{0I,J}}\hat{m}_J\dot{p}_{0I},\\
\left[\nabla_{\mathbf{y}}\cdot\left(\frac{1}{J}\frac{\partial W_0}{\partial \mathbf{F}}\mathbf{F}^T\right)\right]\cdot\mathbf{v}&=\left(\frac{1}{J}\left(\frac{\partial W_0}{\partial \mathbf{F}_{iI}}\right)\mathbf{F}_{jI}\right)_{,j}v_i,\\
\left(\frac{1}{J}\frac{\partial W_0}{\partial \mathbf{F}}\mathbf{F}^T\hat{\mathbf{n}}\right)\cdot\mathbf{v}&=\frac{1}{J}\left(\frac{\partial W_0}{\partial \mathbf{F}_{iI}}\right)\mathbf{F}_{jI}v_i\hat{n}_j
\end{aligned}$$

in Eq. (3.35).

The calculation of the second term in Eq. (3.34), the change of electrostatic field energy, needs some manipulation. The difficulty arises from the fact that the electric energy exists in all space. So we follow a procedure similar to that used by James (2002) and divide the calculation into three steps in Sections 3.4.4 to 3.4.6. The final result is shown in Eq. (3.44).

3.4.4 Rate of Change of Field Energy: Step 1

First, by setting $\psi=\phi$ in Eq. (3.11), we have

$$\int_{\mathbb{R}^3}\epsilon_0\nabla_{\mathbf{y}}\phi\cdot\nabla_{\mathbf{y}}\phi\,dy=\int_{\mathbf{y}(\Omega)}\nabla_{\mathbf{y}}\phi\cdot\mathbf{p}\,dy+\int_{\mathbf{y}(\Omega)}\phi\,\rho\,dy+\int_{S_v}\hat{\phi}\,\sigma\,dS_y+\int_{\partial C_q}\phi\,\sigma\,dS_y\,. \tag{3.36}$$

Therefore,

$$\begin{aligned}
&\frac{d}{dt}\left[\int_{\mathbb{R}3}\epsilon_0|\nabla_{\mathbf{y}}\phi|^2\,dy\right]\\
&\quad=\frac{d}{dt}\left\{\int_{\mathbf{y}(\Omega)}\nabla_{\mathbf{y}}\phi\cdot\mathbf{p}\,dy+\int_{\mathbf{y}(\Omega)}\phi\,\rho\,dy\right\}+\hat{\phi}\frac{d}{dt}\int_{S_v}\sigma\,dS_y+\int_{\partial C_q}\dot{\phi}\,\sigma\,dS_y\\
&\quad=\frac{d}{dt}\left\{\int_{\Omega}\nabla_{\mathbf{y}}\phi\cdot\mathbf{p}_0\,dx+\int_{\Omega}\phi\,\rho_0\,dx\right\}+\hat{\phi}\frac{d}{dt}\int_{S_v}\sigma\,dS_y+\int_{\partial C_q}\dot{\phi}\,\sigma\,dS_y\\
&\quad=\int_{\Omega}\frac{d}{dt}(\nabla_{\mathbf{y}}\phi)\cdot\mathbf{p}_0\,dx+\int_{\Omega}\nabla_{\mathbf{y}}\phi\cdot\dot{\mathbf{p}}_0\,dx+\int_{\Omega}\dot{\phi}\,\rho_0\,dx+\int_{\Omega}\phi\,\dot{\rho}_0\,dx
\end{aligned}$$

$$
\begin{aligned}
&+ \hat{\phi}\frac{d}{dt}\int_{S_v} \sigma\, dS_y + \int_{\partial C_q} \dot{\phi}\,\sigma\, dS_y \\
&= \int_\Omega (\nabla_{\mathbf{y}} \overset{o}{\phi} + \mathbf{v}\cdot\nabla_{\mathbf{y}}\nabla_{\mathbf{y}}\phi)\cdot \mathbf{p}_0\, dx + \int_\Omega \nabla_{\mathbf{y}}\phi\cdot\dot{\mathbf{p}}_0\, dx \\
&\quad + \int_\Omega (\overset{o}{\phi} + \mathbf{v}\cdot\nabla_{\mathbf{y}}\phi)\,\rho_0\, dx + \int_\Omega \phi\,\dot{\rho}_0\, dx + \hat{\phi}\frac{d}{dt}\int_{S_v}\sigma\, dS_y + \int_{\partial C_q}\dot{\phi}\,\sigma\, dS_y \\
&= \int_{y(\Omega)} (\nabla_{\mathbf{y}} \overset{o}{\phi} + \mathbf{v}\cdot\nabla_{\mathbf{y}}\nabla_{\mathbf{y}}\phi)\cdot\mathbf{p}\, dy + \int_{\mathbf{y}(\Omega)} (\overset{o}{\phi} + \mathbf{v}\cdot\nabla_{\mathbf{y}}\phi)\,\rho\, dy \\
&\quad + \int_\Omega \nabla_{\mathbf{y}}\phi\cdot\dot{\mathbf{p}}_0\, dx + \int_\Omega \phi\,\dot{\rho}_0\, dx + \hat{\phi}\frac{d}{dt}\int_{S_v}\sigma\, dS_y + \int_{\partial C_q}\dot{\phi}\,\sigma\, dS_y\ . \qquad (3.37)
\end{aligned}
$$

Notice that we use the fact that C_q is the conductor with fixed charged Q in deriving the second equality.

3.4.5 Rate of Change of Field Energy: Step 2

Second, we multiply $\overset{o}{\phi}$ on both sides of Maxwell equation (3.9), and integrate over $\mathbb{R}^3$ to obtain

$$
\int_{\mathbb{R}^3} \nabla_{\mathbf{y}}\cdot(-\epsilon_0\nabla_{\mathbf{y}}\phi + \mathbf{p}\,\chi(\mathbf{y}(\Omega)))\,\overset{o}{\phi}\, dy = \int_{\mathbb{R}^3}\rho\chi(\mathbf{y}(\Omega))\,\overset{o}{\phi}\, dy\ . \qquad (3.38)
$$

We clarify that these integrals should be interpreted in classical sense rather than in the sense of distribution. The left side of Eq. (3.38) therefore can be split to three parts on which divergence theorem can be applied:

$$
\begin{aligned}
&\int_{\mathbb{R}^3} \nabla_{\mathbf{y}}\cdot(-\epsilon_0\nabla_{\mathbf{y}}\phi + \mathbf{p}\,\chi(\mathbf{y}(\Omega)))\,\overset{o}{\phi}\, dy \\
&\quad = \int_{\mathbf{y}(\Omega)} \nabla_{\mathbf{y}}\cdot(-\epsilon_0\nabla_{\mathbf{y}}\phi + \mathbf{p})\,\overset{o}{\phi}\, dy + \int_{C_q}\nabla_{\mathbf{y}}\cdot(-\epsilon_0\nabla_{\mathbf{y}}\phi)\,\overset{o}{\phi}\, dy \\
&\qquad \int_{\mathbb{R}^3\setminus(\mathbf{y}(\Omega)\cup C_q)} \nabla_{\mathbf{y}}\cdot(-\epsilon_0\nabla_{\mathbf{y}}\phi)\,\overset{o}{\phi}\, dy \\
&\quad = -\int_{\mathbf{y}(\Omega)} \nabla_{\mathbf{y}}\overset{o}{\phi}\cdot(-\epsilon_0\nabla_{\mathbf{y}}\phi + \mathbf{p})\ dy \\
&\qquad + \int_{S_v^-}\overset{o}{\phi}\,(-\epsilon_0\nabla_{\mathbf{y}}\phi + \mathbf{p})\cdot\hat{\mathbf{n}}\, dS_y + \int_{S_f^+}\overset{o}{\phi}\,(-\epsilon_0\nabla_{\mathbf{y}}\phi + \mathbf{p})\cdot\hat{\mathbf{n}}\, dS_y \\
&\qquad - \int_{C_q}\nabla_{\mathbf{y}}\overset{o}{\phi}\cdot(-\epsilon_0\nabla_{\mathbf{y}}\phi)\, dy + \int_{\partial C_q^-}\overset{o}{\phi}\,(-\epsilon_0\nabla_{\mathbf{y}}\phi)\cdot\hat{\mathbf{n}}_q\, dS_y \\
&\qquad - \int_{\mathbb{R}^3\setminus(\mathbf{y}(\Omega)\cup C_q)}\nabla_{\mathbf{y}}\overset{o}{\phi}\cdot(-\epsilon_0\nabla_{\mathbf{y}}\phi)\, dy + \int_{\partial C_q^+}\overset{o}{\phi}\,(-\epsilon_0\nabla_{\mathbf{y}}\phi)\cdot(-\hat{\mathbf{n}}_q)\, dS_y \\
&\qquad + \int_{S_v^+}\overset{o}{\phi}\,(-\epsilon_0\nabla_{\mathbf{y}}\phi)\cdot(-\hat{\mathbf{n}})\, dS_y + \int_{S_f^+}\overset{o}{\phi}\,(-\epsilon_0\nabla_{\mathbf{y}}\phi)\cdot(-\hat{\mathbf{n}})\, dS_y
\end{aligned}
$$

$$= \int_{\mathbb{R}^3} \epsilon_0 \nabla_{\mathbf{y}} \overset{o}{\phi} \cdot \nabla_{\mathbf{y}} \phi \, dy - \int_{\mathbf{y}(\Omega)} \nabla_y \overset{o}{\phi} \cdot \mathbf{p} \, dy - \int_{\partial C_q} [\![\overset{o}{\phi} (-\epsilon_0 \nabla_{\mathbf{y}} \phi)]\!] \cdot \hat{\mathbf{n}}_q \, dS_y$$
$$- \int_{S_v} [\![\overset{o}{\phi} (-\epsilon_0 \nabla_{\mathbf{y}} \phi + \mathbf{p})]\!] \cdot \hat{\mathbf{n}} \, dS_y - \int_{S_f} [\![\overset{o}{\phi} (-\epsilon_0 \nabla_{\mathbf{y}} \phi + \mathbf{p})]\!] \cdot \hat{\mathbf{n}} \, dS_y \, . \tag{3.39}$$

Here, $\hat{\mathbf{n}}$, $\hat{\mathbf{n}}_q$ are the outward unit norms of $\mathbf{y}(\Omega)$ and C_q respectively, S_v^-, S_f^- the inner surfaces of $\mathbf{y}(\Omega)$, S_v^+, S_f^+ the outer surfaces of $\mathbf{y}(\Omega)$, C_q^- and C_q^+ the inner and outer surfaces of C_q respectively. And the last equality comes from Eq. (3.15) and the fact that $\sigma = 0$ on S_f.

Since C_q is fixed in space, and $\overset{o}{\phi} = \dot{\phi}$ on C_q, Eq. (3.38) and (3.39) lead to

$$\int_{\mathbb{R}^3} \epsilon_0 \nabla_{\mathbf{y}} \phi \cdot \nabla_{\mathbf{y}} \overset{o}{\phi} \, dy = \int_{y(\Omega)} \nabla_{\mathbf{y}} \overset{o}{\phi} \cdot \mathbf{p} \, dy + \int_{\mathbf{y}(\Omega)} \overset{o}{\phi} \, \rho \, dy + \int_{\partial C_q} \dot{\phi} \, \sigma \, dS_y$$
$$+ \int_{S_v} [\![\overset{o}{\phi} (-\epsilon_0 \nabla_{\mathbf{y}} \phi + \mathbf{p})]\!] \cdot \hat{\mathbf{n}} \, dS_y + \int_{S_f} [\![\overset{o}{\phi} (-\epsilon_0 \nabla_{\mathbf{y}} \phi + \mathbf{p})]\!] \cdot \hat{\mathbf{n}} \, dS_y \, . \tag{3.40}$$

Therefore, by using Reynolds' transport theorem, we have

$$\frac{d}{dt} \left[\frac{1}{2} \int_{\mathbb{R}^3} \epsilon_0 |\nabla_{\mathbf{y}} \phi|^2 \, dy \right]$$
$$= \frac{\epsilon_0}{2} \int_{\mathbf{y}(\Omega)} \frac{\partial}{\partial t} |\nabla_{\mathbf{y}} \phi|^2 \, dy + \frac{\epsilon_0}{2} \int_{\mathbb{R}^3 \setminus (\mathbf{y}(\Omega) + C_q)} \frac{\partial}{\partial t} |\nabla_{\mathbf{y}} \phi|^2 \, dy$$
$$- \frac{\epsilon_0}{2} \int_{\partial \mathbf{y}(\Omega)} [\![\, |\nabla_{\mathbf{y}} \phi|^2]\!] \, \mathbf{v} \cdot \hat{\mathbf{n}} \, dS_y$$
$$= \int_{\mathbb{R}^3} \epsilon_0 \nabla_{\mathbf{y}} \phi \cdot \nabla_{\mathbf{y}} \overset{o}{\phi} \, dy - \frac{\epsilon_0}{2} \int_{S_v + S_f} [\![\, |\nabla_{\mathbf{y}} \phi|^2]\!] \, \mathbf{v} \cdot \hat{\mathbf{n}} \, dS_y$$
$$= \int_{\mathbf{y}(\Omega)} \nabla_{\mathbf{y}} \overset{o}{\phi} \cdot \mathbf{p} \, dy + \int_{\mathbf{y}(\Omega)} \overset{o}{\phi} \, \rho \, dy + \int_{\partial C_q} \dot{\phi} \, \sigma \, dS_y$$
$$+ \int_{S_v} [\![\overset{o}{\phi} (-\epsilon_0 \nabla_{\mathbf{y}} \phi + \mathbf{p})]\!] \cdot \hat{\mathbf{n}} \, dS_y - \frac{\epsilon_0}{2} \int_{S_v} [\![\, |\nabla_{\mathbf{y}} \phi|^2]\!] \, \mathbf{v} \cdot \hat{\mathbf{n}} \, dS_y$$
$$+ \int_{S_f} [\![\overset{o}{\phi} (-\epsilon_0 \nabla_{\mathbf{y}} \phi + \mathbf{p})]\!] \cdot \hat{\mathbf{n}} \, dS_y - \frac{\epsilon_0}{2} \int_{S_f} [\![\, |\nabla_{\mathbf{y}} \phi|^2]\!] \, \mathbf{v} \cdot \hat{\mathbf{n}} \, dS_y \, . \tag{3.41}$$

Let $S = S_v \bigcup S_f = \partial \mathbf{y}(\Omega)$. Using the jump conditions (3.15), (3.20) and (3.25), we can simplify the last four terms in Expression (3.41):

$$\int_S [\![\overset{o}{\phi} \, (-\epsilon_0 \nabla_{\mathbf{y}} \phi + \mathbf{p})]\!] \cdot \hat{\mathbf{n}} \, dS_y - \frac{\epsilon_0}{2} \int_S [\![\, |\nabla_{\mathbf{y}} \phi|^2]\!] \, \mathbf{v} \cdot \hat{\mathbf{n}} \, dS_y$$
$$= \int_S \langle \overset{o}{\phi} \rangle [\![-\epsilon_0 \nabla_{\mathbf{y}} \phi + \mathbf{p}]\!] \cdot \hat{\mathbf{n}} \, dS_y + \int_S [\![\overset{o}{\phi}]\!] \langle -\epsilon_0 \nabla_{\mathbf{y}} \phi + \mathbf{p} \rangle \cdot \hat{\mathbf{n}} \, dS_y$$

$$
\begin{aligned}
&- \epsilon_0 \int_S \langle \nabla_{\mathbf{y}} \phi \rangle [\![\nabla_{\mathbf{y}} \phi]\!] \, \mathbf{v} \cdot \hat{\mathbf{n}} \, dS_y \\
&= \int_S \overset{o}{\langle \phi \rangle} \, \sigma \, dS_y + \int_S \overset{o}{[\![\phi]\!]} \langle \mathbf{p} \rangle \cdot \hat{\mathbf{n}} \, dS_y \\
&\quad - \epsilon_0 \int_S \overset{o}{[\![\phi]\!]} \langle \nabla_{\mathbf{y}} \phi \rangle \cdot \hat{\mathbf{n}} \, dS_y - \epsilon_0 \int_S \langle \nabla_{\mathbf{y}} \phi \rangle [\![\nabla_{\mathbf{y}} \phi]\!] \, \mathbf{v} \cdot \hat{\mathbf{n}} \, dS_y \\
&= \int_S \left[\dot{\phi} - \mathbf{v} \cdot \langle \nabla_{\mathbf{y}} \phi \rangle \right] \sigma \, dS_y + \frac{1}{2\epsilon_0} \int_S (\mathbf{p} \cdot \hat{\mathbf{n}})^2 (\mathbf{v} \cdot \hat{\mathbf{n}}) \, dS_y \\
&\quad + \frac{1}{2\epsilon_0} \int_S \sigma \, (\mathbf{p} \cdot \hat{\mathbf{n}}) (\mathbf{v} \cdot \hat{\mathbf{n}}) \, dS_y \\
&= \int_S \dot{\phi} \, \sigma \, dS_y - \int_S \mathbf{v} \cdot \left[\nabla_{\mathbf{y}} \phi^- + \frac{1}{2} [\![\nabla_{\mathbf{y}} \phi]\!] \right] \sigma \, dS_y \\
&\quad + \frac{1}{2\epsilon_0} \int_S (\mathbf{p} \cdot \hat{\mathbf{n}})^2 (\mathbf{v} \cdot \hat{\mathbf{n}}) \, dS_y + \frac{1}{2\epsilon_0} \int_S \sigma \, (\mathbf{p} \cdot \hat{\mathbf{n}}) (\mathbf{v} \cdot \hat{\mathbf{n}}) \, dS_y \\
&= \int_S \dot{\phi} \, \sigma \, dS_y - \int_S \sigma \, \mathbf{v} \cdot \nabla_{\mathbf{y}} \phi^- \, dS_y \\
&\quad + \frac{1}{2\epsilon_0} \int_S \sigma (\mathbf{p} \cdot \hat{\mathbf{n}}) (\mathbf{v} \cdot \hat{\mathbf{n}}) \, dS_y + \frac{1}{2\epsilon_0} \int_S \sigma^2 (\mathbf{v} \cdot \hat{\mathbf{n}}) \, dS_y \\
&\quad + \frac{1}{2\epsilon_0} \int_S (\mathbf{p} \cdot \hat{\mathbf{n}})^2 (\mathbf{v} \cdot \hat{\mathbf{n}}) \, dS_y + \frac{1}{2\epsilon_0} \int_S \sigma \, (\mathbf{p} \cdot \hat{\mathbf{n}}) (\mathbf{v} \cdot \hat{\mathbf{n}}) \, dS_y \\
&= \int_S \dot{\phi} \, \sigma \, dS_y - \int_S \sigma \, \mathbf{v} \cdot \nabla_{\mathbf{y}} \phi^- \, dS_y + \frac{1}{2\epsilon_0} \int_S \left(\mathbf{p} \cdot \hat{\mathbf{n}} + \sigma \right)^2 (\mathbf{v} \cdot \hat{\mathbf{n}}) \, dS_y \\
&= \int_S \dot{\phi} \, \sigma \, dS_y + \int_S [\![\mathbf{T}_{\mathrm{M}} \hat{\mathbf{n}}]\!] \cdot \mathbf{v} \, dS_y \\
&= \int_S [\![\mathbf{T}_{\mathrm{M}} \hat{\mathbf{n}}]\!] \cdot \mathbf{v} \, dS_y \, . \qquad (3.42)
\end{aligned}
$$

The last equality comes from the fact that $\phi = \hat{\phi}$, thus $\dot{\phi} = 0$ on S_v, and $\sigma = 0$ on S_f.

Substituting Eq. (3.42) into Eq. (3.41), we have

$$
\begin{aligned}
\frac{d}{dt} \left[\frac{1}{2} \int_{\mathbb{R}^3} \epsilon_0 |\nabla_{\mathbf{y}} \phi|^2 \, dy \right] &= \int_{\mathbf{y}(\Omega)} \nabla_{\mathbf{y}} \overset{o}{\phi} \cdot \mathbf{p} \, dy + \int_{\mathbf{y}(\Omega)} \overset{o}{\phi} \, \rho \, dy \\
&\quad + \int_{\partial C_q} \dot{\phi} \, \sigma \, dS_y + \int_{S_v \bigcup S_f} [\![\mathbf{T}_{\mathrm{M}} \hat{\mathbf{n}}]\!] \cdot \mathbf{v} \, dS_y \, . \qquad (3.43)
\end{aligned}
$$

3.4.6 Rate of Change of Field Energy: Step 3

Now, subtracting Eq. (3.43) from Eq. (3.37), we obtain,

$$\begin{aligned}
&\frac{d}{dt}\left[\frac{1}{2}\int_{\mathbb{R}^3}\epsilon_0|\nabla_{\mathbf{y}}\phi|^2\,dy\right] \\
&\quad=\int_{\Omega}\nabla_{\mathbf{y}}\phi\cdot\dot{\mathbf{p}}_0\,dx+\int_{\Omega}\phi\,\dot{\rho}_0\,dy+\int_{\mathbf{y}(\Omega)}\mathbf{v}\cdot\nabla_{\mathbf{y}}\nabla_{\mathbf{y}}\phi\cdot\mathbf{p}\,dy \\
&\qquad+\int_{\mathbf{y}(\Omega)}\mathbf{v}\cdot\nabla_{\mathbf{y}}\phi\,\rho\,dy+\hat{\phi}\frac{d}{dt}\int_{S_v}\sigma\,dS_y-\int_{\partial\mathbf{y}(\Omega)}[\![\mathbf{T}_{\mathrm{M}}\hat{\mathbf{n}}]\!]\cdot\mathbf{v}\,dS_y\,.
\end{aligned}\tag{3.44}$$

3.4.7 Rate of Dissipation: the Final Expression

Putting together Eq. (3.30), (3.32), (3.34), (3.35), (3.44), we now have the final expression for the rate of dissipation of the whole system:

$$\begin{aligned}
\mathcal{D}&=\mathcal{F}-\frac{d\mathcal{E}}{dt} \\
&=-\int_{\Omega}\left(\nabla_{\mathbf{x}}\mu_{N_{d0}}\cdot\mathbf{J}_{N_{d0}}+\nabla_{\mathbf{x}}\mu_{\rho_{c0}}\cdot\mathbf{J}_{\rho_{c0}}\right)dx \\
&\quad+\int_{\Omega}\left[\left(\mu_{N_{d0}}-\frac{\partial W_0}{\partial N_{d0}}-ez\phi\right)\dot{N}_{d0}+\left(\mu_{\rho_c}-\frac{\partial W_0}{\partial\rho_{c0}}-\phi\right)\dot{\rho}_{c0}\right]dx \\
&\quad+\int_{\Omega}\left[\nabla_{\mathbf{x}}\cdot\left(\frac{\partial W_0}{\partial\nabla_{\mathbf{x}}\mathbf{p}_0}\right)-\frac{\partial W_0}{\partial\mathbf{p}_0}-\mathbf{F}^{-T}\nabla_{\mathbf{x}}\phi\right]\cdot\dot{\mathbf{p}}_0\,dx-\int_{\partial\Omega}\left(\frac{\partial W}{\partial\nabla_{\mathbf{x}}\mathbf{p}_0}\hat{\mathbf{m}}\right)\cdot\dot{\mathbf{p}}_0\,dS_x \\
&\quad+\int_{\mathbf{y}(\Omega)}\left[\nabla_{\mathbf{y}}\cdot\left(\frac{1}{J}\frac{\partial W_0}{\partial\mathbf{F}}\mathbf{F}^T\right)-\left(\nabla_{\mathbf{y}}\nabla_{\mathbf{y}}\phi\right)\mathbf{p}-\rho\nabla_{\mathbf{y}}\phi\right]\cdot\mathbf{v}\,dy \\
&\quad-\int_{\partial\mathbf{y}(\Omega)}\left(\frac{1}{J}\frac{\partial W_0}{\partial\mathbf{F}}\mathbf{F}^T\hat{\mathbf{n}}\right)\cdot\mathbf{v}\,dS_y \\
&\quad+\int_{\partial\mathbf{y}(\Omega)}[\![\mathbf{T}_M\hat{\mathbf{n}}]\!]\cdot\mathbf{v}\,dS_y+\int_{\partial\mathbf{y}(\Omega_s)}\mathbf{t}\cdot\mathbf{v}\,dS_y.
\end{aligned}\tag{3.45}$$

From Eq. (3.45), we can see that the dissipation of the system has three contributions: the first two integrals on the right-hand side of the equation are the dissipation caused by the diffusion of vacancies and charges, the third integral is the dissipation caused by the polarization evolution, and the remaining terms are the contribution from the deformation of the ferroelectric body.

3.5 Governing Equations

According to the second law of thermodynamics specialized to isothermal processes that we are currently considering, the rate of dissipation $\mathcal{D}$ should always be greater or equal to zero. Notice in the expression (3.45) for the rate of dissipation, each term is a product of conjugate pairs – generalized velocity (time rate of change of some quantity or flux of some quantity) times a generalized force (a quantity that depends on the state and not the rate of change of the state). Therefore we may argue as Coleman and Noll (1963) to obtain the governing equations. Specifically, by considering various processes that have the same state at some instant of time but different rates and insisting that $\mathcal{D} \geq 0$ for all these processes, we conclude that

$$\nabla_{\mathbf{x}} \left(\frac{\partial W_0}{\partial \nabla_{\mathbf{x}} \mathbf{p}_0} \right) - \frac{\partial W_0}{\partial \mathbf{p}_0} - \mathbf{F}^{-T} \nabla_{\mathbf{x}} \phi = 0 \quad \text{in} \quad \Omega, \tag{3.46}$$

$$\frac{\partial W_0}{\partial \nabla_{\mathbf{x}} \mathbf{p}_0} \hat{\mathbf{m}} = 0 \quad \text{on} \quad \partial\Omega, \tag{3.47}$$

$$\nabla_{\mathbf{y}} \cdot \left(\frac{1}{J} \frac{\partial W_0}{\partial \mathbf{F}} \mathbf{F}^T \right) - \left(\nabla_{\mathbf{y}} \nabla_{\mathbf{y}} \phi \right) \mathbf{p} - \rho \nabla_{\mathbf{y}} \phi = 0 \quad \text{in} \quad \mathbf{y}(\Omega), \tag{3.48}$$

$$\frac{1}{J} \frac{\partial W_0}{\partial \mathbf{F}} \mathbf{F}^T \hat{\mathbf{n}} - [\![\mathbf{T}_{\mathrm{M}} \hat{\mathbf{n}}]\!] - \mathbf{t} \chi(\mathbf{y}(\partial_s \Omega)) = 0 \quad \text{on} \quad \partial \mathbf{y}(\Omega) \tag{3.49}$$

and

$$\frac{\partial W_0}{\partial N_{d0}} - \mu_{N_{d0}} + ez\phi = 0 \quad \text{in} \quad \Omega, \tag{3.50}$$

$$\frac{\partial W_0}{\partial \rho_0} - \mu_{\rho_{c0}} + \phi = 0 \quad \text{in} \quad \Omega, \tag{3.51}$$

$$\mathbf{J}_{N_{d0}} \cdot \nabla_{\mathbf{x}} \mu_{N_{d0}} \leq 0 \quad \text{in} \quad \Omega, \tag{3.52}$$

$$\mathbf{J}_{\rho_{c0}} \cdot \nabla_{\mathbf{x}} \mu_{\rho_{c0}} \leq 0 \quad \text{in} \quad \Omega\,. \tag{3.53}$$

The first two equations, Eq. (3.46) and (3.47) are, respectively, the equilibrium equation of polarization and its boundary condition. Eq. (3.48) is the force equilibrium equation with boundary condition (3.49).

If we define the *Cauchy stress tensor* as

$$\boldsymbol{\sigma} = \frac{1}{J} \left(\frac{\partial W_0}{\partial \mathbf{F}} \right) \mathbf{F}^T, \tag{3.54}$$

and also notice that

$$\begin{aligned}
-\left(\nabla_{\mathbf{y}}\nabla_{\mathbf{y}}\phi\right)\mathbf{p}-\rho\nabla_{\mathbf{y}}\phi &= -\phi_{,ij}p_j-\rho\phi_{,i}\\
&= -\phi_{,ij}(D_j+\epsilon_0\phi_{,j})-\phi_{,i}D_{j,j}\\
&= -(\phi_{,ij}D_j+\phi_{,i}D_{j,j})-\epsilon_0\phi_{,ij}\phi_{,j}\\
&= (-\phi_{,i}D_j)_{,j}-(\frac{\epsilon_0}{2}\phi_{,k}\phi_{,k}\delta_{ij})_{,j}\\
&= \left(E_iD_j-\frac{\epsilon_0}{2}\left|\nabla_{\mathbf{y}}\phi\right|^2\delta_{ij}\right)_{,j}\\
&= \nabla_{\mathbf{y}}\cdot\left(\mathbf{E}\otimes\mathbf{D}-\frac{\epsilon_0}{2}\mathbf{E}\cdot\mathbf{E}\,\mathbf{I}\right)\\
&= \nabla_{\mathbf{y}}\cdot\mathbf{T}_{\mathrm{M}},
\end{aligned}$$

then Eq. (3.48) and (3.49) can then be rewritten as

$$\nabla_{\mathbf{y}}\cdot(\boldsymbol{\sigma}+\mathbf{T}_{\mathrm{M}})=0 \quad \text{in} \quad \mathbf{y}(\Omega), \tag{3.55}$$

$$\boldsymbol{\sigma}\hat{\mathbf{n}}-[\![\mathbf{T}_{\mathrm{M}}\hat{\mathbf{n}}]\!]-\mathbf{t}\chi(\mathbf{y}(\partial_s\Omega))=0 \quad \text{on} \quad \partial\mathbf{y}(\Omega)\ . \tag{3.56}$$

We make the additional constitutive assumption that

$$\mathbf{J}_{N_{d0}}=-\mathbf{K}_1\nabla_{\mathbf{x}}\mu_{N_0}, \tag{3.57}$$

$$\mathbf{J}_{\rho_{c0}}=-\mathbf{K}_2\nabla_{\mathbf{x}}\mu_{\rho_{c0}} \tag{3.58}$$

for some positive definite and symmetric tensor $\mathbf{K}_1$, $\mathbf{K}_2$ to satisfy Eq. (3.52) and (3.53). $\mathbf{K}_2$ is the conductivity of the solid and $\mathbf{K}_1$ is the diffusivity of defects.

Eq. (3.50), (3.51), (3.57), (3.58), together with the continuity equations (3.6) and (3.7), are equations concerning two diffusion processes. The first one is the diffusion of oxygen vacancies,

$$\dot{N}_{d0}=\nabla\cdot\left(\mathbf{K}_1\nabla\left(\frac{\partial W_0}{\partial N_{d0}}+ez\phi\right)\right), \tag{3.59}$$

and the second one is the diffusion of free charge,

$$\dot{\rho}_{c0}=\nabla\cdot\left(\mathbf{K}_2\nabla\left(\frac{\partial W_0}{\partial \rho_{c0}}+\phi\right)\right). \tag{3.60}$$

In summary, Eq. (3.46), (3.54), (3.55), (3.59), (3.60), plus Maxwell equation (3.9) are the governing equations subject to boundary condition (3.10), (3.47), (3.56), plus suitable

boundary and initial conditions for N_{d0} and ρ_{c0}.

We now discuss some special cases.

(i) *Transient Conduction*

The diffusion of free charges are usually much faster than the diffusion of the defects ($\min \lambda(\mathbf{K_2}) \gg \max \lambda(\mathbf{K_1})$, where $\lambda(\mathbf{K})$ is an eigenvalue of $\mathbf{K}$). By choice, we can consider phenomena on timescales on which there is no diffusion of defects but only transport of free charges. We do so by setting $\mathbf{K}_1 = \mathbf{0}$, so that $\dot{N}_{d0} = 0$ and N_{d0} is fixed and given. In this case, we have Eq. (3.46), (3.54), (3.55), (3.60), (3.9) as the governing equations, plus Eq. (3.47), (3.56), and (3.10) as their boundary conditions.

We point out that the real transportation of free carrier in semiconductors is usually more complicated than described by Eq. (3.60). In Eq. (3.60), electrons and holes are assumed to have the same mobility, which is usually not the case. Our derivation can easily be modified to account for it.

(ii) *Defect Diffusion*

We now work on a time scale appropriate for the diffusion of the defects. We do so by assuming $\mathbf{K}_2 = \infty$, so that the free charges ρ_c are always in equilibrium, or $\dot{\rho}_{c0} = 0$.

The assumption that $\mathbf{K}_2 = \infty$, $\dot{\rho}_{c0} = 0$, together with Eq. (3.60), leads to

$$\frac{\partial W_0}{\partial \rho_{c0}} + \phi = 0 \tag{3.61}$$

which may be interpreted as constitutive relation between free charge density and electric potential. If we further assume that W_0 is convex in ρ_{c0}, we can then invert Eq. (3.61) to obtain $\rho_{c0} = \rho_{c0}(\phi)$, or

$$\rho = \rho(\phi, N_d) \tag{3.62}$$

in the current configuration. As an example we shall use later, for a typical semicon-

ductor, the charge density in thermal equilibrium state is (Sze, 1981):

$$\begin{aligned}\rho(\phi, N_d) = &- eN_c F_{\frac{1}{2}}\left(\frac{E_{fm} - E_c + e\phi}{K_b T}\right) + eN_v F_{\frac{1}{2}}\left(\frac{E_v - e\phi - E_{fm}}{K_b T}\right) \\ &+ zeN_d(x)\left(1 - \frac{1}{1 + \frac{1}{2}\exp\left(\frac{E_d - e\phi - E_{fm}}{K_b T}\right)}\right) \\ &- z'eN_a(x)\left(1 - \frac{1}{1 + \frac{1}{2}\exp\left(\frac{E_{fm} + e\phi - E_a}{K_b T}\right)}\right)\end{aligned} \tag{3.63}$$

where N_c and N_v are the effective density of states in the conduction band and in the valence band respectively, E_c the energy at the bottom of the conduction band, E_v the energy on the top of the valence band, E_d, E_a the donor and acceptor level respectively, K_b the Boltzmann constant, T the absolute temperature, $F_{\frac{1}{2}}$ the Dirac-Fermi integral, and E_{fm} the Fermi level of the semiconductor. The first two terms in Eq. (3.63) calculate the electrons in conduction band and the holes in valence band respectively, while the last two terms are the contributions from donors and acceptors. We point out that E_{fm} of the semiconductor varies with its doping type and doping level. And if the semiconduction is in contact with a metal, E_{fm} should be equal to the metal's Fermi level.

Therefore, instead of solving the diffusion equation for ρ_{c0}, we only need to solve the Maxwell equation (3.9) with ρ decided by Eq. (3.63).

If further, we assume that the total number of defects is conserved in Ω, and that the diffusivity of oxygen vacancies is isotropic ($\mathbf{K_1} = k_1\mathbf{I}$), then the final diffusion equation we need to solve are

$$\dot{N}_{d0} - \nabla \cdot \left(\beta N_{d0} \nabla \left(\frac{\partial W_0}{\partial N_{d0}} + ez\phi\right)\right) = 0 \qquad \text{in } \Omega, \tag{3.64}$$

where $\beta = k_1/N_{d0}$ is the defect's mobility, with an integral constraint

$$\frac{d}{dt}\int_\Omega N_{d0}\, dx = 0\ . \tag{3.65}$$

In summary, we now need to solve Eq. (3.9), (3.46), (3.54),(3.55), (3.63), (3.64), subject to boundary conditions (3.10), (3.47), (3.56) and an integral constraint (3.65).

(iii) *Steady State*

In this case, we assume $\mathbf{K}_1 = \mathbf{0}$, and $\mathbf{K}_2 = \infty$, i.e, we assume that the defects are immobile, and free charges adjust themselves into thermal equilibrium in no time. Consequently, we only need to solve Eq. (3.9), (3.46), (3.54), (3.55), (3.63) subject to boundary conditions (3.10), (3.47) and (3.56).

(iv) *Polarization Evolution*

The polarization equation (3.46) we derived is for its equilibrium state. One way of quickly deriving equations for polarization evolution is to state that it has to overcome a dissipation of $\int_\Omega \mu \dot{\mathbf{p}}_0^2 \, dx$. Hence,

$$\mathcal{D} = \mathcal{F} - \frac{d\mathcal{E}}{dt} - \int_\Omega \mu \dot{\mathbf{p}}_0^2 \, dx \geq 0. \tag{3.66}$$

By recourse to Eq. (3.45) and the argument by Coleman and Noll (1963), we obtain,

$$(f[\mathbf{p}_0] - \mu \dot{\mathbf{p}}_0) \cdot \dot{\mathbf{p}}_0 \geq 0 \tag{3.67}$$

where

$$f[\mathbf{p}_0] = \nabla_{\mathbf{x}} \cdot \left(\frac{\partial W_0}{\partial \nabla_{\mathbf{x}} \mathbf{p}_0} \right) - \frac{\partial W_0}{\partial \mathbf{p}_0} - \mathbf{F}^{-T} \nabla_{\mathbf{x}} \phi \, . \tag{3.68}$$

Consider any process $\mathbf{p}_0(t)$ such that $\mathbf{p}_0(t_0) = \tilde{\mathbf{p}}_0$, $\dot{\mathbf{p}}_0(t_0) = \tilde{\mathbf{q}}_0 \neq 0$. We have for Eq. (3.67) that $(f[\tilde{\mathbf{p}}_0] - \mu \tilde{\mathbf{q}}_0) \cdot \tilde{\mathbf{q}}_0 \geq 0$. Now let us consider another process $\hat{\mathbf{p}}_0(t)$ with $\hat{\mathbf{p}}_0(t_0) = \tilde{\mathbf{p}}_0$, $\dot{\hat{p}}_0(t_0) = -\tilde{\mathbf{q}}_0$. Then

$$-(f[\tilde{\mathbf{p}}_0] + \mu \tilde{\mathbf{q}}_0) \cdot \tilde{\mathbf{q}}_0 = -(f[\tilde{\mathbf{p}}_0] - \mu \tilde{\mathbf{q}}_0) \cdot \tilde{\mathbf{q}}_0 - 2\mu \tilde{\mathbf{q}}_0^2 \geq 0,$$

which means

$$(f[\mathbf{p}_0] - \mu \tilde{\mathbf{q}}_0) \cdot \tilde{\mathbf{q}}_0 \leq 0 \, . \tag{3.69}$$

In view of Eq. (3.67) and (3.69), we therefore conclude:

$$f[\tilde{\mathbf{p}}_0] - \mu \tilde{\mathbf{q}}_0 = 0. \tag{3.70}$$

Since $\mathbf{p}_0$ was an arbitrary process, we conclude that

$$\mu\dot{\mathbf{p}}_0 = \nabla_{\mathbf{x}} \cdot \left(\frac{\partial W_0}{\partial \nabla_{\mathbf{x}} \mathbf{p}_0} \right) - \frac{\partial W_0}{\partial \mathbf{p}_0} - \mathbf{F}^{-T} \nabla_{\mathbf{x}} \phi \, . \tag{3.71}$$

Eq. (3.71) is a gradient flow type of equations. And this type of equations have been widely used in simulating the phase evolution problems (Gunton et al., 1972; Ahluwalia and Cao, 1991; Hu and Chen, 1997; Chen and Shen, 1998; Zhang and Bhattacharya, 2004a,b).

(v) *Linear Elasticity*

We have derived our force equilibrium equation (3.55) from a general setting with finite deformations. However, searching for a suitable constitutive relation like (3.54) and working with finite deformation is a demanding task. For some materials, like $BaTiO_3$, a small strain description often suffices.

We define the infinitesimal strain tensor

$$\boldsymbol{\varepsilon} = \frac{1}{2} \left(\nabla \mathbf{u} + (\nabla \mathbf{u})^T \right), \tag{3.72}$$

where $\mathbf{u}$ is the displacement, set $W = W(\mathbf{p}, \boldsymbol{\varepsilon})$ as in the Devonshire-Ginzburg-Landau models (Devonshire, 1949a,b, 1954). The Maxwell stress is zero in this setting, and the Cauchy stress

$$\boldsymbol{\sigma} = \frac{\partial W(\mathbf{p}, \boldsymbol{\varepsilon})}{\partial \boldsymbol{\varepsilon}}. \tag{3.73}$$

Therefore the governing equations (assuming $\mathbf{K}_2 = \infty$, $\mathbf{K}_1 = k_1 \mathbf{I}$) are given by

$$\frac{dN_d}{dt} - \nabla \cdot \left(\beta N_d \nabla \left(\frac{\partial W}{\partial N_d} + ez\phi \right) \right) = 0 \qquad \text{in} \quad \Omega, \tag{3.74}$$

$$\mu\dot{\mathbf{p}} - \nabla \left(\frac{\partial W}{\partial \nabla \mathbf{p}} \right) + \frac{\partial W}{\partial \mathbf{p}} + \nabla\phi = 0 \qquad \text{in} \quad \Omega, \tag{3.75}$$

$$\nabla \cdot \boldsymbol{\sigma} = 0 \qquad \text{in} \quad \Omega, \tag{3.76}$$

$$\nabla \cdot (-\epsilon_0 \nabla\phi + \mathbf{p}\, \chi(\Omega)) = \rho(\phi, N_d)\chi(\Omega) \quad \text{in} \quad \mathbb{R}^3, \tag{3.77}$$

together with constitutive Eq. (3.63) and (3.73), subject to appropriate boundary and initial conditions, and any other constraints like Eq. (3.65).

Chapter 4

Barium Titanate with Platinum Electrodes: Formulation

We consider perovskite ferroelectrics in this chapter and in Chapter 5. Specifically, we consider a $Pt/BaTiO_3/Pt$ structure with shorted electrodes (a slab of barium titanate with platinum electrodes on top and bottom with zero applied voltage between them as shown in Fig. 4.1) at room temperature. We assume the material properties and kinematic quantities are invariant along z direction, therefore we only work in two dimensions.

We rewrite the equations in non-dimensional form and select parameters in Section 4.1. Section 4.2 is devoted to a discussion of oxygen vacancies and the normalization of their diffusion equations. Numerical and analytical analysis are covered in Chapter 5.

For simplicity, we only consider small deformation here; therefore we do not differentiate current configuration from the reference configuration, and also ignore the Maxwell stress. This is a reasonable choice for $BaTiO_3$ where the c/a ratio for the tetragonal phase is 1.011. But note that this would be questionable for $PbTiO_3$ where the c/a ratio is about 1.064 (Mitsui et al., 1981). Finally, we assume the stored energy functional $W(N_d, \mathbf{p}, \nabla\mathbf{p}, \boldsymbol{\epsilon})$ can

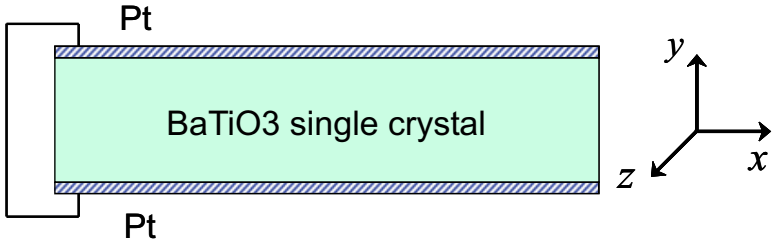

Figure 4.1: Computation domains.

be split into three parts:

$$W(N_d, \mathbf{p}, \nabla\mathbf{p}, \boldsymbol{\epsilon}) = W_d(N_d) + W_g(\nabla\mathbf{p}) + W_p(\mathbf{p}, \boldsymbol{\varepsilon}). \tag{4.1}$$

The first term is the energy of defects. The second term, associated with the polarization gradient, penalizes rapid changes of polarization. The last term is the energy of deformation and polarization, it contains important information of crystallography. Under these assumptions, the governing equations become:

$$\dot{N}_d - \nabla \cdot \left(\beta N_d \nabla \left(\frac{dW_d}{dN_d} + ez\phi \right) \right) = 0 \qquad \text{in} \quad \Omega \tag{4.2}$$

$$\mu\dot{\mathbf{p}} - \nabla \cdot \left(\frac{dW_g}{d\nabla\mathbf{p}} \right) + \frac{\partial W_p}{\partial \mathbf{p}} + \nabla\phi = 0 \qquad \text{in} \quad \Omega, \tag{4.3}$$

$$\nabla \cdot \boldsymbol{\sigma} = 0 \qquad \text{in} \quad \Omega, \tag{4.4}$$

$$\nabla \cdot (-\epsilon_0 \nabla\phi + \mathbf{p}\,\chi(\Omega)) = \rho(\phi, N_d)\chi(\Omega) \qquad \text{in} \quad \mathbb{R}^3. \tag{4.5}$$

subject to appropriate boundary and initial conditions. We point out that by splitting the stored energy functional W into three parts as in Eq. (4.1), we ignore the effect of strain/stress on the concentration of defects N_d. Consequently, the stress induced diffusion of N_d is not considered here.

We discuss the particular choices of W_g, W_p and the normalization of Eq. (4.3), (4.4), (4.5) in Section 4.1. We discuss W_d and Eq. (4.2) separately in Section 4.2.

4.1 Normalization and Parameter Selection

We choose the stored energy of polarization gradient, polarization and deformation to be the Devonshire-Ginzburg-Landau energy (Devonshire, 1949a,b, 1954) with slight modification (Zhang and Bhattacharya, 2003). Specifically, we choose W_g to be

$$W_g(\nabla\mathbf{p}) = \frac{a_0}{2} |\nabla\mathbf{p}|^2 \tag{4.6}$$

where

$$|\nabla\mathbf{p}|^2 := \nabla\mathbf{p} \cdot \nabla\mathbf{p} := \text{Trace}\left(\nabla\mathbf{p}\nabla\mathbf{p}^T\right) = p_{x,x}^2 + p_{x,y}^2 + p_{y,x}^2 + p_{y,y}^2, \tag{4.7}$$

and

$$\begin{aligned} & W_p(\mathbf{p},\boldsymbol{\varepsilon}) \\ & = \frac{a_1}{2}(p_x^2+p_y^2)+\frac{a_2}{4}(p_x^4+p_y^4)+\frac{a_3}{2}p_x^2p_y^2+\frac{a_4}{6}(p_x^6+p_y^6)+\frac{a_5}{4}(p_x^4p_y^4) \\ & - \frac{b_1}{2}(\varepsilon_{xx}p_x^2+\varepsilon_{yy}p_y^2)-\frac{b_2}{2}(\varepsilon_{xx}p_y^2+\varepsilon_{yy}p_x^2)-b_3\varepsilon_{xy}p_xp_y \\ & + \frac{c_1}{2}(\varepsilon_{xx}^2+\varepsilon_{yy}^2)+c_2\varepsilon_{xx}\varepsilon_{yy}+\frac{c_3}{2}\varepsilon_{xy}^2. \end{aligned} \tag{4.8}$$

Let $W_g' = W_g/c_0$, $W_p' = W_p/c_0$, $\mathbf{p}' = \mathbf{p}/p_0$ and $\mathbf{x}' = \mathbf{x}/L_0$, where c_0 is some constant with units of stress, L is some constant length scale, and p_0 is some constant polarization. With little effort, we can rewrite W_g' and W_p' as

$$W_g'(\nabla'\mathbf{p}') = \frac{W_g}{c_0} = \frac{a_0'}{2}\left|\nabla'\mathbf{p}'\right|^2 = \frac{a_0'}{2}({p'_{x,x}}^2+{p'_{x,y}}^2+{p'_{y,x}}^2+{p'_{y,y}}^2) \tag{4.9}$$

and

$$\begin{aligned} W_p'(\mathbf{p}',\boldsymbol{\varepsilon}) &= \frac{W_p}{c_0} \\ &= \frac{a_1'}{2}({p'_x}^2+{p'_y}^2)+\frac{a_2'}{4}({p'_x}^4+{p'_y}^4)+\frac{a_3'}{2}{p'_x}^2{p'_y}^2 \\ &\quad + \frac{a_4'}{6}({p'_x}^6+{p'_y}^6)+\frac{a_5'}{4}({p'_x}^4{p'_y}^4) \\ &\quad - \frac{b_1'}{2}(\varepsilon_{xx}{p'_x}^2+\varepsilon_{yy}{p'_y}^2)-\frac{b_2'}{2}(\varepsilon_{xx}{p'_y}^2+\varepsilon_{yy}{p'_x}^2)-b_3'\varepsilon_{xy}p'_xp'_y \\ &\quad + \frac{c_1'}{2}(\varepsilon_{xx}^2+\varepsilon_{yy}^2)+c_2'\varepsilon_{xx}\varepsilon_{yy}+\frac{c_3'}{2}\varepsilon_{xy}^2, \end{aligned} \tag{4.10}$$

where $a_0' = a_0p_0^2/c_0L_0^2$, $a_1' = a_1{p_0}^2/c_0$, $a_2' = a_2{p_0}^4/c_0$, $a_3' = a_3{p_0}^4/c_0$, $a_4' = a_4{p_0}^6/c_0$, $a_5' = a_5{p_0}^8/c_0$; $b_j' = b_j{p_0}^2/c_0$ and $c_j' = c_j/c_0$ with $j = 1,2,3$; $p'_{x,x}$ denotes $\partial p'_x/\partial x'$, and the analogous definitions apply to $p'_{x,y}$, $p'_{y,x}$ and $p'_{y,y}$. Also notice that $\nabla' = \hat{\mathbf{i}}\,\partial/\partial x' + \hat{\mathbf{j}}\,\partial/\partial y'$ in the above expression.

The obvious choice of p_0 would be the spontaneous polarization, so that the normalized spontaneous polarization is 1. For $BaTiO_3$, the spontaneous polarization in room temperature is $0.26\,\mathrm{C/m^2}$. Therefore, we choose $p_0 = 0.26\,\mathrm{C/m^2}$.

In order to choose c_0 and L_0, it is necessary to understand the role of the parameter a_0. We are interested in studying domain walls, and the classical calculation* shows that the domain wall thickness is proportional to $\sqrt{a_0/|a_1|}$. This is not surprising because a_0 (the

*A version of this calculation is shown in Section 5.3.2.1.

coefficient of $\nabla \mathbf{p}$ term) penalizes changes in polarization while a_1 is related to the steepness of the energy wells which promotes formation of domain walls. Since the energy barrier for switching from one spontaneous state to another in $BaTiO_3$ is a few MPa, while the stiffness of the material is of order 100 GPa, we choose $c_0 = 1$GPa and $L_0 = p_0\sqrt{a_0/c_0}$, so that $a_0' = 1$, and both the domain wall thickness and the normalized elastic moduli are of moderate range (10-100). This choice also has the feature that the normalized solution for the classical perfect crystal case does not depends on a_0.

However, a_0 does play a very important role in defected crystals, and therefore it is important to decide the range of a_0. From experimental data (Shilo et al., 2004) and first principle calculation (Padilla et al., 1996), people believe that the domain wall thickness is usually about $1 \sim 10$ nm, although domain wall thickness as large as 150 nm has been reported in $LiNbO_3$ (Wittborn et al., 2002). Here, we will work on two cases: $a_0 = 10^{-9}\,\mathrm{Vm^3C^{-1}}$ corresponding to a domain wall thickness of a few nanometer, and $a_0 = 10^{-7}\,\mathrm{Vm^3C^{-1}}$ for one order thicker domain walls.

Other material constants we choose are (Zhang and Bhattacharya, 2003): $c_1' = 185$, $c_2' = 111$, $c_3' = 54$, $b_1' = 1.4282$, $b_2' = -0.185$, $b_3' = 0.5886$, $a_1' = -0.007$, $a_2' = -0.009$, $a_3' = 0.003$, $a_4' = 0.0261$, $a_5' = 5$. Notice that a_1' and a_2' are both negative since the cubic to tetragonal phase transition of $BaTiO_3$ is a first order phase transition (Strukov and Levanyuk, 1998; Padilla et al., 1996).

Since we will use the finite element method to simulate the domain wall structures, it is advantageous to rewrite W_p' as

$$\begin{aligned} W_p'(\mathbf{p}', \boldsymbol{\varepsilon}) = {} & \frac{a_1'}{2}({p_x'}^2 + {p_y'}^2) + \left(\frac{a_2'}{4} - d'\right)({p_x'}^4 + {p_y'}^4) \\ & + \left(\frac{a_3'}{2} - f'\right){p_x'}^2{p_y'}^2 + \frac{a_4'}{6}({p_x'}^6 + {p_y'}^6) + \frac{a_5'}{4}({p_x'}^4{p_y'}^4) \\ & + \frac{1}{2}(\boldsymbol{\varepsilon} - \boldsymbol{\varepsilon}_s) \cdot \mathbf{C}' \, (\boldsymbol{\varepsilon} - \boldsymbol{\varepsilon}_s), \end{aligned} \tag{4.11}$$

so that the normalized stress $\boldsymbol{\sigma'} = \boldsymbol{\sigma}/c_0$ can be easily written as

$$\boldsymbol{\sigma'} = \mathbf{C}'(\boldsymbol{\varepsilon} - \boldsymbol{\varepsilon}_s), \tag{4.12}$$

where $\mathbf{C}'$ is the normalized stiffness matrix,

$$\mathbf{C}' = \begin{pmatrix} c_1' & c_2' & 0 \\ c_2' & c_1' & 0 \\ 0 & 0 & c_3' \end{pmatrix} \tag{4.13}$$

in Voigt notation, $\boldsymbol{\varepsilon}_s$ the eigenstrain caused by spontaneous polarization,

$$\boldsymbol{\varepsilon}_s = \begin{pmatrix} a' {p_x'}^2 - b' {p_y'}^2 \\ b' {p_x'}^2 - a' {p_y'}^2 \\ c' p_x' p_y' \end{pmatrix} \tag{4.14}$$

and

$$a' = \frac{b_1' c_1' - b_2' c_2'}{2({c_1'}^2 - {c_2'}^2)} = 0.0065, \tag{4.15}$$

$$b' = \frac{b_2' c_1' - b_1' c_2'}{2({c_1'}^2 - {c_2'}^2)} = -0.0044, \tag{4.16}$$

$$c' = \frac{b_3'}{c_3'} = 0.0109, \tag{4.17}$$

$$d' = \frac{-2b_1' b_2' c_2' + ({b_1'}^2 + {b_2'}^2) c_1'}{8({c_1'}^2 - {c_2'}^2)} = 0.0025, \tag{4.18}$$

$$f' = \frac{2b_1' b_2' c_1' - ({b_1'}^2 + {b_2'}^2) c_2'}{4({c_1'}^2 - {c_2'}^2)} - \frac{{b_3'}^2}{2c_3'} = -0.0005. \tag{4.19}$$

With Eq. (4.11), we can easily see the meaning of each term in the energy functional W_p'. The last term is the strain energy. The remaining part of W_p' is a polynomial of polarization, and embodies the multi-well structure corresponding to the spontaneous polarizations. Fig. 4.2 clearly shows the multi-well structure of W_p' by setting $\boldsymbol{\varepsilon} = \boldsymbol{\varepsilon}_s$ for each $\mathbf{p}$. The minima correspond to the four spontaneous states: $p_x' = \pm 1$, $p_y' = 0$ or $p_x' = 0$, $p_y' = \pm 1$. The energy barrier between different wells is $E_b' = 3.924 \times 10^{-3}$, or $E_b = 3.924\,\mathrm{MPa}$, which is about the right range for $BaTiO_3$ (Zhang, 2004a). From Eq. (4.14), we notice that the c/a ratio of the tetragonal phase of $BaTiO_3$ is $(1 + a')/(1 + b') = 1.0109$, which is consistent with experimental data. For detailed discussion of the material constants selection, refer to Zhang and Bhattacharya (2004a).

With the normalized energy functional W_g' and W_p', the normalization of Eq. (4.3) to

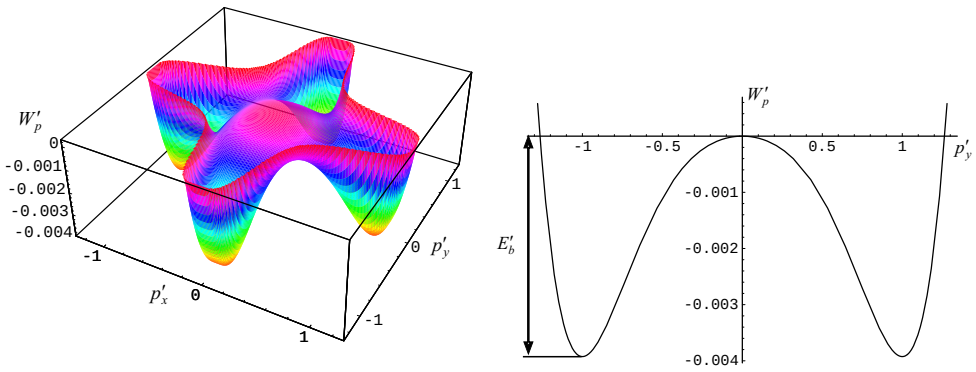

Figure 4.2: (a): Multi-well structure of normalized energy functional W'_p. (b): W'_p as a function of p'_y only when $p'_x = 0$.

Eq. (4.5) follows naturally. Let $\phi' = \phi/\phi_0$, $\rho' = \rho/\rho_0$ and $t' = t/T_0$, Eq. (4.3) to Eq. (4.5) then become:

$$\frac{\mu p_0^2}{T_0 c_0}\frac{\partial p'}{\partial t'} - \nabla' \cdot \left(\frac{dW'_g}{d\nabla' \mathbf{p}'}\right) + \frac{\partial W'_p}{\partial \mathbf{p}'} + \frac{\phi_0 p_0}{L_0 c_0}\nabla'\phi' = 0,$$

$$\nabla' \cdot \boldsymbol{\sigma}' = 0,$$

$$\nabla' \cdot (-\frac{\epsilon_0 \phi_0}{L_0 p_0}\nabla'\phi + \mathbf{p}'\,\chi(\Omega)) = \frac{L_0 \rho_0}{p_0}\rho'(\phi', N_d).$$

By choosing $\phi_0 = L_0 c_0/p_0$, $\rho_0 = p_0/L_0$, $T_0 = \mu {p_0}^2/c_0$, we obtain,

$$\mu'\frac{\partial p'}{\partial t'} - \nabla' \cdot \left(\frac{dW'_g}{d\nabla' \mathbf{p}'}\right) + \frac{\partial W'_p}{\partial \mathbf{p}'} + \nabla'\phi' = 0, \tag{4.20}$$

$$\nabla' \cdot \boldsymbol{\sigma}' = 0, \tag{4.21}$$

$$\nabla' \cdot (-\epsilon'\nabla'\phi + \mathbf{p}'\,\chi(\Omega)) = \rho'(\phi', N_d) \tag{4.22}$$

with $\mu' = 1$ and $\epsilon' = \epsilon_0\phi_0/L_0 p_0 = \epsilon_0 c_0/p_0^2$.

To summarize, we now obtain a set of normalized governing equations (Eq. (4.20) to Eq. (4.22)) which has the same form as the original set (Eq. (4.3) to Eq. (4.5)). The normalized variables are:

$$\begin{aligned} \mathbf{x}' &= \frac{\mathbf{x}}{L_0}, \quad t' = \frac{t}{T_0}, \quad W'_g = \frac{W_g}{c_0}, \quad W'_p = \frac{W_p}{c_0}, \\ \mathbf{p}' &= \frac{\mathbf{p}}{p_0}, \quad \phi' = \frac{\phi}{\phi_0}, \quad \rho' = \rho/\rho_0, \quad \boldsymbol{\sigma}' = \frac{\boldsymbol{\sigma}}{c_0} \end{aligned} \tag{4.23}$$

with characteristic constants,

$$\begin{aligned} &c_0 = 1\,\mathrm{GPa}, \quad p_0 = 0.26\,\mathrm{C/m^2}, \\ &L_0 = p_0\sqrt{\frac{a_0}{c_0}}, \quad \phi_0 = \sqrt{a_0 c_0}, \quad \rho_0 = \sqrt{\frac{c_0}{a_0}}, \quad T_0 = \frac{\mu p_0^2}{c_0}, \end{aligned} \tag{4.24}$$

and material constants,

$$\mu' = 1, \quad \epsilon' = \frac{\epsilon_0 c_0}{p_0^2} = 0.131. \tag{4.25}$$

We point out that although a_0 does not explicitly appear in the normalized equations, it is implicitly included in $\rho'(\phi')$ in Eq. (4.22) since

$$\begin{aligned} \rho'(\phi') =& \frac{1}{\rho_0}\left\{-eN_c F_{\frac{1}{2}}\left(\frac{E_{fm} - E_c + e\phi_0\phi'}{K_b T}\right) + eN_v F_{\frac{1}{2}}\left(\frac{E_v - e\phi_0\phi' - E_{fm}}{K_b T}\right)\right. \\ &+ zeN_d\left(1 - \frac{1}{1 + \frac{1}{2}\exp\left(\frac{E_d - e\phi_0\phi' - E_{fm}}{K_b T}\right)}\right) \\ &\left.-z'eN_a\left(1 - \frac{1}{1 + \frac{1}{2}\exp\left(\frac{E_{fm} + e\phi_0\phi' - E_a}{K_b T}\right)}\right)\right\} \end{aligned} \tag{4.26}$$

and ρ_0, ϕ_0 defined by Eq. (4.24) depend on a_0. For example, for $a_0 = 10^{-9}\,\mathrm{Vm^3C^{-1}}$, $\rho_0 = 10^9\,\mathrm{Cm^{-3}}$, $\phi_0 = 1\,\mathrm{V}$, while for $a_0 = 10^{-7}\,\mathrm{Vm^3C^{-1}}$, $\rho_0 = 10^8\,\mathrm{Cm^{-3}}$ and $\phi_0 = 10\,\mathrm{V}$, Therefore, the solution of normalized equations still depends on a_0, and thus depends on the physical thickness of domain walls. The only exception is when $\rho'(\phi') \equiv 0$. However even in this case, a_0 still enters itself since the size of the computational specimen depends on a_0.

We now specify the material constants we use for $BaTiO_3$ in Eq. (4.26). As we have stated before, the first two terms in Eq. (4.26) calculate the electrons in conduction band and the holes in valence band respectively, while the last two terms are the contributions from donors and acceptors. $F_{\frac{1}{2}}$ is the Dirac-Fermi integral; N_c and N_v are respectively the effective density of states in the conduction band and in the valence band, and they are approximately $1.0 \times 10^{24}\,\mathrm{m^{-3}}$ (Ashcroft and Mermin, 1976; Sze, 1981). K_b as Boltzmann constant is $1.3807 \times 10^{-23}\,\mathrm{JK^{-1}}$. T is the absolute temperature; since we work on room temperature, we choose $T = 300\,\mathrm{K}$.

The Fermi level E_{fm} of the electrodes is $-5.3\,\mathrm{eV}$. The constants of the band structure

of $BaTiO_3$ are chosen to be (Scott, 2000): $E_c = -3.6\,\text{eV}$, $E_d = -4.0\,\text{eV}$, $E_a = -6.2\,\text{eV}$, $E_v = -6.6\,\text{eV}$, where E_c is the energy at the bottom of the conduction band, E_v the energy on the top of the valence band, E_d, E_a the donor and acceptor level respectively.

As to the defects, we set $N_a = 0$ here since we are mainly interested in oxygen vacancies, which act like donors. And we estimate the oxygen vacancy density N_d as follows. For $BaTiO_3$, $a = 3.9920\,\text{Å}$, $c = 4.0361\,\text{Å}$ (Mitsui et al., 1981), therefore the volume of a unit cell is about $60\,\text{Å}^3$. Since there are 5 atoms per unit cell, the volume per atom is approximately $10\,\text{Å}^3$, thus the total atoms sites per unit volume is $N_t = 10^{29}\,\text{cm}^{-3}$. According to Zhang (2004a), the oxygen vacancy density ranges from 10 ppm to 1000 ppm, and it corresponds a N_d ranging from $10^{24}\,\text{m}^{-3}$ to $10^{27}\,\text{m}^{-3}$. The nominal valency of oxygen vacancy z is equal to 2, although the effective valency is usually less (Zhang, 2004a). We choose $z = 1$ here.

Fig. 4.3 shows the relation with $N_d = 10^{24}\,\text{m}^{-3}$ and $N_a = 0\,\text{m}^{-3}$. As we can see from Eq.(4.26), the first two terms (electrons in conduction band and holes in valence band) balance each other as long as $(E_v - E_{fm})/e < \phi < (E_c - E_{fm})/e$, or $-1.3\,\text{V} < \phi < 1.7\,\text{V}$, and the charge contribution is mainly from the donors (the third term in Eq.(4.26)). However, when $\phi > (E_c - E_{fm})/e = 1.7\,\text{V}$, because of its low energy level, electrons are attracted into the $BaTiO_3$ domain which then becomes negatively charged. On the contrary, when $\phi < (E_v - E_{fm})/e = -1.3\,\text{V}$, electrons start to flow outside the $BaTiO_3$ domain, which then becomes positively charged. Since K_bT in Eq. (4.26) equals to $0.0258\,\text{eV}$ at room temperature, a slight change of potential ϕ will result a big change of ρ. These are clearly shown in Fig. 4.3(a). If we look into the charge contribution from donors, we notice that $\phi_c = (E_d - E_{fm})/e = 1.3\,\text{V}$ is another threshold: when $\phi < \phi_c$, all the donors are ionized and the free electrons are swept into platinum side, therefore the $BaTiO_3$ domain is positively charged, and reaches a saturated value of $\rho_c = ezN_d$; when $\phi > \phi_c$, the donors are hardly ionized, and $BaTiO_3$ domain remains charge neutral. These are clearly shown in Fig. 4.3(b). We mainly work on the range when the major charge contribution comes from donors. However, as we will see later, since there is a big electrical mismatch between 90° domain walls, a potential height and well will form near the domain walls, and the first term in Eq.(4.26) starts to play an important role.

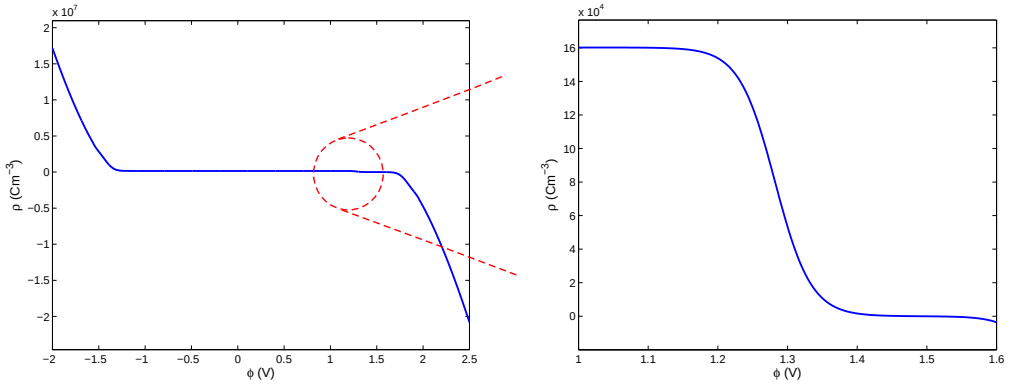

(a) (b)

Figure 4.3: Charge-potential relation in thermal equilibrium at room temperature in $BaTiO_3$ in contact with platinum with $N_d = 10^{24}\,\mathrm{m}^{-3}$ and $N_a = 0\,\mathrm{m}^{-3}$.

4.2 Diffusion of Oxygen Vacancies

For a regular binary solution of component A and B with mole Gibbs free energy G_A, G_B, mole fraction X_A, X_B, $(X_A + X_B = 1)$, the mole Gibbs free energy after mixing is (See for example, Porter and Easterling, 1981):

$$G = \hat{\mu}_A X_A + \hat{\mu}_B X_B, \tag{4.27}$$

with

$$\hat{\mu}_A = G_A + \Omega(1 - X_A)^2 + N_a K_b T \ln X_A, \tag{4.28}$$

$$\hat{\mu}_B = G_B + \Omega(1 - X_B)^2 + N_a K_b T \ln X_B, \tag{4.29}$$

and $\Omega = N_a z \epsilon$, where N_a is the Avogadro's number, z the number of bonds per atom, ϵ the energy difference between $A - B$ bond and average of $A - A$ and $B - B$ bonds. In the case of vacancies, we set

$$X_A = 1 - X_v, \qquad X_B = X_v. \tag{4.30}$$

where $X_v = N_d/N_t$ is the mole fraction of vacancies.

We are interested in mole Helmholtz free energy here since the free energy W we defined in Eq. (4.1) is Helmholtz free energy per unit volume. However, considering the fact that

we work with small deformation in a moderate stress state, it is reasonable to assume

$$W_d = \frac{N_t}{N_a} G \tag{4.31}$$

with G defined by Eq. (4.27) and Eq. (4.30). Further,

$$\frac{dW_d}{dN_d} = \frac{dW_d}{dX_v}\frac{dX_v}{dN_d} = \frac{1}{N_a}\frac{\partial G}{\partial X_B}\bigg|_{X_A} = \frac{\hat{\mu}_B}{N_a}. \tag{4.32}$$

Recalling that the equation governing the diffusion of defects (Eq. (4.2)) may be written as,

$$\dot{N}_d = -\nabla \cdot \mathbf{J}, \tag{4.33}$$

$$\mathbf{J} = -\beta N_d \nabla \left(\frac{dW_d}{dN_d} + ez\phi \right), \tag{4.34}$$

we have using Eq. (4.32) that

$$\begin{aligned}
\mathbf{J} &= -\beta \frac{N_t}{N_a} X_v \nabla \left(G_B + \Omega(1-X_v)^2 + N_a K_b T \ln X_v \right) - \beta ez N_d \nabla\phi \\
&= -\beta \frac{N_t}{N_a} X_v \left(N_a K_b T \frac{1}{X_v} \nabla X_v - 2\Omega(1-X_v)\nabla X_v \right) - \beta ez N_d \nabla\phi \\
&= -\beta K_b T \left(1 - \frac{2\Omega(1-X_v)X_v}{RT} \right) \nabla N_d - \beta ez N_d \nabla\phi \\
&= -d\nabla N_d - \beta ez N_d \nabla\phi
\end{aligned} \tag{4.35}$$

where d is the diffusion coefficient defined as

$$d = \beta K_b T \left(1 - \frac{2\Omega(1-X_v)X_v}{RT} \right) = \beta K_b T F, \tag{4.36}$$

and F is the *thermodynamic factor* defined as

$$F = 1 - \frac{2\Omega(1-X_v)X_v}{RT}, \tag{4.37}$$

where $R = N_a K_b$ is the gas constant. For dilute case, $X_v \ll 1$, F is approximately equal to 1. For simplicity, we will work only with the dilute case here.

Now, defining

$$\begin{aligned} C = X_v = \frac{N_d}{N_t}, \quad \phi' = \frac{\phi}{\phi_0}, \quad \mathbf{x}' = \frac{\mathbf{x}}{L_0}, \quad t' = \frac{t}{T_0}, \\ \mathbf{J}' = \frac{T_0}{L_0 N_t}\mathbf{J}, \quad \alpha = \frac{T_0}{L^2}d, \quad \gamma = \frac{ez\phi_0}{K_b T}, \end{aligned} \tag{4.38}$$

where L_0, ϕ_0, T_0 are defined by Eq. (4.24) in Section 4.1, we obtain,

$$\frac{\partial C}{\partial t'} = -\nabla' \cdot \mathbf{J}', \tag{4.39}$$

$$\mathbf{J}' = -\alpha \nabla' C - \alpha\gamma C \nabla' \phi'. \tag{4.40}$$

In a steady state, $\partial C/\partial t' = 0$, and $\mathbf{J}' = \text{const}$. If we further assume that $\mathbf{J}' = 0$ in the steady state, we obtain,

$$\nabla' C + \gamma C \nabla' \phi' = 0. \tag{4.41}$$

In the case of one dimension, if we assume the defect population is conserved in the computed domain $[-L, L]$, we have

$$\frac{dC}{dx'} + \gamma C \frac{d\phi'}{dx'} = 0 \tag{4.42}$$

with

$$\int_{-L}^{+L} C \, dx' = 2LC_0. \tag{4.43}$$

Or

$$C = Q \exp(-\gamma \phi') \tag{4.44}$$

with

$$Q = \frac{2LC_0}{\int_{-L}^{L} \exp(-\gamma\phi') \, dx'} \tag{4.45}$$

where C_0 is the average defect concentration.

Eq. (4.42) has an integral constraint (Eq. (4.43)). In order to solve it numerically, we first define (Ascher and Russell, 1981)

$$S = \int_{-L}^{x'} C \, dx', \tag{4.46}$$

and then add equation,

$$\frac{dS}{dx'} = C \tag{4.47}$$

and boundary conditions,

$$S(-L) = 0, \quad S(L) = 2LC_0 \tag{4.48}$$

into the original equation sets.

Finally we point out here that γ defined in Eq. (4.38) is approximately equal to $40\,\phi_0$ at room temperature with z chosen to be 1. Substituting this in Eq. (4.44), we see that a slight difference of potential ϕ will result in a huge difference in defect concentration. This poses a computational challenge, and gives rise to an almost singular Jacobian in both the collocation method and the Newton-Raphson method. At the same time, this is physically unlikely since Eq. (4.44) is based on the assumption that we are working in the dilute case and the thermodynamic factor F can be approximated by 1. Indeed, in most diffusion processes in semiconductors, the diffusion coefficient d defined Eq. (4.36) is not a constant, and it approaches to zero when the diffused species reaches a saturated value (Sze, 1981). Nevertheless, the potential difference is indeed a crucial driving force for defect redistribution, and a small potential difference does result a big difference in defect concentration. Therefore, we choose $\gamma = 4\phi_0$ for our numerical calculation here.

Chapter 5

Barium Titanate with Platinum Electrodes: Results

We continue the discussion of $Pt/BaTiO_3/Pt$ structure in this Chapter. In Section 5.1, we use the finite element method to study the detailed structure of 180^o and 90^o domain walls of the tetragonal phase. In particular, we consider a $BaTiO_3$ thin film with a 180^o or 90^o domain wall in the middle, and with shorted Platinum electrodes on both sides of the film (Fig. 5.1). The advantage of using finite element method is that the computed variable is the displacement. Most simulations in the literature use finite difference with strain as their primary variable and this requires higher regularity. The disadvantages of using displacement as primary variables is the difficulty of applying periodic boundary conditions.

We first work on perfect crystals in Section 5.1.1. We are specially interested in the strain, stress, and electric field near the domain walls. In Section 5.1.2, we investigate the possible role of oxygen vacancies on ferroelectric behavior by working on a $BaTiO_3$ crystal doped with oxygen vacancies. Through finite element simulation, we illustrate the formation of depletion layers; we also investigate the interaction of oxygen vacancies with different domain walls.

In Section 5.2, we further explore the depletion layers by working with a one-dimension situation far away from domain walls (along the y direction shown as Case A in Fig. 5.1). By numerical simulation, we study thin films with different thicknesses and doping levels in Section 5.2.1. This enables us to investigate the effects of doping level and film thickness. We also study the diffusion of oxygen vacancies to the depletion layers, and discuss its implications on ferroelectric fatigue and dielectric breakdown. In Section 5.2.2, we estimate the depletion width and approximate the potential profile in the depletion layer analytically.

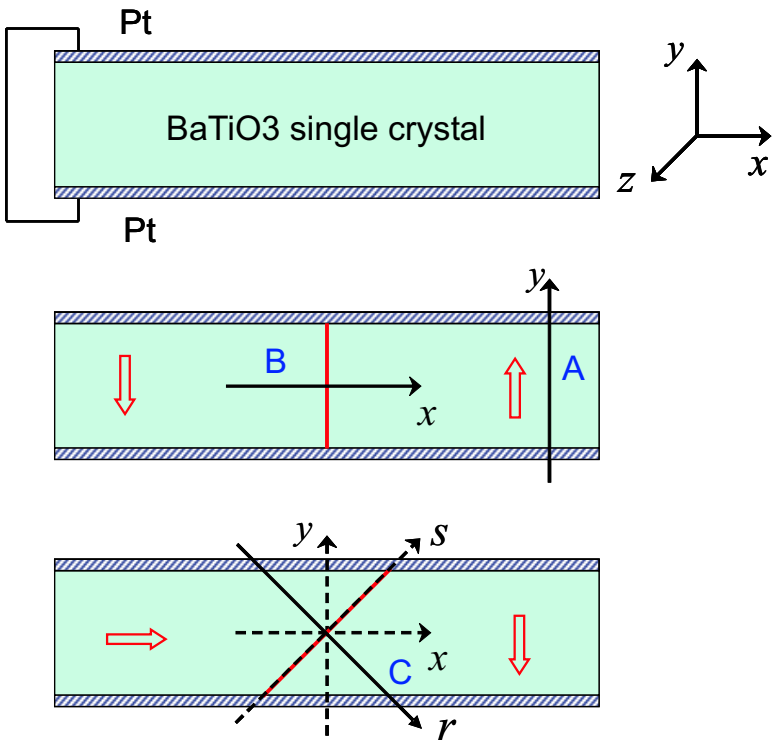

Figure 5.1: Computation domains.

The results verify the numerical simulation in Section 5.1 and Section 5.2.1.

In Section 5.3, we focus on domain walls by studying one-dimensional problems transverse to isolated domain walls: x direction for 180° walls (Case B in Fig. 5.1) and r direction for 90° domain walls (Case C in Fig. 5.1). Our analysis clearly shows the essential differences between 180° and 90° domain walls, the formation of electronic double layers at 90° domain walls, and redistribution of oxygen vacancies near 90° domain walls.

5.1 Domain Walls in a Thin Film

5.1.1 Domain Walls in Perfect Crystals

We consider a $Pt/BaTiO_3/Pt$ structure with shorted electrodes at room temperature (Fig. 5.1). We first consider $BaTiO_3$ without defects, so $\rho'(\phi') \equiv 0$ in Eq. (4.22).

We compute on a 800×200 rectangular domain corresponding to a single crystal whose pseudocubic axes are parallel to the edges of the domain. The boundary conditions we choose are: upper or lower boundary shorted, no flux at left and right side; no rotation/reflection allowed, no displacement at left lower corner point, no x displacement along

left side, and stress free elsewhere. We start with an initial guess (an ideal domain wall) for an 180^o or a 90^o domain wall in the middle of specimen, and then let it relax until it reaches its equilibrium state.

Fig. 5.2 is the polarization profile cross 180^o and 90^o domain walls through the mid-section ($y = 100$). It is easy to see that the relaxed domain walls have finite thickness.

Figs. 5.3 and 5.4 are the strain and stress field near 180^o and 90^o domain walls. It is easy to see that the strain/stress are raised near the domain walls, and concentrated at the intersections of domain walls with electrodes (not shown). These strain/stress concentration sites may likely serve as starting points for microcracking or domain wall pinning. It is also interesting to notice that there is not much difference in terms of magnitude of stress concentration between 180^o and 90^o domain walls. This is a little surprising, since the conventional wisdom states that 90^o domain walls undergo much more distortion than 180^o domain walls.

Fig. 5.5 is the deformed configuration near 180^o and 90^o domain walls. Compared to 180^o domain wall, 90^o domain wall does undergo much larger distortion. However, most of the deformation comes from the rigid rotation caused by the matching of two differently oriented domains. This does not contribute extra strain or stress, and therefore it is consistent with same level of stress and strain concentration in 180^o and 90^o domain walls. The computed angle of the rigid rotation in $BaTiO_3$ is about 0.6^o, and it can be verified by a simple calculation. We also point out that the displacement profile of 90^o domain walls can be used to identify the location of the domain walls due to the large rotation. This has been experimentally realized in $PbTiO_3$ by Shilo et al. (2004) through atomic force microscopy.

Fig. 5.6 is the potential profile across 180^o and 90^o domain walls. We notice that the potential change across 90^o domain wall is one order of magnitude larger than the potential change across 180^o domain walls. This tells us that 90^o domain walls indeed have much larger electrical mismatch than 180^o domain walls. It is exactly this electrical mismatch which makes a 90^o domain walls a plausible site for electronic charge trapping as we will see in Section 5.1.2.

5.1.2 Domain Walls in an Oxygen-Vacancy Doped Crystal

We now turn our attention to $BaTiO_3$ with defects. We still consider the $Pt/BaTiO_3/Pt$ structure, but with oxygen vacancies in $BaTiO_3$. For simplicity, we look at a single snap-

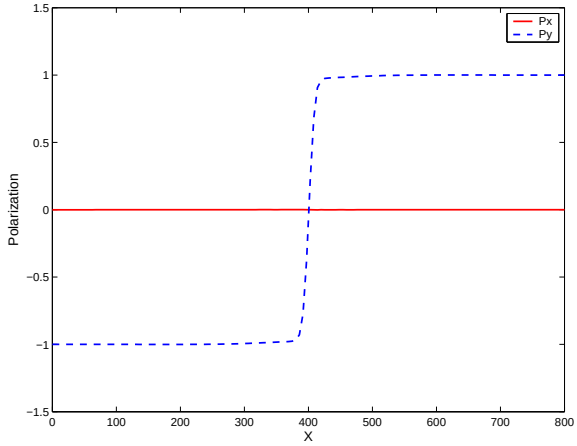

(a)

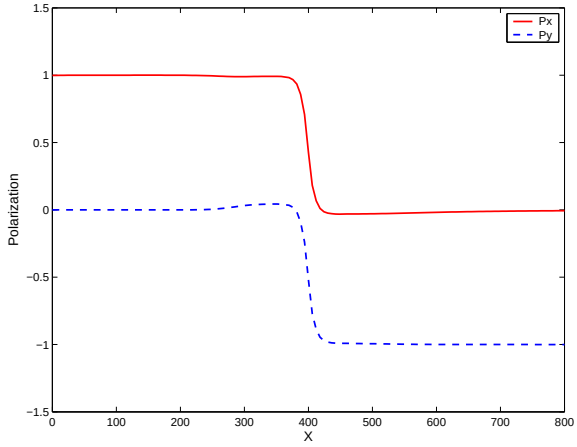

(b)

Figure 5.2: Polarization profile near (a) 180° and (b) 90° domain wall at $y = 100$.

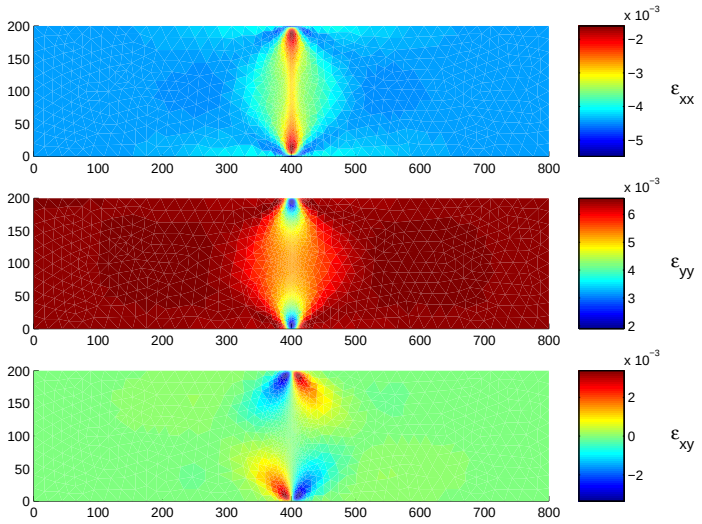

(a)

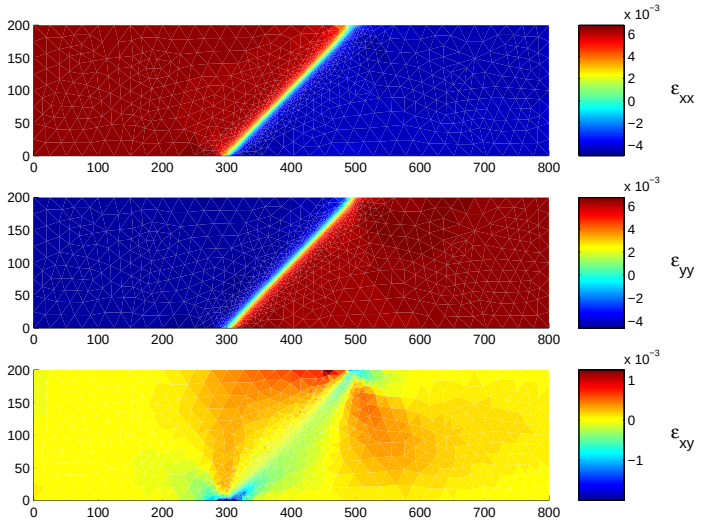

(b)

Figure 5.3: Strain profile near (a) 180° and (b) 90° domain wall.

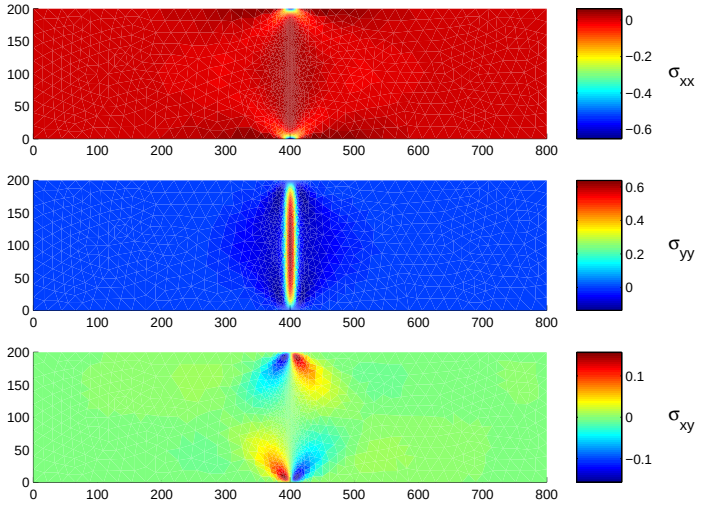

(a)

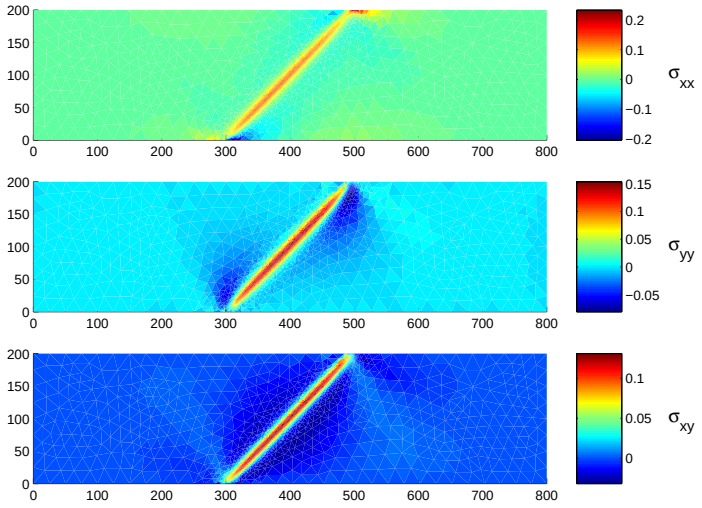

(b)

Figure 5.4: Stress profile near (a) 180^o and (b) 90^o domain wall(GPa).

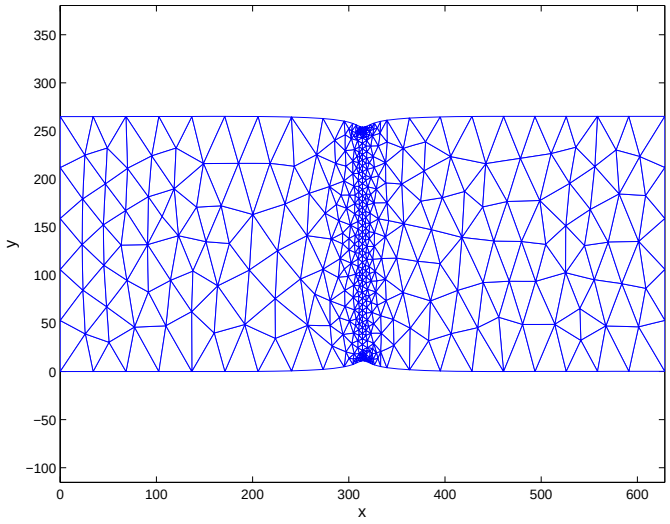

(a)

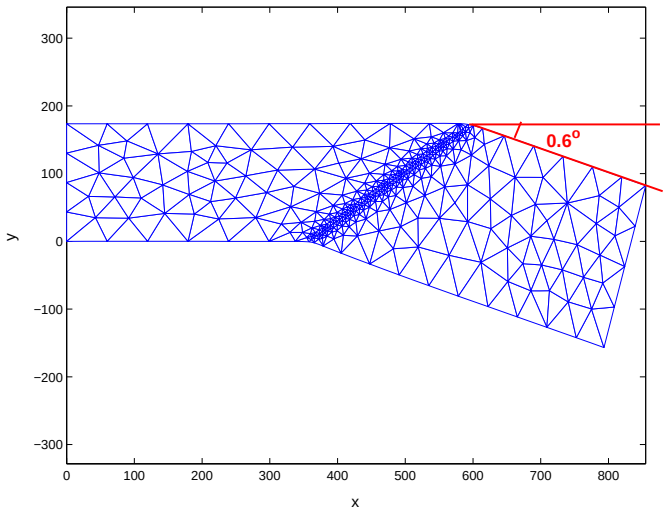

(b)

Figure 5.5: Deformed configuration near (a) 180° domain wall with amplification factor=50 and (b) 90° domain wall with amplification factor=30.

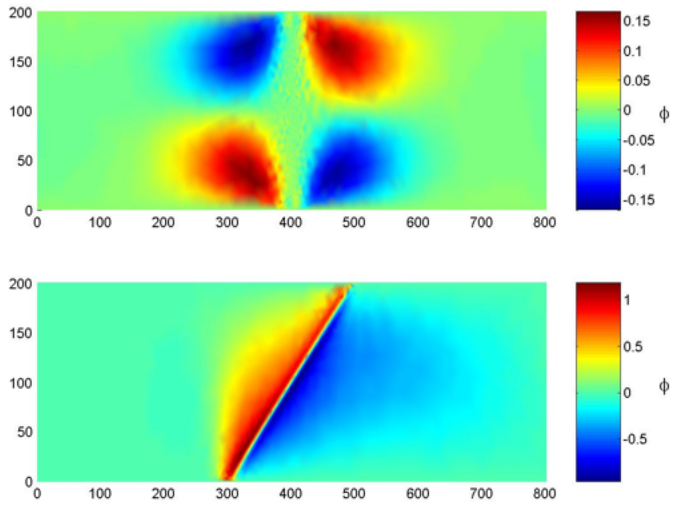

Figure 5.6: Electric potential near 180° (upper) and 90° (lower) domain walls. The real value of ϕ depends on a_0, the number (Volt) shown here is by choosing $a_0 = 1.0 \times 10^{-7}\,\mathrm{Vm^3C^{-1}}$.

shot in time when the oxygen vacancy concentration is uniform, and also ignore the effects of elasticity. Therefore, the equations reduce to

$$\mu' \frac{\partial \mathbf{p}'}{\partial t'} - \nabla' \left(\frac{dW_g'}{d\nabla' \mathbf{p}'} \right) + \frac{\partial W_p'}{\partial \mathbf{p}'} + \nabla' \phi' = 0 \qquad \text{in} \quad \Omega, \tag{5.1}$$

$$\nabla' \cdot (-\epsilon' \nabla' \phi' + \mathbf{p}'\, \chi(\Omega)) = \rho'(\phi') \quad \text{in} \quad \mathbb{R}^3 \tag{5.2}$$

with W_g' defined by Eq. (4.9), W_p' defined by Eq. (4.11) with $\boldsymbol{\varepsilon} = \boldsymbol{\varepsilon}_s$ and $\rho'(\phi')$ defined by Eq. (4.26) with $N_a = 0$ and $N_d = 1.0 \times 10^{24}\mathrm{m}^{-3}$.

We first investigate the electrostatic consequences of the interaction between the oxygen vacancies and domain walls. Still using the finite element method, we compute a 400×200 rectangular domain, with a 180° or a 90° domain wall in the middle. We choose the coefficient of $\nabla \mathbf{p}$ term a_0 to be $1.0 \times 10^{-7}\,\mathrm{Vm^3C^{-1}}$, the film thickness is therefore about 520 nm.

The computational result is shown in Fig. 5.7. The first difference we immediately notice from the case with no defects (Fig. 5.6) is the sharp rise in electrostatic potential from the electrodes to the interior of the film by as much as 1.5 V. This is caused by the the diffusion of electrons from $BaTiO_3$ into Pt giving rise to "depletion layers" of approximate thickness of 100 nm. These depletion layers also generate the Schottky barriers across the interfaces.

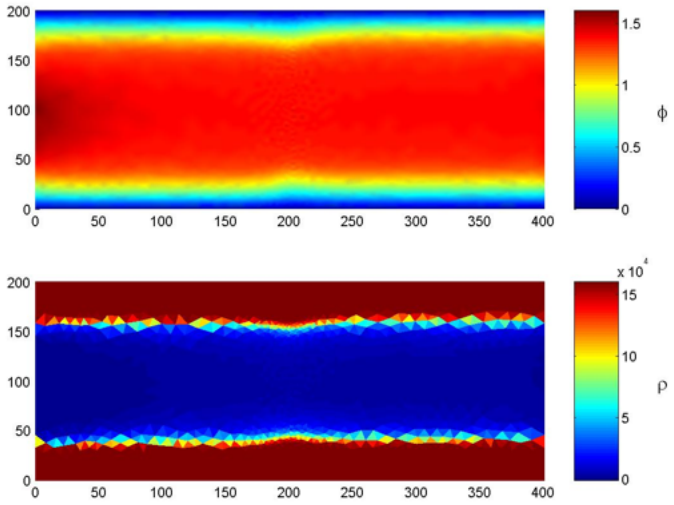

(a)

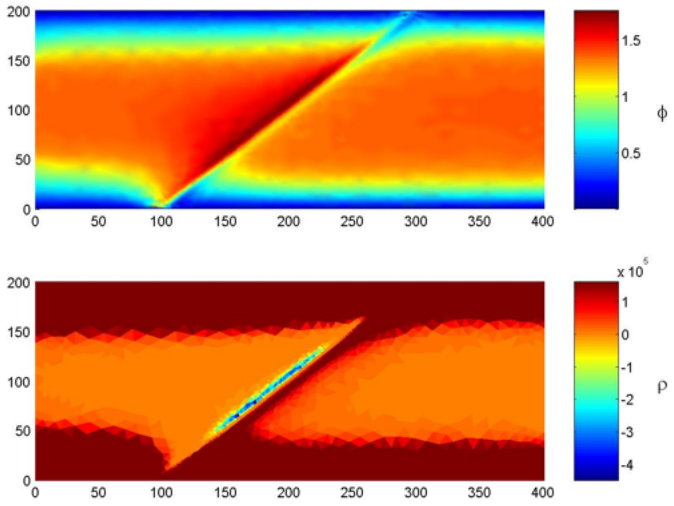

(b)

Figure 5.7: Electric potential (V) and charge densities ($\mathrm{C\,m^{-3}}$) near 180°(a) and 90°(b) domain walls

The Schottky barriers are important in preventing dielectric breakdown by resisting the injection of charges into the ferroelectric. As we shall see later in Section 5.2.3, the large electric field in the depletion layer however provides a driving force for the field-driven diffusion of oxygen vacancies. This in turn reduces the depletion layer width and promotes electronic charge tunneling which may accelerate dielectric breakdown.

In the case of the 180° domain walls (Fig. 5.7(a)), the depletion layer overwhelms any contribution from the domain wall and we barely notice the domain wall in either the distribution of potential or charges. Thus we conclude that 180° domain walls has very little interaction with the space charges. In turn, we will see in Section 5.3.3 that 180° domain wall has little effect on oxygen vacancies and their diffusion.

In contrast, there is a significant interaction between 90° domain walls and the space charges as shown in Fig. 5.7(b). We see the depletion layers as before, but we also see that very large amounts of negative charges are accumulated along the domain wall. In other words, we have electrons injected from electrodes and trapped at the domain wall at equilibrium. The reason for this can be understood by going back to the the electric potential in Fig. 5.6 without defects and noting the large electric field at the domain wall. This drives the injection of charges into the domain wall. Despite this, an electric field remains at the domain wall as shown in Fig. 5.7 and this in turn can force the diffusion of oxygen vacancies and lead to pinning of domain walls. We will examine this later in Section 5.3.3.

In summary, we find that the field caused by the depletion layers near the electrodes can promote oxygen vacancy diffusion and reduce the depletion layer thickness which may cause electronic charge tunnelling. We also find that 90° domain walls can contribute to dielectric breakdown by promoting the injection of charges and to fatigue by pinning of domain walls.

5.2 Depletion Layers

We now study in detail the depletion layers caused by electrodes away from domain walls. It is sufficient to study this problem only in one dimension, i.e., the thickness or y direction shown as Case A in Fig. 5.1, and assume $\partial/\partial x = 0$. For simplicity, we assume $p_x = 0$, and consider only the polarization along y direction, and denote it as p'. With no elasticity

being considered, the system equations are now:

$$\frac{d^2p'}{dy'^2} - \frac{dW'_p}{dp'} - \frac{d\phi'}{dy'} = 0, \tag{5.3}$$

$$-\epsilon' \frac{d^2\phi'}{dy'^2} + \frac{dp'}{dy'} = \rho'(\phi', N_d). \tag{5.4}$$

with

$$W'_p = \frac{a'_1}{2}p'^2 + \left(\frac{a'_2}{4} - d'\right)p'^4 + \frac{a'_4}{6}p'^6 \tag{5.5}$$

as shown in Fig. 4.2(b).

5.2.1 Effects of Film Thickness, Doping Level and a_0

We begin by studying the situation when the oxygen vacancy concentration is uniform. This problem is the same as that studied by Shenoy and Bhattacharya (2004) except they consider p-type dopants. Our results are very similar but for a change of sign in ρ and ϕ.

We show the polarization, potential, and charge profiles with different doping level, film thickness and a_0 in Fig. 5.8, 5.9, 5.10. Fig. 5.8 is for low concentrations with $N_d = 10^{24}\,\mathrm{m}^{-3}$; Fig. 5.9 is for medium doping with $N_d = 10^{25}\,\mathrm{m}^{-3}$; and Fig. 5.10 is for films with doping level as high as $N_d = 10^{26}\,\mathrm{m}^{-3}$. In these figures, left columns are computed results with $a_0 = 10^{-9}\,\mathrm{Vm^3C^{-1}}$, and right columns are computed results with $a_0 = 10^{-7}\,\mathrm{Vm^3C^{-1}}$. The solid blue lines are for thin films about 13 nm thick, the green dashed lines are for medium thick films with thickness equal to 52 nm, and the red dash-dot lines are for thick film with thickness equal to 520 nm.

Let us first examine the low-doping case when $N_d = 10^{24}\,\mathrm{m}^{-3}$. From Fig. 5.8, we can see that when the film is thin (blue solid and green dashed lines), all the donors across the film are ionized, and the free electrons are swept into the electrodes. The whole film is therefore fully depleted and the charge density reaches a saturated value of $\rho_c = eN_d = 1.6 \times 10^5\,\mathrm{Cm}^{-3}$. Due to the small amount of free electrons, the built-in potentials are relatively small, and the whole films remain in the regime of $0 < \phi < \phi_c$. However things are quite different in the thick film (red dash-dot lines). Because relatively large amount of free electrons are available and swept into electrodes, the built-in potential starts to reach the critical value of $\phi_c = 1.3\,\mathrm{V}$, and the donors inside the films remain unionized. As a result, depletion layers about 100 nm wide are formed near the electrodes, and the middle

part of the film remains almost charge neutral. This is consistent with our two-dimension simulation in Section 5.1.2, where we work with the same doping level and the same film thickness ($N_d = 10^{24}\,\mathrm{m}^{-3}$ and $L = 520\,\mathrm{nm}$). Finally we notice that when the films are thin, the polarization across the films changes only slightly and linearly around its spontaneous value $p_0 = 0.26\,\mathrm{Cm}^{-2}$; however, when the film thickness increases, polarization starts to have large derivation from p_0 and changes nonlinearly.

For the medium-doping case with $N_d = 10^{25}\,\mathrm{m}^{-3}$ (Fig. 5.9), things are very similar to what we have discussed in the low-doping case. In particular, we notice that the depletion layers in the thick film decreases with increased doping level. Also, the built-in potential in the film starts to reach the saturated value of built-in potential $\phi_{bi} = 1.5\,\mathrm{V}$ which we have discussed in Section 4.1 and will further investigate in Section 5.2.2.

Fig. 5.10 shows the the polarization, potential, and charge profiles for highly doped films with $N_d = 10^{26}\,\mathrm{m}^{-3}$. We see dramatic changes of the profiles in the medium and thick film cases. Compared to the low-doping and medium doping cases, the first difference we notice is the charged layer in the middle of the film. For the medium film thickness, polarization changes linearly from negative to positive; while in the thick film, a head-to-head domain pattern occurs. In these cases, the films lose their ferroelectricity, and become more like nonlinear dielectric or paraelectric. It can actually be proved that the critical doping level and film thickness when the loss of ferroelectricity occurs are related to the energy barrier E_b of the ferroelectrics (Shenoy and Bhattacharya, 2004).

Finally, we examine the effect of a_0 on the film properties. We do not see much differences by comparing the left columns of Fig. 5.8, 5.9, 5.10 where $a_0 = 10^{-9}\,\mathrm{Vm}^3\mathrm{C}^{-1}$ to the right columns where $a_0 = 10^{-7}\,\mathrm{Vm}^3\mathrm{C}^{-1}$. The only exception is the high-doping cases, where polarization varies significantly across the film. However, even in these cases, no essential and qualitative changes are observed. This is reasonable considering the fact that a_0 only penalizes the rapid changes of polarization, and does not effect the charge-potential relation directly.

5.2.2 Potential Profile and Depletion Layer Width

We now derive approximate analytic description of the profile of the electric potential and estimate the depletion layer width. As discussed in Section 4.1 and shown in Section 5.2.1, the free electrons on $BaTiO_3$'s side flow into Pt side which has a lower energy, creating a

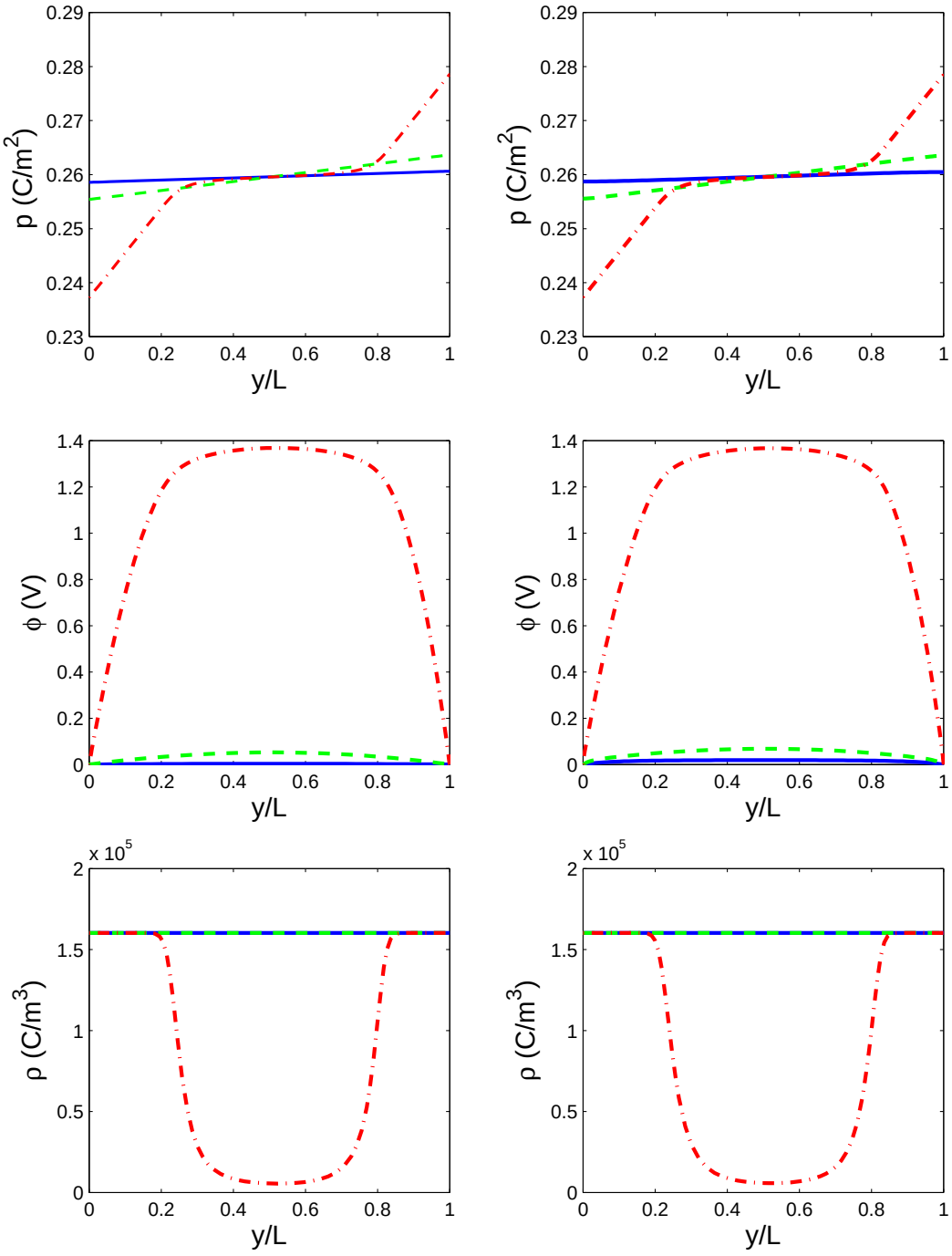

(a)

Figure 5.8: Polarization, potential, and charge profiles of films with $N_d = 10^{24}\,\mathrm{m}^{-3}$. Left column: $a_0 = 10^{-9}\,\mathrm{Vm^3C^{-1}}$, right column: $a_0 = 10^{-7}\,\mathrm{Vm^3C^{-1}}$. Blue solid lines: $L = 13\,\mathrm{nm}$; green dashed lines: $L = 52\,\mathrm{nm}$; red dash-dot lines: $L = 520\,\mathrm{nm}$.

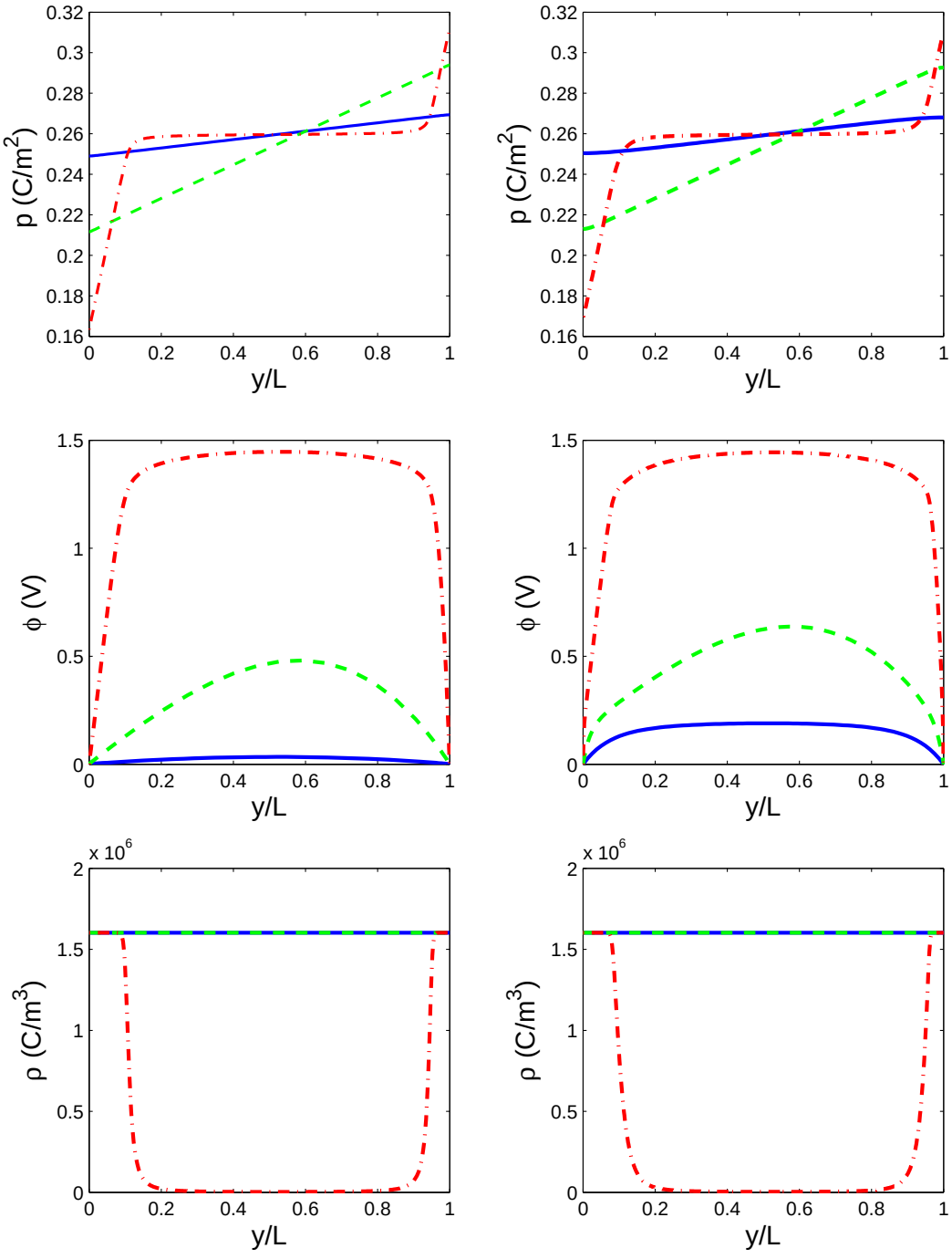

(a)

Figure 5.9: Polarization, potential, and charge profiles of films with $N_d = 10^{25}\,\mathrm{m}^{-3}$. Left column: $a_0 = 10^{-9}\,\mathrm{Vm^3C^{-1}}$, right column: $a_0 = 10^{-7}\,\mathrm{Vm^3C^{-1}}$. Blue solid lines: $L = 13\,\mathrm{nm}$; green dashed lines: $L = 52\,\mathrm{nm}$; red dash-dot lines: $L = 520\,\mathrm{nm}$.

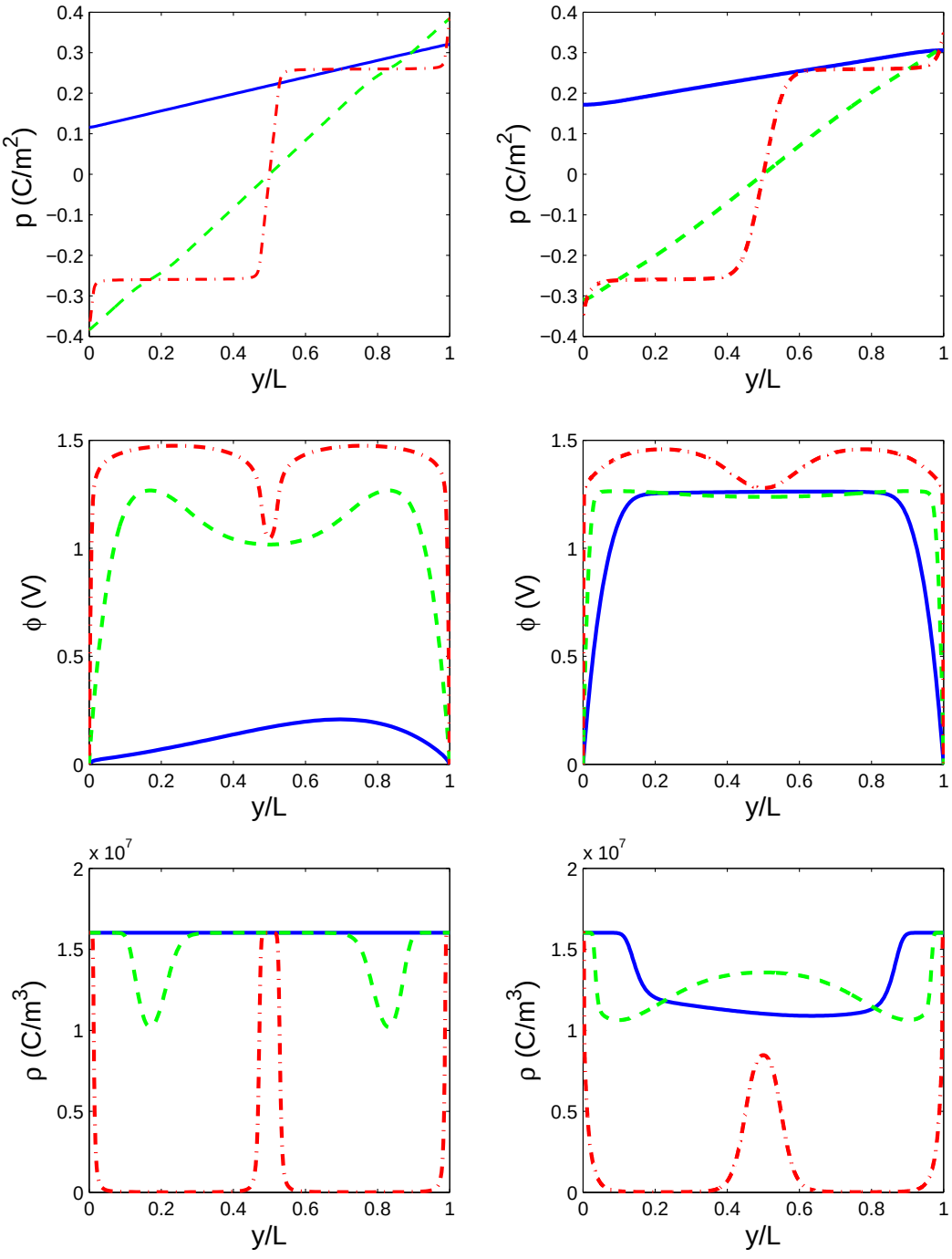

(a)

Figure 5.10: Polarization, potential, and charge profiles of films with $N_d = 10^{26}\,\mathrm{m}^{-3}$. Left column: $a_0 = 10^{-9}\,\mathrm{Vm^3C^{-1}}$, right column: $a_0 = 10^{-7}\,\mathrm{Vm^3C^{-1}}$. Blue solid lines: $L = 13\,\mathrm{nm}$; green dashed lines: $L = 52\,\mathrm{nm}$; red dash-dot lines: $L = 520\,\mathrm{nm}$.

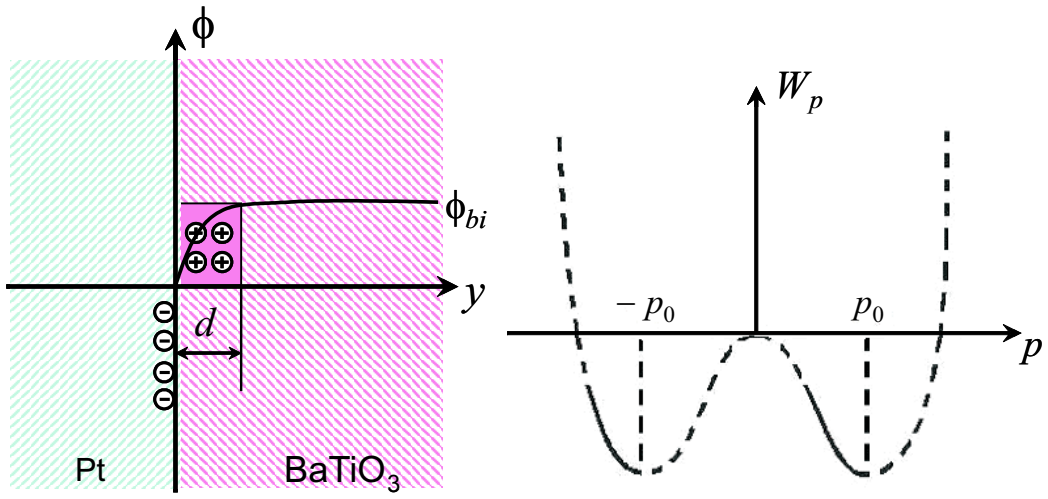

(a) (b)

Figure 5.11: (a): Potential profile across Pt/n-type $BaTiO_3$ interface. (b): Double well energy for ferroelectric crystal: the reversal of the solid line is the potential profile in the depletion layer on the left.

positive charged depletion layer near the interface on $BaTiO_3$ side and a built-in potential $\phi_{bi} = 1.5\,\mathrm{V}$. The potential profile is shown schematically in Fig. 5.11(a).

We consider the interface of a half-infinite $BaTiO_3$ slab in contact with a platinum slab. We denote d as the depletion layer width. Since the material is charge neutral deep inside the $BaTiO_3$ domain, in order to estimate the thickness of the depletion layer, we assume $\rho = 0$ outside the depletion layer and $\rho = \rho_c = ezN_d$ inside the depletion layer. We also assume that ϕ reaches the built-in potential ϕ_{bi} after the depletion layer. These are consistent with our discussion at the end of Section 4.1. From the numerical simulation in Section 5.2.2, we know that a_0 doesn't effect the properties of depletion layer significantly, therefore we ignore the gradient term here. Putting the assumption together, we solve the following equations:

$$-\epsilon_0 \phi_{,yy} + p_{,y} = \rho, \tag{5.6}$$

$$\frac{dW_p(p)}{dp} + \phi_{,y} = 0 \tag{5.7}$$

with

$$\rho = \begin{cases} ezN_d & \text{if} \quad 0 < y < d, \\ 0 & \text{if} \quad y > d, \end{cases} \tag{5.8}$$

and

$$\phi(0) = 0, \quad \phi(d) = \phi_{bi}. \tag{5.9}$$

For a dielectric semiconductor, since $W_p(p) = p^2/(2\chi\epsilon_0)$ or $p = \epsilon_0 \chi E$ with χ being the electric susceptibility, the above equation is easy to solve and the answer is well known. The width of depletion layer in this case is (Sze, 1981)

$$d = \sqrt{\frac{2\epsilon_r \epsilon_0 \phi_{bi}}{\rho}} = \sqrt{\frac{2\epsilon_r \epsilon_0 \phi_{bi}}{ezN_d}} \tag{5.10}$$

where $\epsilon_r = 1 + \chi$ is the relative dielectric constant.

For a ferroelectric semiconductor, however, things are not so straightforward. Since ϵ_0 is small, we follow Shenoy and Bhattacharya (2004) and neglect that term in Eq. (5.6) and solve:

$$p_{,y} = \rho, \tag{5.11}$$

$$\frac{dW_p(p)}{dp} + \phi_{,y} = 0 \tag{5.12}$$

with $W_p(p)$ the usual polynomial with double-well shape as in Fig. 5.11(b). It is easy to see that $p = \rho y + k_1$, where k_1 is some constant. And

$$\begin{aligned} \phi(y) &= \int -\frac{dW_p}{dp}(\rho y + k_1)\, dy + k_2 = \int -\frac{dW_p}{dp}\frac{dy}{dp} dp + k_2 \\ &= -\frac{1}{\rho} W_p(\rho y + k_1) + k_2 \end{aligned} \tag{5.13}$$

where k_2 is some constant. Therefore, the potential profile across the depletion layer looks like the inverted graph of W_p near its potential well (the solid line in Fig. 5.11(b)).

Assuming that far from the interface, we have $p = p_0$ (or $p = -p_0$ depending on the polarization direction), we obtain

$$p = p_0 + \rho(y - d) \quad \text{when} \quad 0 < y < d. \tag{5.14}$$

Therefore, we have

$$\phi(0) = -\frac{1}{\rho} W_p(p_0 - \rho d) + k_2 = 0, \tag{5.15}$$

$$\phi(d) = -\frac{1}{\rho} W_p(p_0) + k_2 = \phi_{bi}, \tag{5.16}$$

which leads to:

$$\phi_{bi}\rho = W(p_0 - \rho d) - W(p_0). \tag{5.17}$$

We perform a Taylor expansion of the right-hand-side and note that for a ferroelectric crystal with $W_p(p)$ as described by Fig. 5.11(b), $\partial W_p/\partial p(p_0) = 0$. We conclude,

$$d = \sqrt{\frac{2\phi_{bi}}{\rho}\left(\left.\frac{\partial^2 W_p}{\partial p^2}\right|_{p_0}\right)^{-1}} = \sqrt{\frac{2\phi_{bi}}{ezN_d}\left(\left.\frac{\partial^2 W_p}{\partial p^2}\right|_{p_0}\right)^{-1}}. \tag{5.18}$$

This is similar to the result for a dielectric semiconductor if we set*:

$$\epsilon_r = \left(\left.\frac{\partial^2 W_p}{\partial p^2}\right|_{p_0} \epsilon_0\right)^{-1}. \tag{5.19}$$

With the material constants we have chosen for $BaTiO_3$, $\epsilon_r \approx 113$. If $N_d = 1.0 \times 10^{24}\,\mathrm{m}^{-3}$, then the depletion layer is about 100 nm thick, which agrees with our computation results in Section 5.1.2 and Section 5.2.1. Finally we point out that as the oxygen vacancy concentration N_d increases, so does ρ resulting in a reduction of d and an increase of electronic charge injection. We can therefore conclude that increasing oxygen vacancy concentration near the electrodes makes it susceptible to failure.

5.2.3 Oxygen Vacancy Diffusion in Depletion Layers

We now consider the same problem of depletion layers considered in Section 5.2.1; however, we now allow the oxygen vacancies to be mobile. In fact we study the equilibrium situation following the methods described in Section 5.1.2.

The results for a film with low doping level are shown in Fig 5.12, and compared with the previous calculation with immobile defects. The polarization and potential profiles are similar. However a large number of oxygen vacancies accumulate at the electrodes creating a significant charge concentration there. Further the depletion layer becomes thinner (con-

* $\left(\left.\frac{\partial^2 W_p}{\partial p^2}\right|_{p_0} \epsilon_0\right)^{-1}$ is actually equal to the electric susceptibility χ, but since $\chi \gg 1$, we may set $\epsilon_r = \chi + 1 \approx \chi$.

sistent with the calculation in Section 5.2.2). We conclude that mobile vacancies can lead to significant charge injection into the ferroelectric and make it even more susceptible to failure.

This situation becomes worse when the (average) dopant concentration is increased as shown in Fig. 5.13. Even though $N_d = 10^{25}\,\mathrm{m}^{-3}$ here, the film behaves as if $N_d = 10^{25}\,\mathrm{m}^{-3}$ if it were uniform.

5.3 Structure of Isolated Domain Walls

In Section 5.1.1, our numerical results showed that in a perfect $BaTiO_3$ crystal, the potential change across 90° domain wall is one order larger than the potential change across 180° domain walls. We also showed in Section 5.1.2 that compared to 180° domain walls, 90° domain walls play a much more active role in the interaction with defects and a pronounced charge trapping occurs near the 90° domain walls. In this section, we examine this further. Specifically, we examine a region of the ferroelectric containing one or more domain walls that is far away from the electrodes. Thus we isolate the effects of the domain wall from the depletion layer. Further, since the domain wall are planar defects, it suffices to study the problem in one dimension transverse to the domain wall.

5.3.1 System Equations in One Dimension

For 180° domain walls, we work in the x direction and assume $\partial/\partial y = 0$ (Case B in Fig. 5.1). For 90° domain walls, we work in the r direction and assume $\partial/\partial s = 0$ (Case C in Fig. 5.1). We confine ourselves to the region away from the electrodes in both cases. For simplicity, we only consider steady state. We also ignore elasticity here. As we have shown in Section 5.1.2, strain as a second order parameter in the para-ferro phase transition does not play a key role in our problem.

By choosing

$$W = \frac{a_0}{2}\left|\nabla \mathbf{p}\right|^2 + W_p(\mathbf{p}) \tag{5.20}$$

where

$$W_p = \frac{a}{2}(p_x^2 + p_y^2) + \frac{b}{2}p_x^2 p_y^2 + \frac{c}{4}\left(p_x^4 + p_y^4\right) \tag{5.21}$$

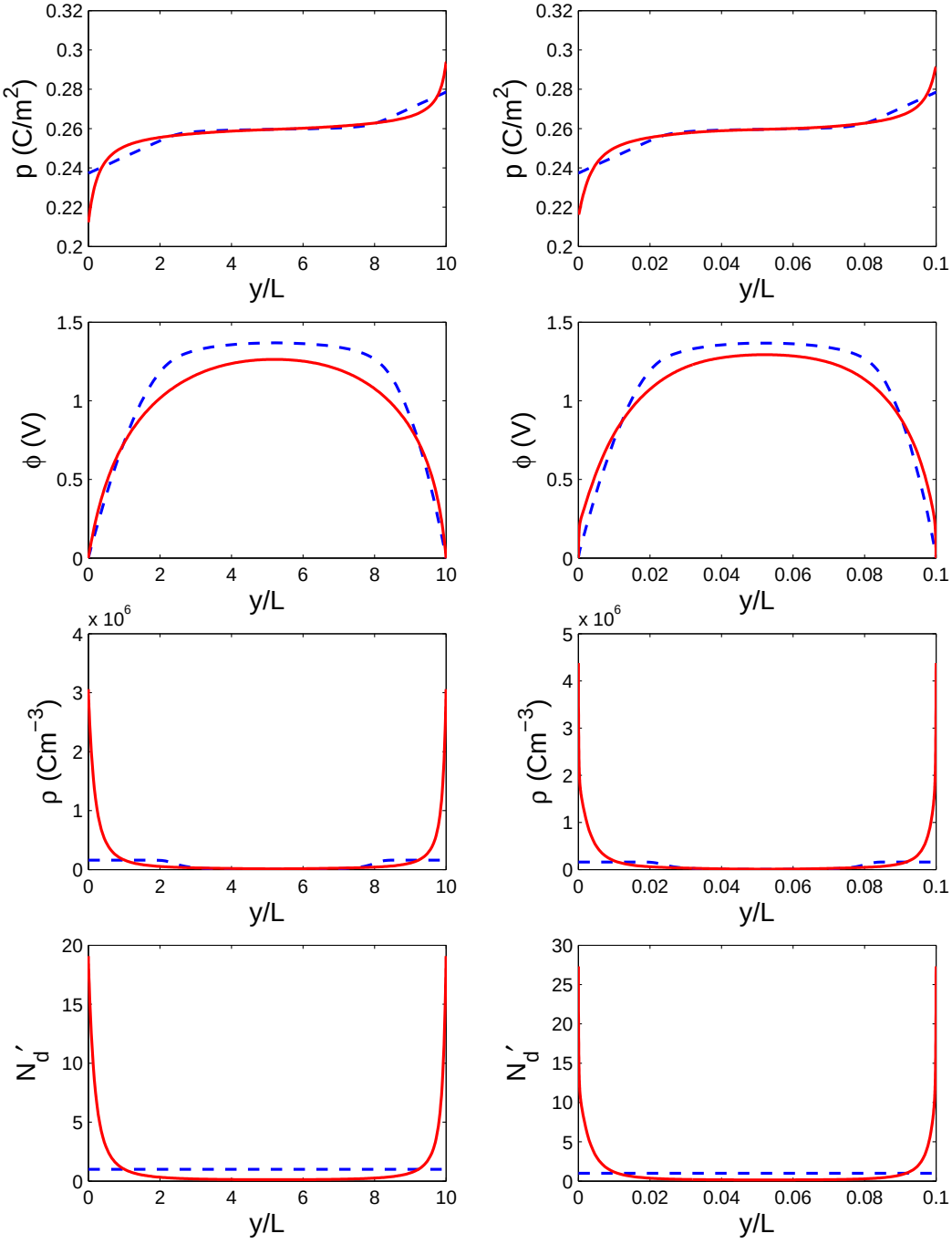

(a)

Figure 5.12: Depletion layers in films with average $N_d = 10^{24}\,\mathrm{m}^{-3}$ and $L = 520\,\mathrm{nm}$. Left column: $a_0 = 10^{-9}\,\mathrm{Vm^3C^{-1}}$, right column: $a_0 = 10^{-7}\,\mathrm{Vm^3C^{-1}}$. Blue dashed lines: w/o diffusion; red solid lines: with diffusion.

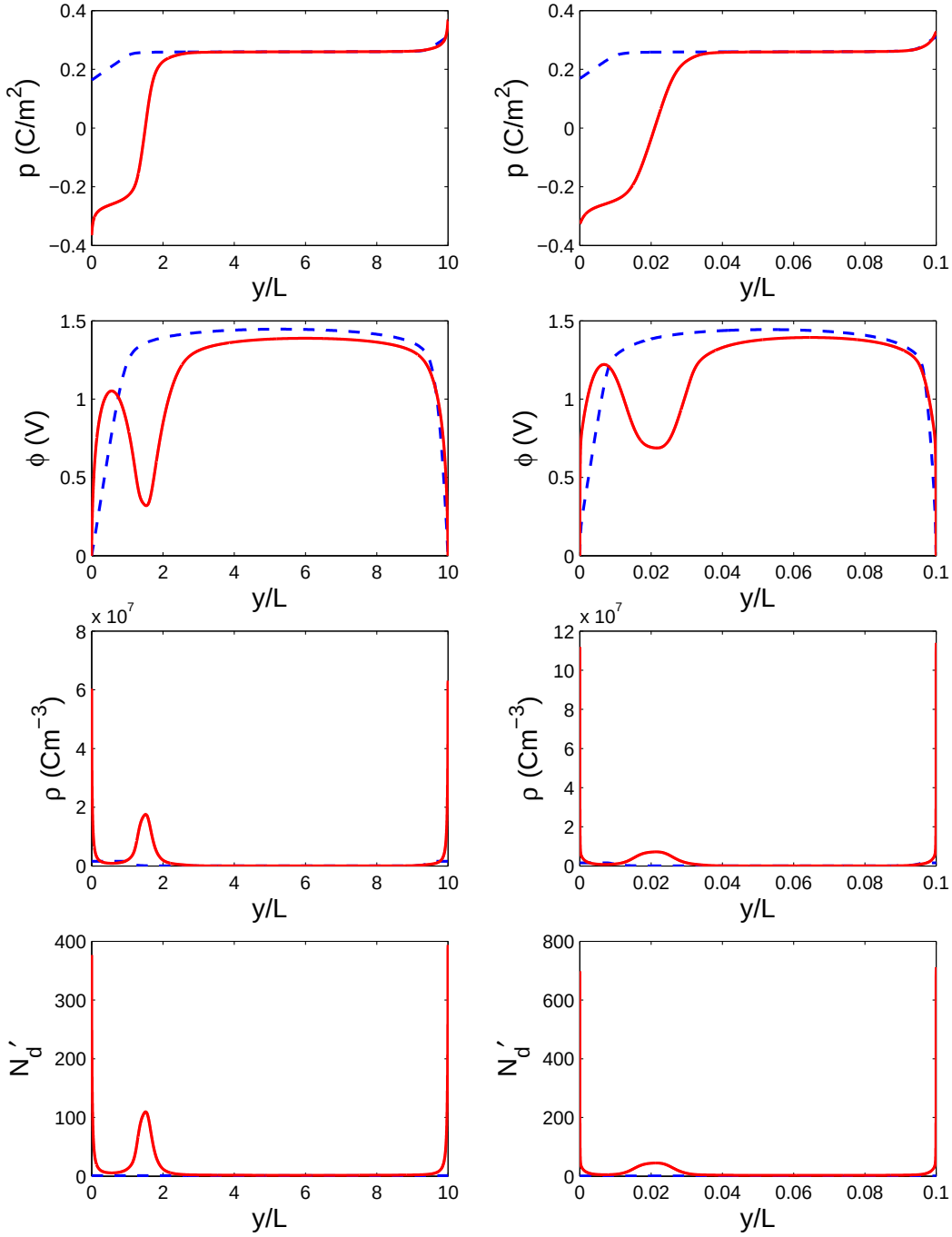

(a)

Figure 5.13: Depletion layers in films with average $N_d = 10^{25}\,\mathrm{m}^{-3}$ and $L = 520\,\mathrm{nm}$. Left column: $a_0 = 10^{-9}\,\mathrm{Vm^3C^{-1}}$, right column: $a_0 = 10^{-7}\,\mathrm{Vm^3C^{-1}}$. Blue dashed lines: w/o diffusion; red solid lines: with diffusion.

with $a < 0$, $c > 0$, the simplified two-dimensional equations become

$$a_0 \Delta \mathbf{p} - \frac{\partial W_p}{\partial \mathbf{p}} - \nabla \phi = 0 \qquad \text{in} \quad \Omega, \tag{5.22}$$

$$\nabla \cdot (-\epsilon_0 \nabla \phi + \mathbf{p}) = \rho(\phi) \qquad \text{in} \quad \Omega. \tag{5.23}$$

with suitable boundary conditions for $\mathbf{p}$ and ϕ. This particular choice of W_p is for simplicity, and is appropriate for crystals like PZT which undergo second-order para-ferro phase transitions. At the same time, we believe that it captures the essential features and the results are representative even for materials like $BaTiO_3$.

We follow the same normalization process as in Section 4.1 (Eq. (4.23)) except we define the normalized energy function W_p' as

$$W_p' = \frac{W_p}{E_b} \tag{5.24}$$

where $E_b = a^2/4c$ is the energy barrier between different wells. Therefore, the normalized variables are

$$\mathbf{x}' = \frac{\mathbf{x}}{L_0}, \quad \mathbf{p}' = \frac{\mathbf{p}}{p_0}, \quad \phi' = \frac{\phi}{\phi_0}, \quad \rho' = \frac{\rho}{\rho_0} \tag{5.25}$$

with characteristic constants,

$$\begin{aligned} &E_b = \frac{a^2}{4c}, \quad p_0 = \sqrt{\frac{-a}{c}}, \\ &L_0 = p_0 \sqrt{\frac{a_0}{E_b}}, \quad \phi_0 = \sqrt{a_0 E_b}, \quad \rho_0 = \sqrt{\frac{E_b}{a_0}}. \end{aligned} \tag{5.26}$$

The reason we choose E_b to normalize W_p instead of c_0 as in Eq. 4.23 is because we do not consider elasticity here. By choosing E_b, we obtain a normalized energy functional W_p' of order unity, and therefore a domain wall thickness of order unity.

The normalized system equations now are:

$$\Delta' \mathbf{p}' - \frac{\partial W_p'}{\partial \mathbf{p}'} - \nabla \phi' = 0 \qquad \text{in} \quad \Omega, \tag{5.27}$$

$$\nabla \cdot (-\epsilon' \nabla \phi' + \mathbf{p}') = \rho'(\phi') \qquad \text{in} \quad \Omega \tag{5.28}$$

with W'_p defined as

$$W'_p(p'_x, p'_y) = \frac{a'}{2}({p'_x}^2 + {p'_y}^2) + \frac{b'}{2}{p'_x}^2{p'_y}^2 + \frac{c'}{4}\left({p'_x}^4 + {p'_y}^4\right) \tag{5.29}$$

where $a' = -4$, $c' = -a' = 4$, and $b' = 4b/c = 20$ if we choose $b/c = 5$ for a good approximation to real crystals.

A very important parameter in Eq. (5.28) is ϵ' defined as

$$\epsilon' = \frac{\epsilon_0 E_b}{p_0^2} \tag{5.30}$$

If we pick $p_0 = 0.26\,\mathrm{C/m^2}$ as of $BaTiO_3$, and $E_b = 5 \times 10^6\,\mathrm{Jm^{-3}}$ which is about the same order as of the one we pick for $BaTiO_3$ in Section 4.1, then $\epsilon' = 6.54 \times 10^{-4}$. We notice that $\epsilon' \ll 1$, while the remaining terms in Eq. (5.27) and Eq. (5.28) are all of $O(1)$ except $\rho'(\phi')$ which varies dramatically with ϕ'. In addition to numerical solutions to the full set of equations, we will use the fact that $\epsilon' \ll 1$ to perform an asymptotic analysis.

We now write down the full one-dimensional equations. For 180° domain walls, by assuming $\partial/\partial y' = 0$, from equation Eq. (5.27) and Eq. (5.28), we obtain,

$$\frac{d^2 p'_x}{dx'^2} - \frac{\partial W'_p}{\partial p'_x} - \frac{d\phi'}{dx'} = 0, \tag{5.31}$$

$$\frac{d^2 p'_y}{dx'^2} - \frac{\partial W'_p}{\partial p'_y} = 0, \tag{5.32}$$

$$-\epsilon' \frac{d^2\phi'}{dx'^2} + \frac{dp'_x}{dx'} = \rho'(\phi'). \tag{5.33}$$

with suitable boundary conditions and W'_p defined by Eq. (5.29).

For 90° domain walls, by assuming $\partial/\partial s' = 0$, we obtain,

$$\frac{d^2 p'_r}{dr'^2} - \frac{\partial W'_p}{\partial p'_r} - \frac{d\phi'}{dr'} = 0, \tag{5.34}$$

$$\frac{d^2 p'_s}{dr'^2} - \frac{\partial W'_p}{\partial p'_s} = 0, \tag{5.35}$$

$$-\epsilon' \frac{d^2\phi'}{dr'^2} + \frac{dp'_r}{dr'} = \rho'(\phi'). \tag{5.36}$$

with suitable boundary conditions and W'_p defined by Eq. (5.29) with

$$p'_x = \frac{\sqrt{2}}{2}p'_r + \frac{\sqrt{2}}{2}p'_s, \tag{5.37}$$

$$p'_y = -\frac{\sqrt{2}}{2}p'_r + \frac{\sqrt{2}}{2}p'_s. \tag{5.38}$$

5.3.2 Structure of Domain Walls without Defects

5.3.2.1 180° Domain Walls

To understand the structure of a 180° domain wall, we seek a "kink" solution for Eq. (5.31)–(5.33) with $\rho' = 0$ which satisfies the following boundary conditions:

$$\frac{dp'_x}{dx'}(\pm\infty) = 0, \tag{5.39}$$

$$\frac{dp'_y}{dx'}(\pm\infty) = 0, \tag{5.40}$$

$$\frac{d\phi'}{dx'}(\pm\infty) = 0, \tag{5.41}$$

and in the form of a 180° domain wall located at $x' = 0$. By the last condition, we mean that p'_x should approximate to 0 at infinity, while p'_y should approximately be -1 at one end and 1 at the other.

Since

$$\frac{\partial W'_p}{\partial p'_x} = p'_x\left(a' + c'{p'_x}^2 + b'{p'_y}^2\right), \tag{5.42}$$

a solution with

$$p'_x \equiv 0 \quad \text{and} \quad \phi' \equiv 0 \tag{5.43}$$

satisfies Eq. (5.31), Eq. (5.33), and boundary condition (5.39) and (5.41). We only need to solve Eq. (5.32) which is now

$$\frac{d^2p'_y}{dx'^2} - p'_y(a' + c'{p'_y}^2) = 0 \tag{5.44}$$

by substituting $p'_x = 0$ into

$$\frac{\partial W'_p}{\partial p'_y} = p'_y\left(a' + b'{p'_x}^2 + c'{p'_y}^2\right). \tag{5.45}$$

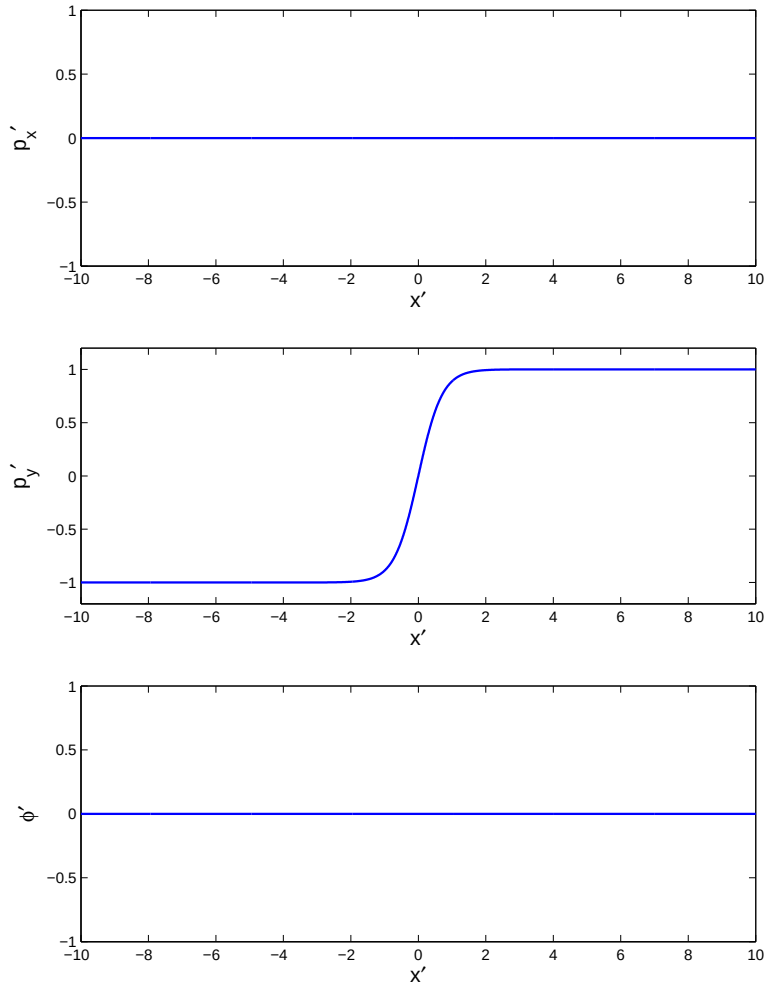

Figure 5.14: Structure of an 180° domain wall without defects.

Eq. (5.44) has an exact solution

$$p'_y = \tanh\left(\frac{x'}{\sqrt{-2/a'}}\right) = \tanh\left(\sqrt{2}\,x'\right) \tag{5.46}$$

which satisfies boundary condition (5.40) and has a 180° domain wall located at $x' = 0$.

In summary, for a 180° domain wall in perfect crystal, the polarization and potential profile is

$$p'_x = 0, \quad p'_y = \tanh\left(\sqrt{2}\,x'\right), \quad \text{and} \quad \phi' = 0. \tag{5.47}$$

This is shown in Fig. 5.14.

We notice that ϕ' here can actually be any constant since ϕ appears in our problem only in the form of $d\phi'/dx'$. Therefore, the solution also holds when we have an equally fixed

potential at both ends. When the infinite domain is replaced by a finite domain $[-L, L]$, the solution still holds approximately as long as $L \gg \sqrt{-2/a'}$.

Finally we point out that the polarization profile of 180° domain walls we obtain here is by no means new. Indeed, Cao and Cross (1991) has worked out the solution for a first order phase transition. However, in their approach, although they considered the effects of strain energy, they ignored electric field energy completely, i.e., no Maxwell equation is solved. Although the omission of electric field energy leads to the same solution for 180° domain walls, for 90° domain walls, it results in the loss of some essential information as we will show next.

5.3.2.2 90° Domain Walls

For a 90° domain wall, we seek a "kink" solution for Eq. (5.34)–(5.36) with $\rho' = 0$ which satisfies the following conditions:

$$\frac{dp'_r}{dr'}(\pm\infty) = 0, \tag{5.48}$$

$$\frac{dp'_s}{dr'}(\pm\infty) = 0, \tag{5.49}$$

$$\frac{d\phi'}{dr'}(\pm\infty) = 0, \tag{5.50}$$

and in the form of a 90° domain wall located at $r' = 0$. By the last condition, we mean that p'_r should approximately be $\sqrt{2}/2$ or $-\sqrt{2}/2$ at both ends, while p'_s should approximately be $-\sqrt{2}/2$ at one end and $\sqrt{2}/2$ at the other.

Since

$$\frac{\partial W'_p}{\partial p'_r} = p'_r \left(a' + \frac{b' + c'}{2} {p'_r}^2 + \frac{3c' - b'}{2} {p'_s}^2 \right), \tag{5.51}$$

unlike 180° domain walls, a solution with

$$p'_r \equiv \frac{\sqrt{2}}{2} \quad \text{and} \quad \phi' \equiv 0 \tag{5.52}$$

does not satisfy Eq. (5.34) and Eq. (5.36) simultaneously. As we will see later, this is actually the essential difference between 180° and 90° domain walls.

The above problem can be solved by numerical simulation, and the results are shown in Fig. 5.15. Note that there is a drop in potential across the domain wall. This is consistent

with our two dimensional solution in Fig. 5.6. This potential drop across the 90° domain wall is different from the 180° domain wall and is the essential difference between the two. To understand this further, we recall that $\epsilon' \ll 1$, and seek a perturbative solution by assuming that:

$$\begin{aligned} \phi' &\sim \phi'_0 + \epsilon' \phi'_1, \\ p'_r &\sim p'_{r0} + \epsilon' p'_{r1}, \\ p'_s &\sim p'_{s0} + \epsilon' p'_{s1}. \end{aligned} \tag{5.53}$$

We obtain the following equations at $O(1)$:

$$\frac{d^2 p'_{r0}}{dr'^2} - \left.\frac{\partial W'_p}{\partial p'_{r0}}\right|_{p'_{r0},\, p'_{s0}} - \frac{d\phi'_0}{dr'} = 0, \tag{5.54}$$

$$\frac{d^2 p'_{s0}}{ds'^2} - \left.\frac{\partial W'_p}{\partial p'_{s0}}\right|_{p'_{r0},\, p'_{s0}} = 0, \tag{5.55}$$

$$\frac{dp'_{r0}}{dr'} = 0. \tag{5.56}$$

And the equations at $O(\epsilon')$ are

$$\frac{d^2 p'_{r1}}{dr'^2} - \left.\frac{\partial^2 W'_p}{\partial {p'_r}^2}\right|_{p'_{r0},\, p'_{s0}} p'_{r1} - \left.\frac{\partial^2 W'_p}{\partial p'_r \partial p'_s}\right|_{p'_{r0},\, p'_{s0}} p'_{s1} - \frac{d\phi'_1}{dr'} = 0, \tag{5.57}$$

$$\frac{d^2 p'_{s1}}{ds'^2} - \left.\frac{\partial^2 W'_p}{\partial p'_r \partial p'_s}\right|_{p'_{r0},\, p'_{s0}} p'_{r1} - \left.\frac{\partial^2 W'_p}{\partial {p'_s}^2}\right|_{p'_{r0},\, p'_{s0}} p'_{s1} = 0, \tag{5.58}$$

$$-\frac{d^2 \phi'_0}{dr'^2} + \frac{dp'_{r1}}{dr'} = 0. \tag{5.59}$$

The solution of the $O(1)$ equations can be worked out without much effort:

$$\begin{aligned} p'_{r0} &\equiv p_m, \\ p'_{s0} &= -A \tanh(Br'), \\ \phi'_0 &= Cr' + D \tanh(Br') + \phi_m \end{aligned} \tag{5.60}$$

where

$$A = \sqrt{\frac{-2a' + (b' + 3a')p_m^2}{b' - a'}} \tag{5.61}$$

$$B = \frac{1}{2}\sqrt{-2a' + (b' + 3a')p_m^2} \tag{5.62}$$

$$C = \frac{2a(b' + a')}{b' - a'} p_m(-1 + 2p_m^2) \tag{5.63}$$

$$D = \frac{-(b' + 3a')}{b' - a'} p_m \sqrt{-2a' + (b' + 3a')p_m^2} \tag{5.64}$$

and p_m, ϕ_m are some constants decided by boundary conditions (Eq. (5.48), Eq. (5.49), Eq. (5.50) with p'_r, p'_s, ϕ' being replaced by p'_{r0}, p'_{s0} and ϕ'_0 respectively). We therefore have

$$p_m = \frac{\sqrt{2}}{2}, \quad A = \frac{\sqrt{2}}{2}, \quad B = \sqrt{3}, \quad C = 0, \quad D = -\frac{\sqrt{6}}{3} \tag{5.65}$$

and ϕ_m can be any constant.

With the equations of $O(1)$ solved, we now turn to the equations of $O(\epsilon')$. p'_{r1} can be solved easily from Eq. (5.59),

$$p'_{r1} = DB \sec(Br'). \tag{5.66}$$

The other two equations of $O(\epsilon')$ are however quite messy, and can not easily be solved analytically. Fortunately, numerical simulation shows that the first order approximation of p'_s and ϕ' is good enough to capture the essential profiles. Fig. 5.15 shows the numerical solution of the exact equation (5.34)-(5.36) and compares it with the perturbation solution ($p'_{r0} + \epsilon' p'_{r1}$, p'_{s0} and ϕ'_0).

In light of the potential drop across the domain wall, the potential does not vanish at infinity. To explore this further, we consider a finite domain $[-L, L]$ with fixed potential at both ends: $\phi'(\pm L) = 0$. In order to satisfy the boundary, we have

$$-CL + D\tanh(-BL) + \phi_m = 0,$$
$$CL + D\tanh(BL) + \phi_m = 0,$$

which leads to:

$$\phi_m = 0, \tag{5.67}$$

$$CL + D\tanh(BL) = 0. \tag{5.68}$$

Therefore, in order to find p_m, we only need to solve an algebraic equation (Eq. (5.68)).

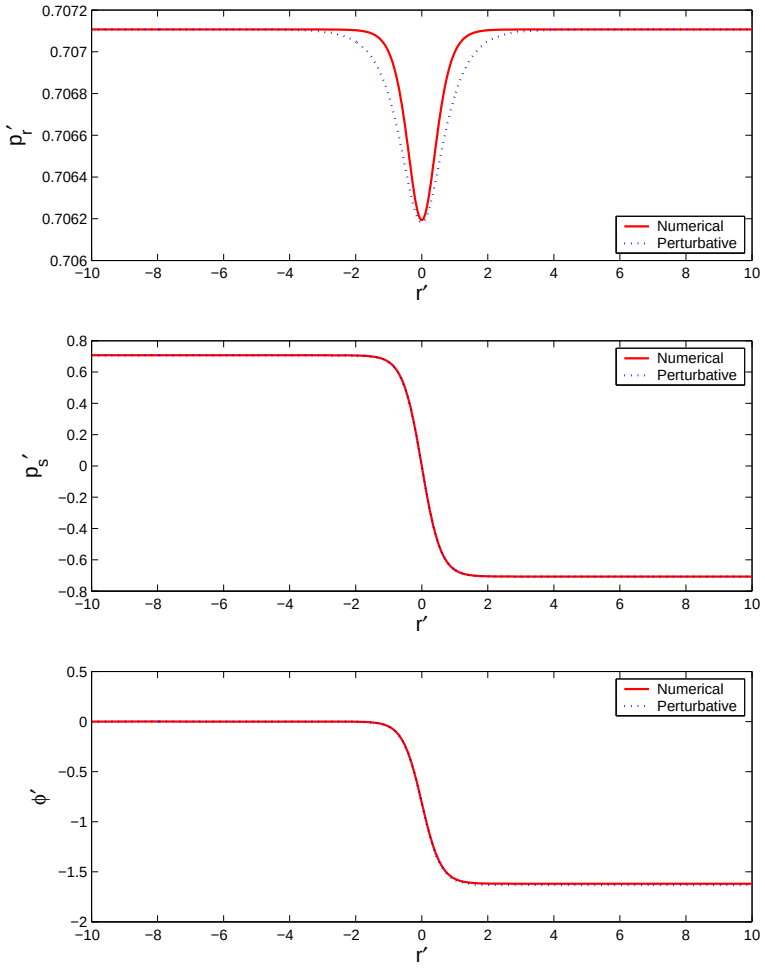

Figure 5.15: Structure of a 90° domain wall without defects.

Further, for $L \gg 0$, $B \sim O(1)$, Eq. (5.68) can be simplified as:

$$CL + D = 0. \tag{5.69}$$

For example, for $L = 10$, both Eq. (5.68) and Eq. (5.69) lead to the same solution:

$$p_m = 0.699438, \quad A = 0.70456, \quad B = 1.72581,$$
$$C = 0.0804732, \quad D = -0.804732.$$

Similarly, for the equations of $O(\epsilon')$, it is enough to just solve p'_{r1} from Eq. (5.59). Fig. 5.16 shows the numerical solution of the exact equations (Eq. (5.34)-(5.36)) and the perturbational solution ($p'_{r0} + \epsilon' p'_{r1}$, p'_{s0} and ϕ'_0). The results show that there is an uniform electric field that balances the potential drop.

We point out that the perturbative solution we obtain for small ϵ' is no different from the solution for $\epsilon' = 0$ except the small modification for p'_r in the transition layer, although ϵ' is a coefficient of highest order term. This is because the boundary conditions we choose for p'_r and p'_s does not allow the occurrence of boundary layers.

From our analysis and numerical simulation, we conclude that the potential drop across the 90° domain wall (Fig. 5.15) is the essential difference between the two types of domain walls. When a fixed potential is prescribed at the boundary, because of the potential drop, the whole potential profile is tilted (Fig. 5.15). An internal field is therefore formed inside the whole domain with a potential height and well near the wall. It is exactly because of this, 90° domain walls become potential sites for charge trapping and injection as we have showed in Section 5.1.2 and will further explore in following sections.

We also note that the thickness of 90^o domain wall is thinner than 180° domain walls if $b' + 3a' > 0$ (Eq. (5.62)). The sign of $b' + 3a'$ also decides whether it is a potential drop or a potential increase across the wall (Eq. (5.64)). The implication of the these facts and the choice of b' need further investigation.

5.3.3 Structure of Domain Walls with Defects and Diffusion

We now turn our attention to the structure of isolated domain walls with defects and diffusion. We found in Section 5.3.2 that the essential difference between 180° and 90° domain walls is a potential drop across the domain wall. In this section, we investigate

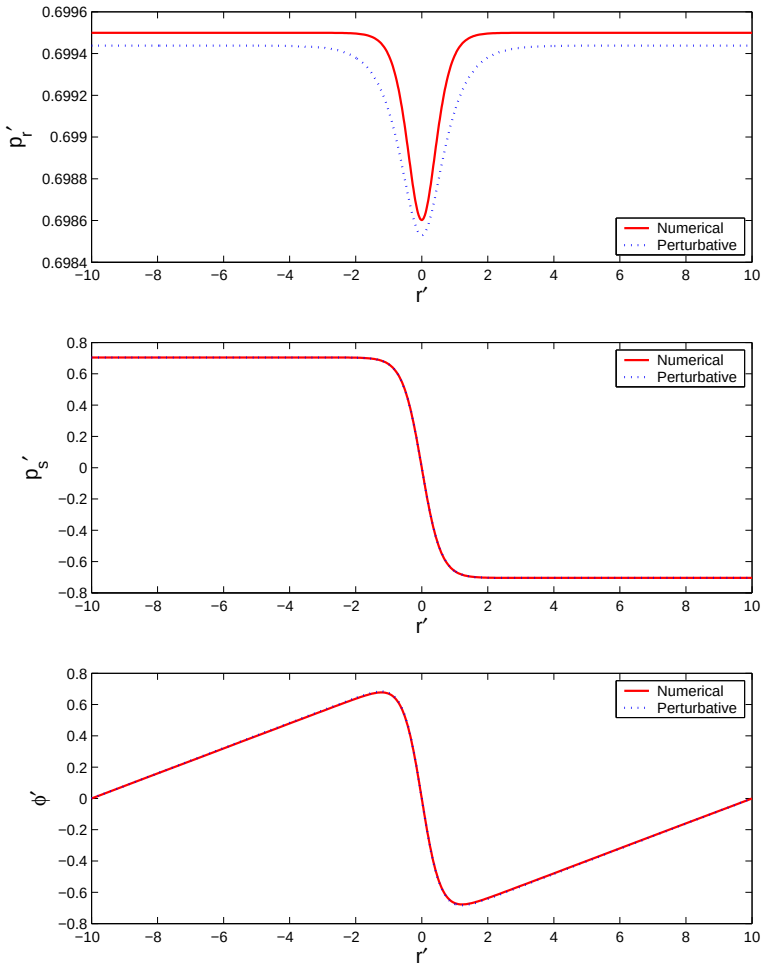

Figure 5.16: Structure of a 90° domain walls without defects with fixed potentials on both ends.

the consequence that this difference has on the space charges and vacancies. We focus on numerical analysis due to the complexity of the problem.

For 180° domain walls, we solve Eq. (5.31)–Eq. (5.33) subject to boundary conditions (5.39)–(5.41). However, instead of infinite domain, we now work on finite domain $[-L, L]$ with $L \gg 1$, i.e, $\pm\infty$ in Eq. (5.39)–Eq. (5.41) are replaced by $\pm L$. The results are identical to the case with no defects or diffusion and hence are not shown. For 90° domain walls, we solve Eq. (5.34)–Eq. (5.36) subject to boundary conditions (5.48)–(5.50) with $\pm\infty$ being replaced by $\pm L$. In addition, for mobile defects, we also need to solve Eq. (4.42) and Eq. (4.43) simultaneously.

5.3.3.1 Interaction of Defects with Domain Walls

Fig. 5.17 and Fig. 5.18 show the isolated 90° domain wall under different circumstances. Fig. 5.17 is the computed results on the domain $[-50, 50]$ with $a_0 = 10^{-7}\,\mathrm{Vm^3C^{-1}}$. Fig. 5.18 is the computed results with $a_0 = 10^{-9}\,\mathrm{Vm^3C^{-1}}$. Since the physical domain is scaled by $L_0 = p_0\sqrt{a_0/E_b}$, we compute on $[-500, 500]$ in Fig. 5.18 for comparison reason.

Let us first consider the of potential profile. The green dashed and cyan dotted lines show the potential drop in a perfect crystal cross the 90° domain wall as we have discussed in Section 5.3.2.2. When there are defects (oxygen vacancies in our case) present but immobile, the results are shown in blue dash-dot lines. We may interpret it as follows. The potential drop described above sweeps the electrons freed from ionized defects to one side of the domain wall which has higher potential and thus lower energy. The big potential drop is then lowered. In the mean time, a potential height and a well are formed cross the domain wall. When the defects are mobile, the results are shown in red solid lines. The positively charged defects flow into the potential well discussed above and redistribute near the domain wall. The defect concentration profile shown in these figures are normalized according to the initial uniformly distributed concentration. We can see the big difference between mobile defects and immobile defects. However, we also notice that the redistribution of defects only slightly change the polarization, potential and charge profile. Part of the reason may be that we use $\gamma = 4\phi_0$ instead of $\gamma = 40\phi_0$ in our computation (See Section 4.2 for details).

5.3.3.2 Parallel Arrays of Domain Walls

Fig. 5.19, 5.20, 5.21, 5.21 are computed results of Eq. (5.34), (5.35), (5.36) with periodic boundary conditions, with different a_0, defect concentration and periodicity. The existence of these almost periodic solutions and the redistribution of oxygen vacancies near 90^o domain walls gives a concrete mechanism for the domain memory observed by Ren (2004) and provides a potentially new mechanism for large electrostriction.

5.3.3.3 Effect of a_0 and Doping Level

We compare 90^o domain wall structures with different a_0 when defects and diffusion are considered in Fig. 5.23. We see no essential differences between $a_0 = 10^{-7}\,\mathrm{Vm^3C^{-1}}$ and $a_0 = 10^{-9}\,\mathrm{Vm^3C^{-1}}$, except the size of the potential differences cross the walls, the amount of charges accumulated near the walls, and the degree of the defect redistributions. All these quantitative differences comes from the fact that a bigger a_0, or a thicker domain wall in a perfect crystal has a bigger potential drop. We recall that potential is scaled by $\phi_0 = \sqrt{a_0 E_b}$ in Eq. (5.25), therefore, a bigger a_0 means a bigger potential drop. This is clearly shown by comparing Fig. 5.17 and Fig. 5.18.

We compare 90^o domain wall structures with different doping level in Fig. 5.24. Again, we do not see any qualitative differences between different N_ds.

5.3.3.4 A Final Remark

Finally, we point out that although we are working on isolated domain walls in Section 5.3, we still assume that far away from the wall, the crystal is connected to electrodes made of Platinum. Therefore, the Fermi level in our calculation is the Fermi level of Platinum. However, the results we obtain in this section also apply to isolated crystals. In that case, we simply replace the Fermi level of Platinum by the Fermi level of the crystal itself in Eq. (4.26), and the result is just a simple shift of potential. This is numerically shown in Fig. 5.25.

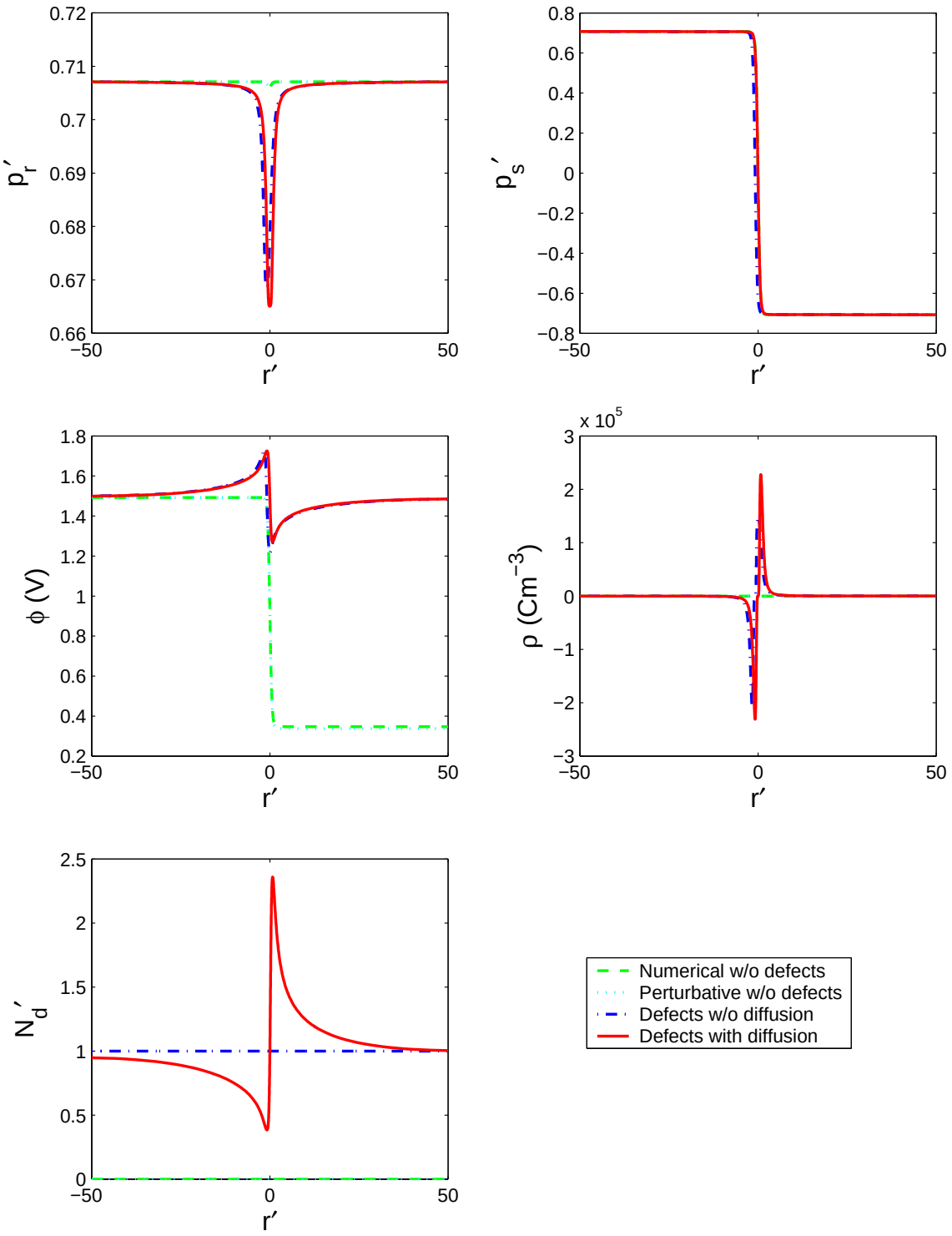

Figure 5.17: Isolated 90° domain walls with $a_0 = 10^{-7}\,\mathrm{Vm^3C^{-1}}$ under different circumstances. Green dashed lines: numerical results without defects; cyan dotted lines: perturbative results without defects; blue dash-dot lines: numerical results with defects but no diffusion; red solid lines: numerical results with defects and diffusion.

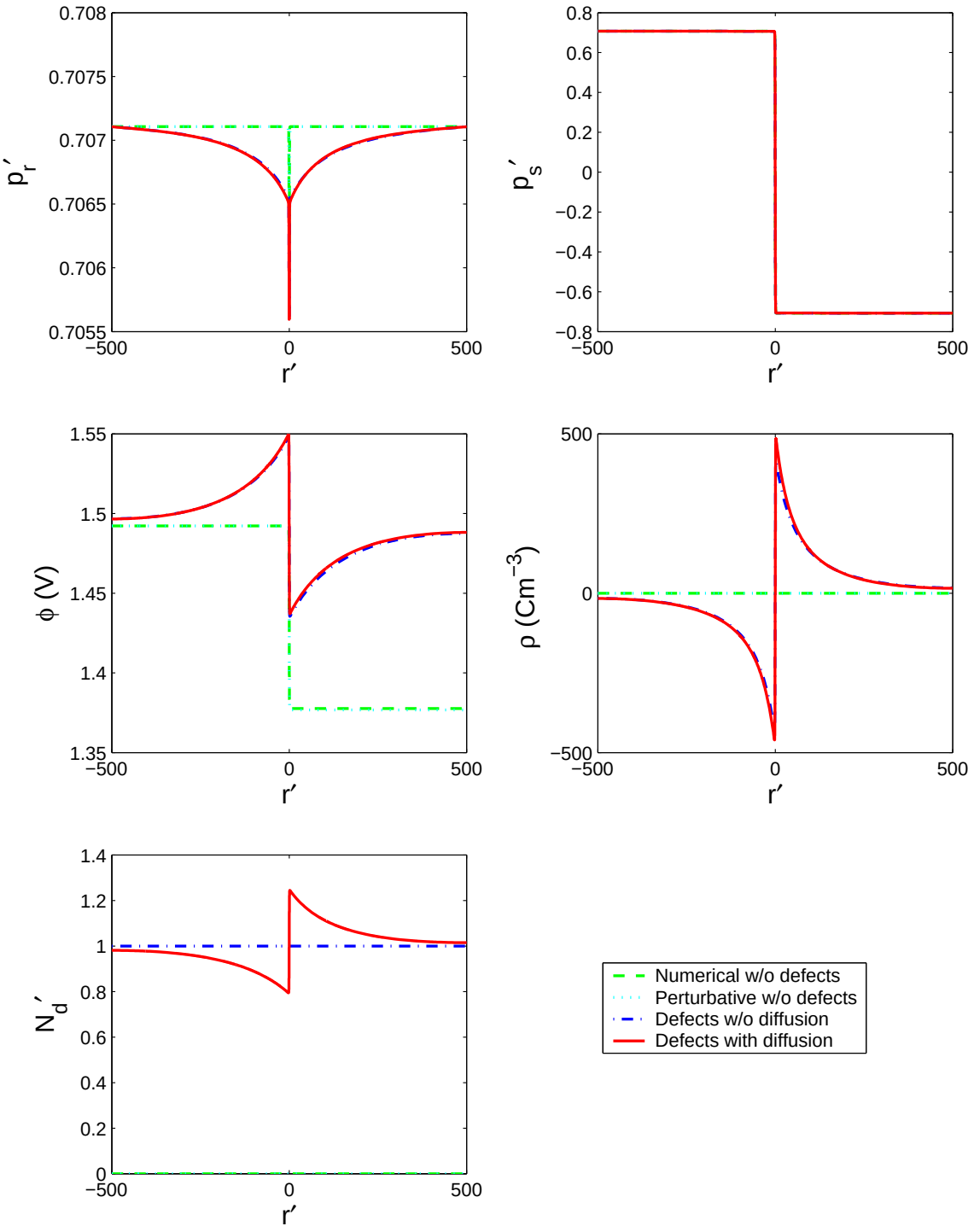

Figure 5.18: Isolated 90° domain walls with $a_0 = 10^{-9}\,\mathrm{Vm^3C^{-1}}$ under different circumstances. Green dashed lines: numerical results without defects; cyan dotted lines: perturbative results without defects; blue dash-dot lines: numerical results with defects but no diffusion; red solid lines: numerical results with defects and diffusion.

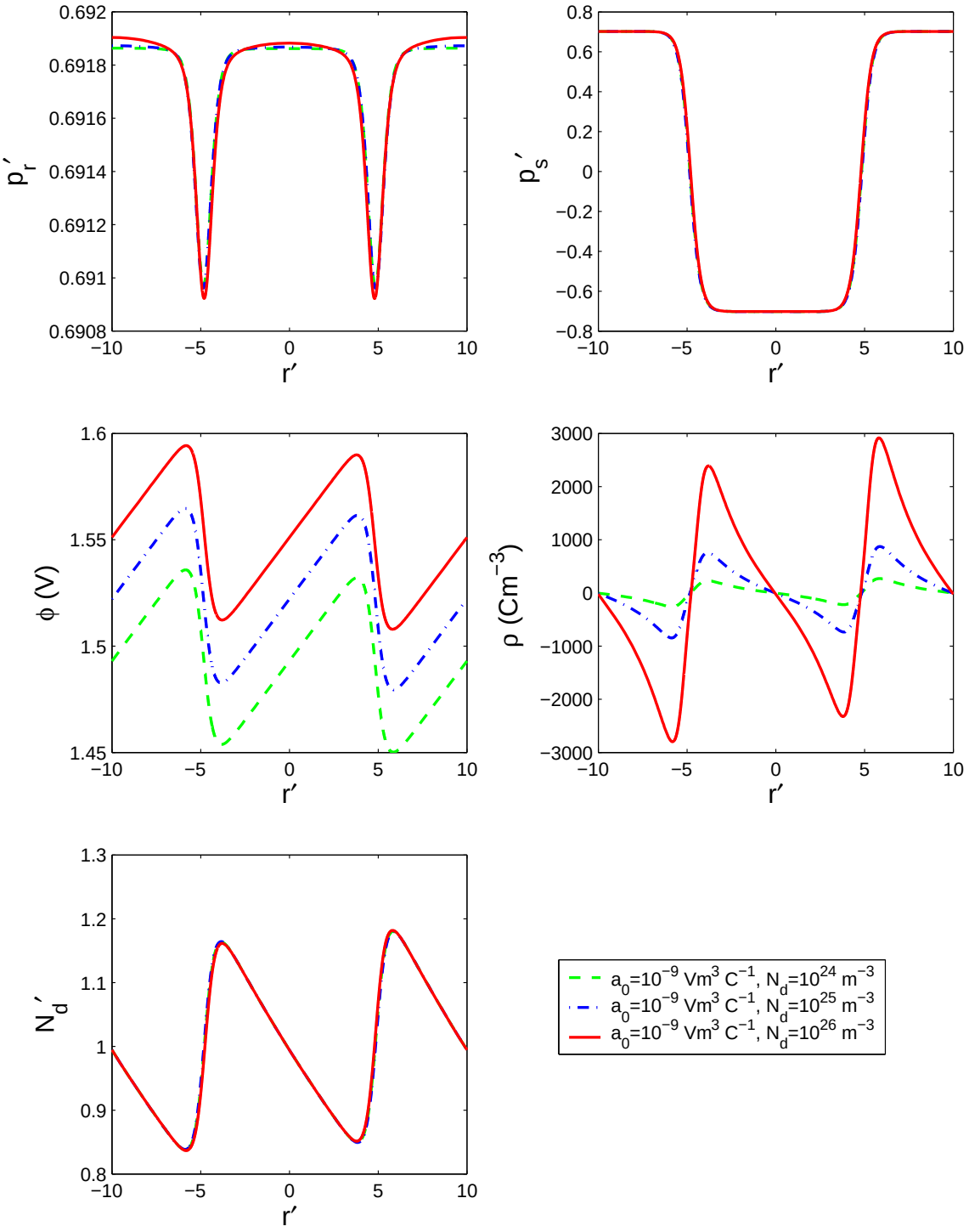

Figure 5.19: Periodic solution of 90° domain walls in 1-D with defects and diffusion, and with the same physical periodicity and different N_ds.

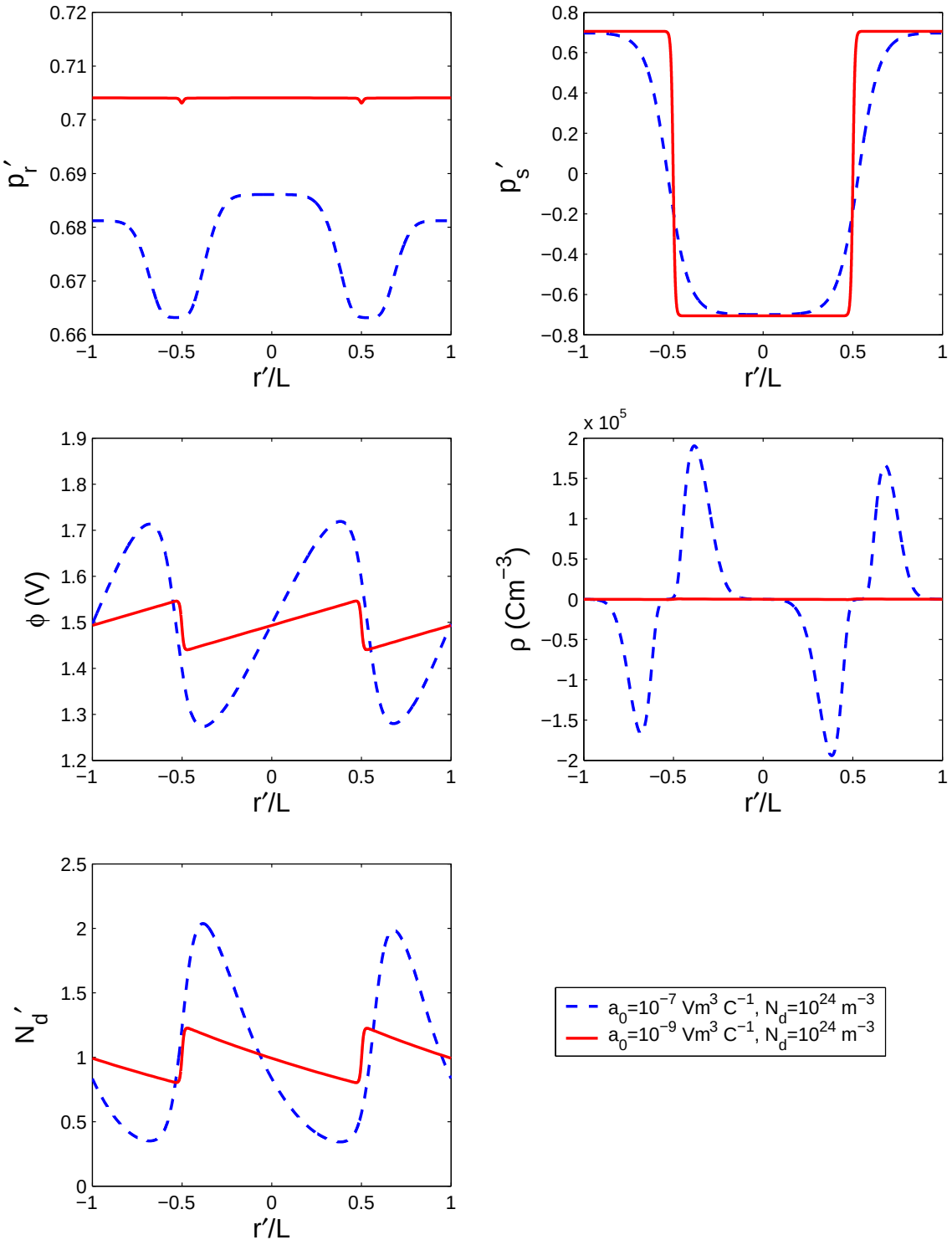

Figure 5.20: Periodic solution of 90° domain walls in 1-D with defects and diffusion, and with the same physical periodicity: L=5 for blue dashed lines and L=50 for red solid lines.

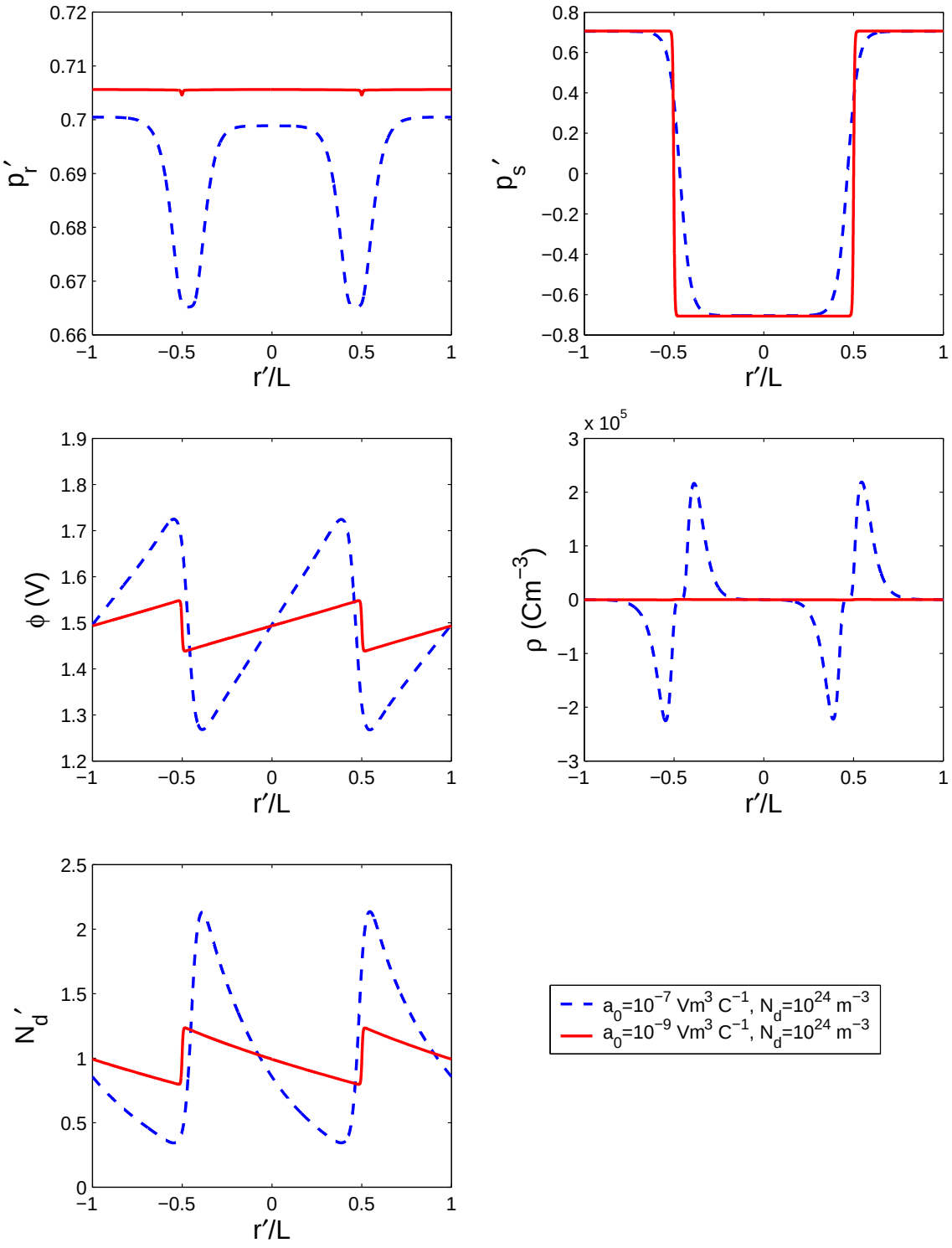

Figure 5.21: Periodic solution of 90° domain walls in 1-D with defects and diffusion, and with the same physical periodicity: L=10 for blue dashed lines and L=100 for red solid lines.

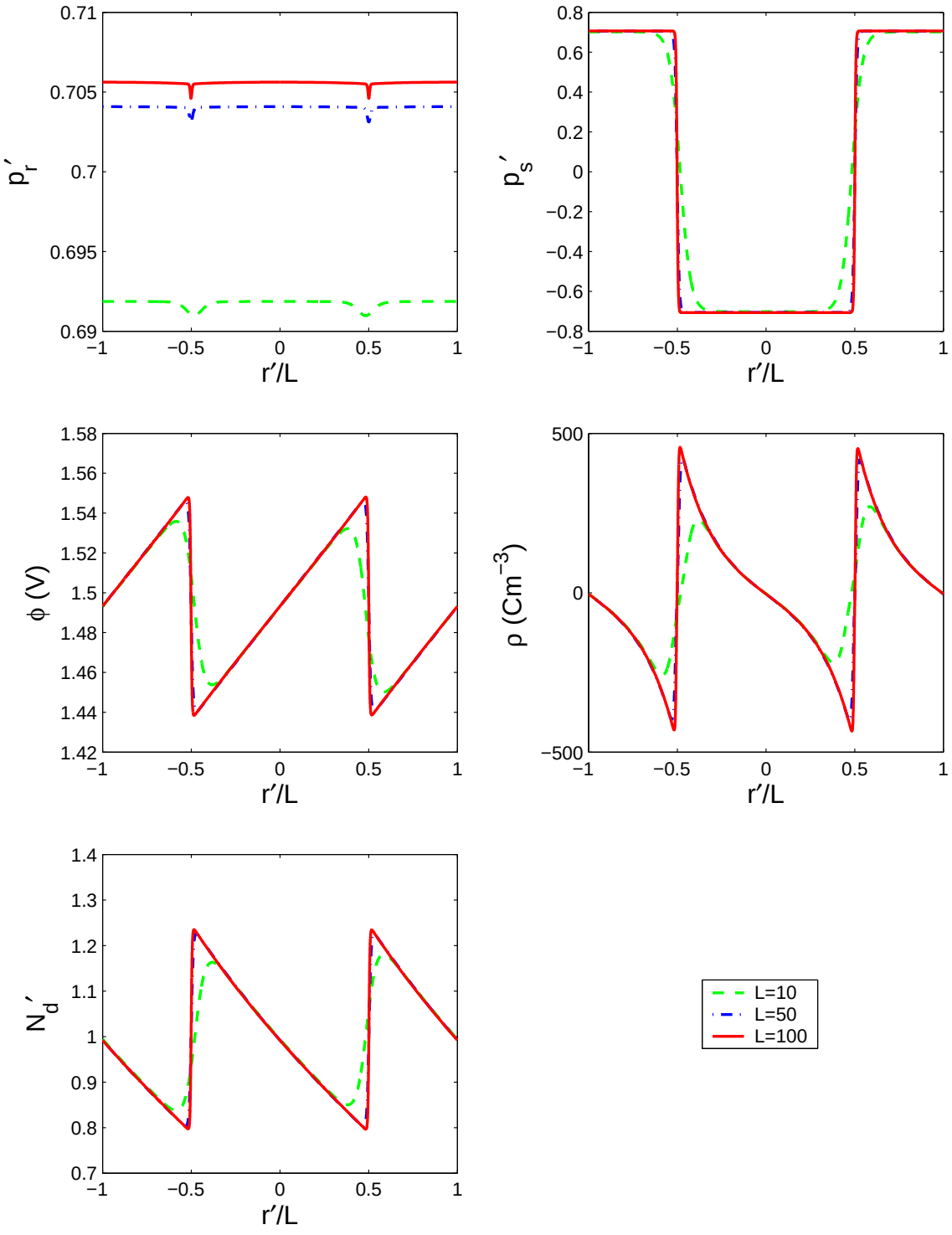

Figure 5.22: Periodic solution of 90° domain walls in 1-D with defects and diffusion, and with different physical periodicities ($N_d = 10^{24}\,\mathrm{m}^{-3}$, $a_0 = 10^{-9}\,\mathrm{Vm}^3$).

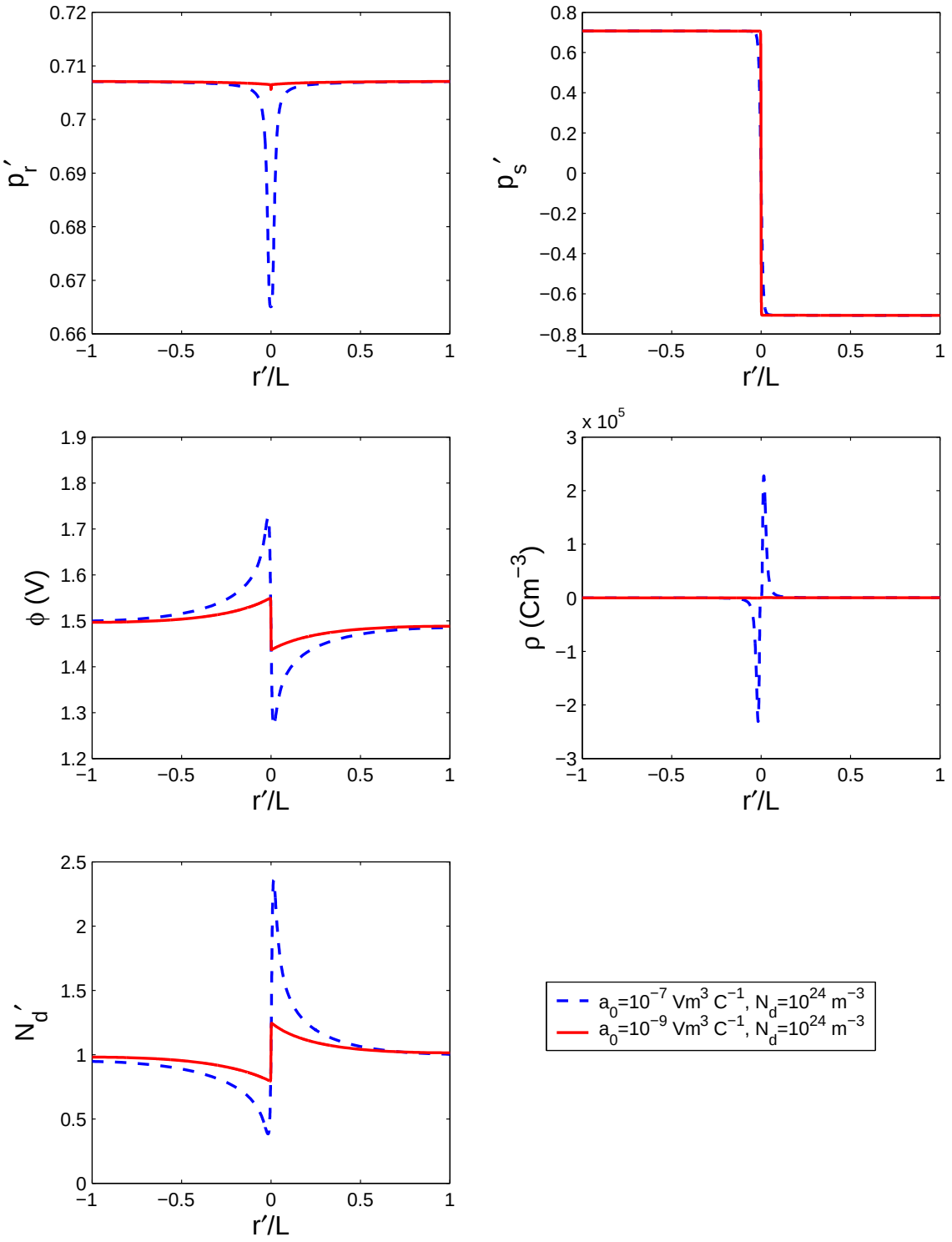

Figure 5.23: Isolated 90° domain walls with defects and diffusion with different a_0. Blue dashed lines: $a_0 = 10^{-7}\,\mathrm{Vm^3C^{-1}}$; red solid lines: $a_0 = 10^{-9}\,\mathrm{Vm^3C^{-1}}$.

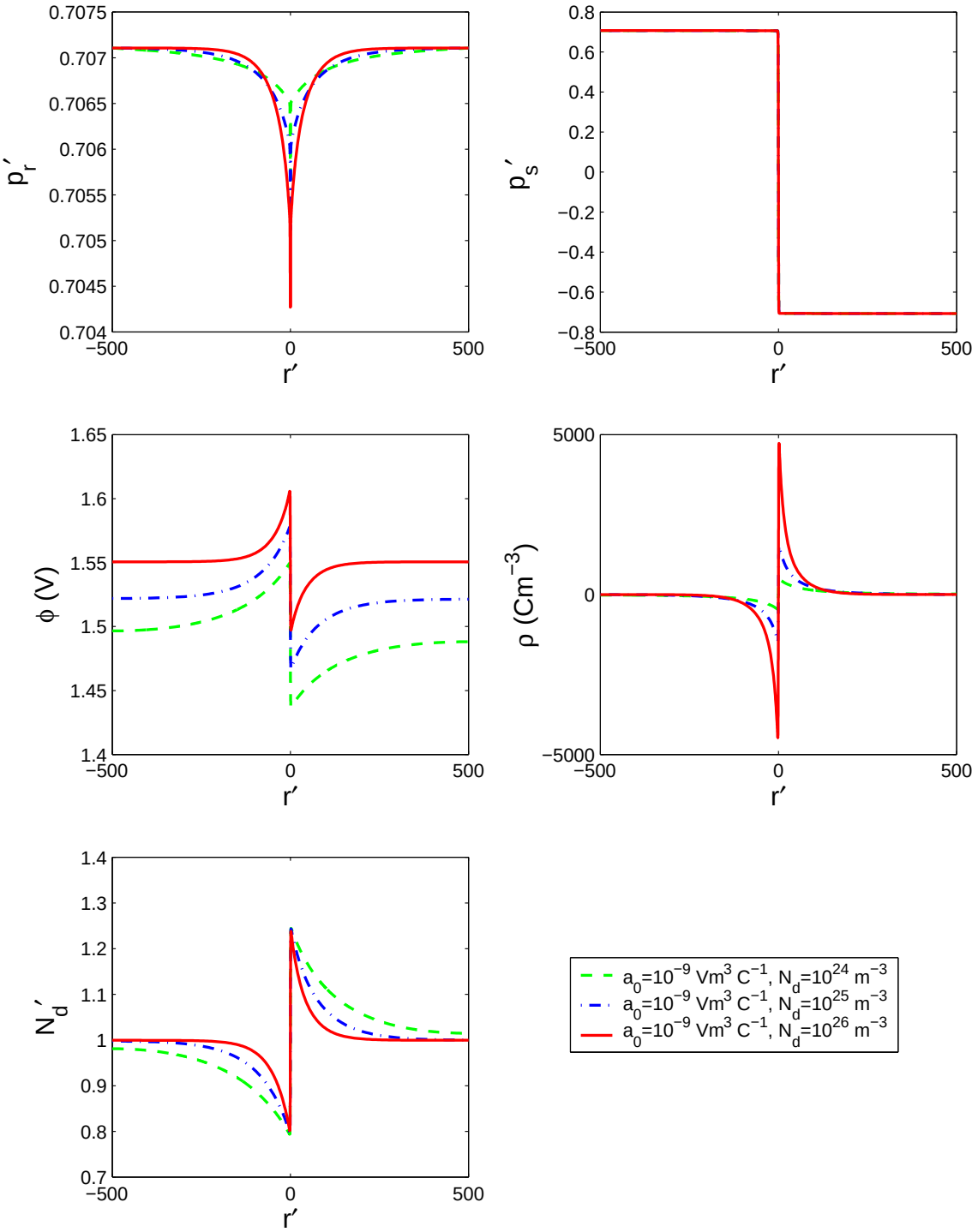

Figure 5.24: Isolated 90° domain walls with defects and diffusion with $a_0 = 10^{-9}\,\mathrm{Vm^3C^{-1}}$ and with different N_d. Green dashed lines: $N_d = 10^{24}\,\mathrm{m^{-3}}$; blue dash-dot lines: $N_d = 10^{25}\,\mathrm{m^{-3}}$; red solid lines: $N_d = 10^{26}\,\mathrm{m^{-3}}$.

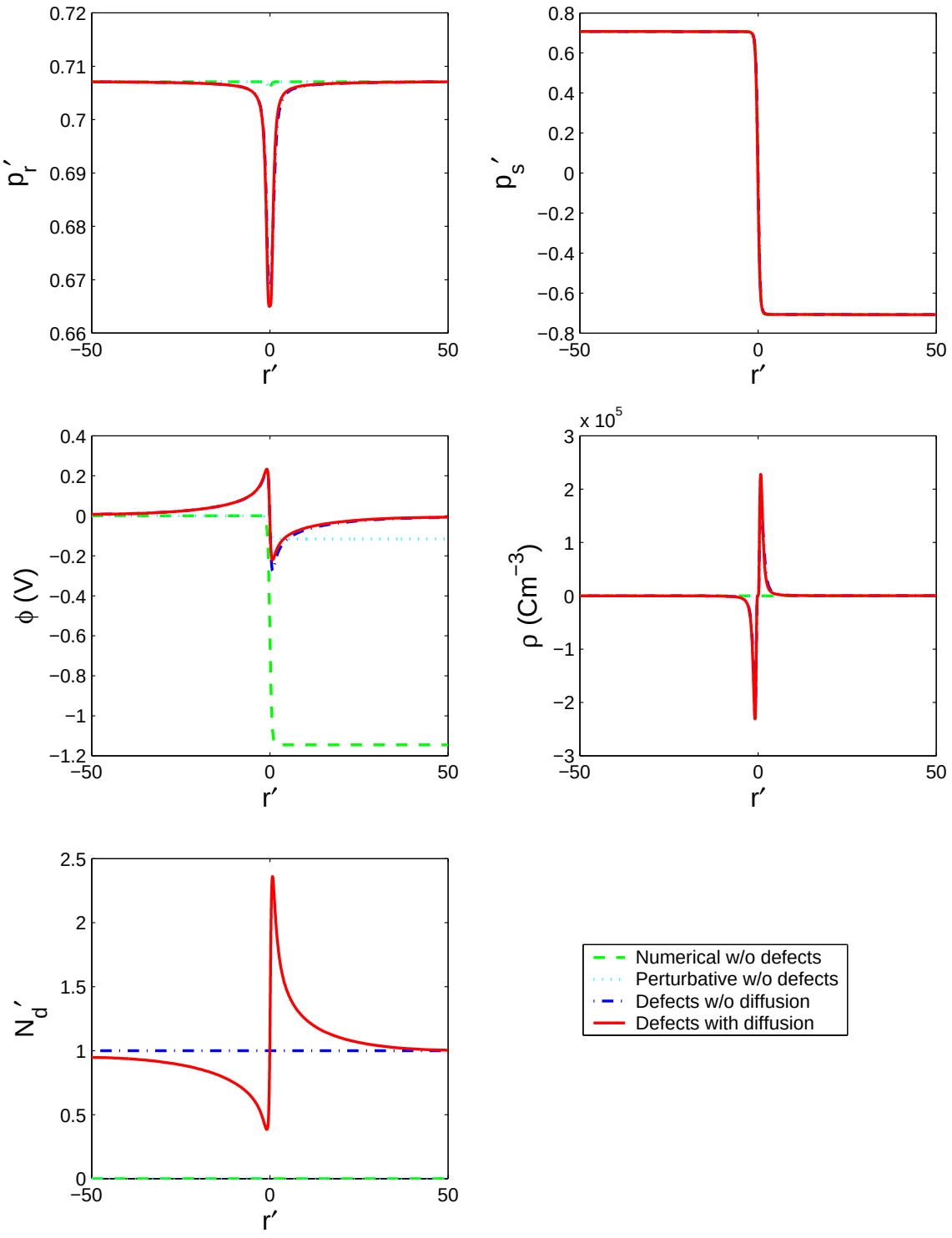

Figure 5.25: Isolated 90° domain walls in isolated crystals with $a_0 = 10^{-7}\,\mathrm{Vm^3C^{-1}}$ under different circumstances. Green dashed lines: numerical results without defects; cyan dotted lines: perturbative results without defects; blue dash-dot lines: numerical results with defects but no diffusion; red solid lines: numerical results with defects and diffusion.

Chapter 6

Field Energy Revisited

A ferroelectric crystal is spontaneously polarized below its Curie temperature, i.e., there is a non-vanishing dipole moment in each of its primitive cells. This non-vanishing moment is caused by a distortion of the primitive cell from the unpolarized configuration above the Curie temperature. For example, the polarization in $BaTiO_3$, as we illustrated schematically in Chapter 2, is the result of a shift of the positively charged ions relative to the negatively charged ones. Therefore, a ferroelectric crystal can be treated as a periodic distribution of charges such that it has zero net charge but non-zero polarization (dipole moment) in each primitive cell. In this chapter, we seek to derive a continuum theory starting from this atomistic (discrete) picture.

Recall that in Chapter 3, we wrote the energy of a ferroelectric as the sum of a local and nonlocal term:

$$\int_{\Omega_0} W_0 \, d\mathbf{x} + \frac{\epsilon_0}{2} \int_{\mathbb{R}^3} |\nabla \phi|^2 \, d\mathbf{x} \tag{6.1}$$

where W_0 depends on the pointwise polarization density and ϕ is obtained from the polarization density $\mathbf{p}$ via the Maxwell's equation*

$$\nabla(-\epsilon_0 \nabla \phi + \mathbf{p}) = 0 \, .$$

Alternately, we can write the electric field

$$\mathbf{E}(\mathbf{x}) = -\nabla \phi(\mathbf{x}) = \int_{\Omega_0} \mathbb{K}(\mathbf{x} - \mathbf{y}) \mathbf{p}(\mathbf{y}) \, d\mathbf{y} \tag{6.2}$$

*The field energy in Chapter 3 also included the energy generated by external sources. However, in this Chapter, it is sufficient to restrict ourselves to the field energy generated by the spontaneous polarization only.

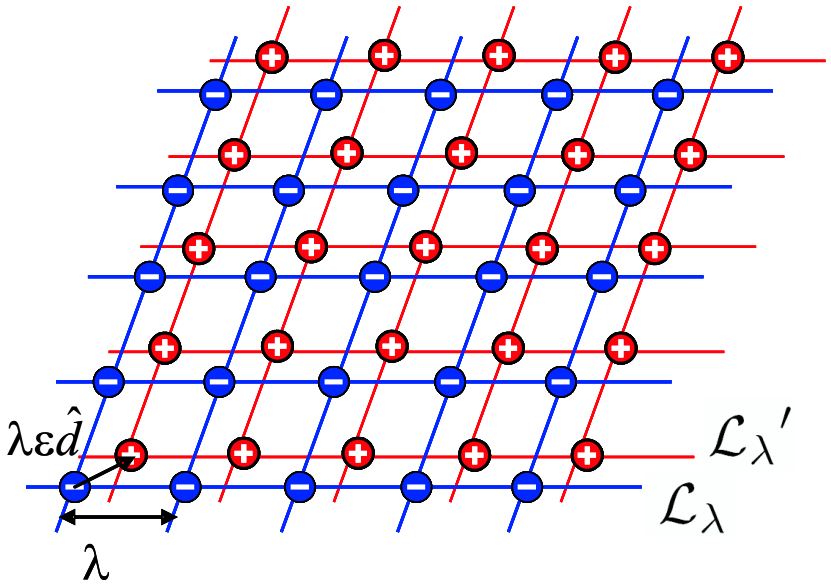

Figure 6.1: A periodic arrangement of charges which has zero net charge but non-zero polarization in each primitive cell inside Ω.

where

$$\mathbb{K}(\mathbf{x}) = \frac{1}{\epsilon_0 |\mathbf{x}|^3} \left\{ \mathbf{I} - 3 \frac{\mathbf{x}}{|\mathbf{x}|} \otimes \frac{\mathbf{x}}{|\mathbf{x}|} \right\}, \quad \mathbf{x} \in \mathbb{R}^3. \tag{6.3}$$

In this chapter, we examine if this can be justified starting from the discrete situation.

This question poses various difficulties. On the discrete or atomistic side, the calculation of Coulomb energy by lattice summation is not straightforward. This is because Coulomb energy has a decay rate of $1/r$ which falls off very slowly. Or mathematically speaking, the Coulomb interaction gives a series like $\sum_{n=1}^{\infty}(-1)^n/r$ which is only conditionally convergent. So it can be summed to any value, depending on the order of the summation. Similarly, on a continuum level, there are also tricky issues when dealing with the field inside a polarized material, since the dipole induced a non-integrable $1/r^3$ singularity in the field (See Eq. (6.3)). Indeed, this is the mathematical origin of the so-called *Lorentz local field*, a crucial concept in developing electromagnetic theory for continua.

The milestone work in addressing these difficulties is due to Lorentz (1952). When developing a theory for dielectrics, he calculated the electrostatic field of an array of point dipoles arranged on a uniform space lattice and concluded that[†]

$$\mathbf{E}_S = \mathbf{E}_L + \mathbf{E}_{MS} \tag{6.4}$$

[†]We follow the notation of Toupin (1956) here.

where $\mathbf{E}_S$ is the total electric field at a point inside the dielectrics, $\mathbf{E}_{MS}$ the Maxwell self field, or the macroscopic electric field generated by the dielectric body, and $\mathbf{E}_L$ the Lorentz local field which depends on lattice symmetry. For example, $\mathbf{E}_L = \mathbf{p}/3\epsilon_0$ for a cubic lattice where $\mathbf{p}$ is polarization per unit volume. In a fundamental work concerning continuum theory of elastic dielectrics, Toupin (1956) reinterpreted Lorentz's result and extended it to deformable dielectrics. He also argued that the Lorentz local field which depends on the lattice symmetry, and thus on the deformation, provides a contribution to W_0, the local energy density, along with contributions from other short range interactions. Brown (1966) developed similar theories for ferromagnetism. James and Müller (1994) rigorously calculated the Coulomb energy and the dipole field of a finite ferromagnetic body following Lorentz (1952). They also considered cases in which there is no oscillation of polarization, oscillation on the scale much larger than the lattice parameter, and oscillation on a scale comparable to the lattice parameter. Schlömerkemper (2002) studied magnetic forces in three-dimensional lattice and continuum settings. But, all of these authors start from a lattice of dipoles and none of them address a periodic arrangement of charges. Other important work includes Tiersten (1990) and Bobbio (2000), in which they developed electromagnetic equations for continua starting from the Maxwell's equations in free space; nevertheless, their approach is quite formal.

Starting from a periodic arrangement of charges poses a new and difficult set of problems. In fact, it is difficult to even define the polarization or dipole moment per primitive cell since it depends on the choice of the cell. For example, for a charge distribution $q(x) = q_0 \sin(x)$, the polarization $\int_\alpha^{\alpha+2\pi} q(x)x\,dx = -2\pi q_0 \cos\alpha$ depends on α! Or for example, we could get different values for the dipole if we make different choices of primitive cell in Fig. 6.1. King-Smith and Vanderbilt (1994) argued that while the polarization itself may be an ill-defined quantity, the change in polarization from a non-polar reference state is well defined and this is the experimentally relevant quantity. In the context of Fig. 6.1, if we choose the state $\epsilon = 0$ (where the two sub-lattices coincide) as the reference, then the dipole per unit cell is well defined to be $\mathbf{d} = q\lambda\epsilon\hat{\mathbf{d}}$. Some researchers (Resta, 1994) have also argued that this classical picture of primitive charges is insufficient and polarization should be regarded as a fundamental quantum mechanical quantity (a gauge-invariant phase feature of the electronic wave function). There are also issues of surface closure and charges. Many of these issues remain open for the future.

In this chapter, we rigorously justify the continuum theory of Chapter 3 with the classical interpretation of the ferroelectric as a distribution of charges as shown in Fig. 6.1 and with a definite choice of polarization per unit cell. The main result is Theorem 6 given in Section 6.4.1. It states that in the limit where the size of the body is large compared to the unit cell, the energy of Coulombic interactions is given by Eq. (6.1). It consists of a local part and a nonlocal part. The local part depends on the lattice structure, but is different from the Lorentz formula[‡]. The nonlocal part is as described before and identical to the Lorentz formula. At short distances, one sees the pair of charges, but at large distance, one only sees the dipoles.

6.1 Formulation of Problem

Consider a finite spontaneously polarized body. As we have just discussed, microscopically, we can view it as a group of positive charges residing on a Bravais lattice $\mathcal{L}_\lambda$, and the same group of charges with negative values defined on the $\mathcal{L}'_\lambda$ which is $\mathcal{L}$ with a shift $\epsilon\lambda\hat{\mathbf{d}}$, i.e., the positive charges are located on $\mathcal{L}_\lambda \cap \Omega$, while the negative charges are located on $(\mathcal{L}_\lambda + \epsilon\lambda\hat{\mathbf{d}}) \cap \Omega$.

A *Bravais lattice* $\mathcal{L}(\mathbf{e}_i, \mathbf{o})$ in $\mathbb{R}^3$ is an infinite set of points generated by translations of a single point $\mathbf{o}$ through three linear independent lattice vectors $\mathbf{e}_1, \mathbf{e}_2, \mathbf{e}_3$:

$$\mathcal{L}(\mathbf{e}_i, \mathbf{o}) = \left\{\mathbf{x} \in \mathbb{R}^3 : \mathbf{x} = \nu^i \mathbf{e}_i + \mathbf{o} \quad \text{where} \quad \nu^i \in \mathbb{Z},\ i = 1, 2, 3\right\}. \tag{6.5}$$

We assume (by normalization) that the unit cell defined by $\{\mathbf{e}_i\}$,

$$U := \left\{\mathbf{z} \in \mathbb{R}^3 : \mathbf{z} = \mathbf{x} + \alpha^i \mathbf{e}_i,\ \mathbf{x} \in \mathcal{L}(\mathbf{e}_i, o),\ 0 \le \alpha_i \le 1,\ i = 1, 2, 3\right\} \tag{6.6}$$

has unit volume, i.e., $[\mathbf{e}_1, \mathbf{e}_2, \mathbf{e}_3] = \mathbf{e}_1 \cdot (\mathbf{e}_2 \otimes \mathbf{e}_3) = 1$. A family of Bravais lattices $\mathcal{L}_\lambda, \lambda \in (0, 1]$ is defined as

$$\mathcal{L}_\lambda = \lambda \mathcal{L}_1 := \mathcal{L}(\lambda \mathbf{e}_i, \mathbf{o}). \tag{6.7}$$

Clearly, each unit cell for $\mathcal{L}_\lambda$ has volume λ^3. We define another family of Bravais lattices $\mathcal{L}'_\lambda, \lambda \in (0, 1]$ by shifting $\mathcal{L}_\lambda$ a small distance of $\lambda\epsilon$ along $\hat{\mathbf{d}}$ direction, that is, $\mathcal{L}'_\lambda = \mathcal{L}_\lambda + \lambda\epsilon\hat{\mathbf{d}}$.

[‡]However, since it is absorbed into W_0, we do not see the explicit manifestation of this difference.

We place a negative charge $q_\lambda(\mathbf{x})$ at each point $\mathbf{x} \in \mathcal{L}_\lambda$. At the corresponding point $\mathbf{x} + \lambda\epsilon\hat{\mathbf{d}} \in \mathcal{L}'_\lambda$, we place a positive charge $q_\lambda(\mathbf{x} + \lambda\epsilon\hat{\mathbf{d}})$, and $q_\lambda(\mathbf{x} + \lambda\epsilon\hat{\mathbf{d}}) = -q(\mathbf{x})$ in order to maintain neutral charge in each unit cell (Fig. 6.1). In another word, we place at each point of $\mathcal{L}_\lambda$ an electric dipole with magnitude

$$d_\lambda = q_\lambda \lambda\epsilon \tag{6.8}$$

along $\hat{\mathbf{d}}$ direction. Note that we allow the charge q_λ to vary from one lattice point to another but not the direction $\hat{\mathbf{d}}$.

We want to calculate the limiting energy of these electric dipoles when $\lambda \to 0$ with ϵ held constant, and

$$d_\lambda(\mathbf{x}) \to p \in L^2(\mathbb{R}^3, \mathbb{R}) \quad \text{as} \quad \lambda \to 0. \tag{6.9}$$

By Eq. (6.9) we mean $d_\lambda^\sim \in L^2(\mathbb{R}^3, \mathbb{R})$ defined by

$$d_\lambda^\sim(\mathbf{z}) = \lambda^{-3} d_\lambda(\mathbf{x}) \quad \text{for} \quad \mathbf{z} \in \mathbf{x} + \lambda U \quad \text{and} \quad \mathbf{x} \in \mathcal{L}_\lambda. \tag{6.10}$$

converges to $p \in L^2(\mathbb{R}^3, \mathbb{R})$, i.e.,

$$d_\lambda^\sim \to p \quad \text{in} \quad L^2(\mathbb{R}^3, \mathbb{R}). \tag{6.11}$$

This is equivalent to (See Lemma 8)

$$p_\lambda \to p \quad \text{in} \quad L^2(\mathbb{R}^3, \mathbb{R}) \tag{6.12}$$

where $p_\lambda \in L^2(\mathbb{R}^3, \mathbb{R})$ is any background field such that

$$d_\lambda(\mathbf{x}) = \int_{\mathbf{x}+\lambda U} p_\lambda(\mathbf{z})\, d\mathbf{z}. \tag{6.13}$$

6.2 Energy of Array of Dipoles

The electric potential at $\mathbf{x}$ with $-q$ at origin, and q at $\lambda\epsilon\hat{\mathbf{d}}$ (Fig. 6.2) is

$$\phi(\mathbf{x}) = q\left(\frac{1}{|\mathbf{x} - \lambda\epsilon\hat{\mathbf{d}}|} - \frac{1}{|\mathbf{x}|}\right). \tag{6.14}$$

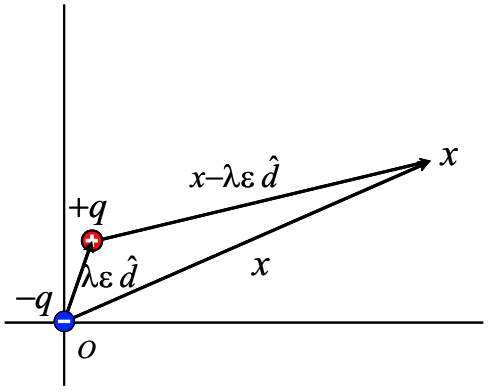

Figure 6.2: Electric field of an electric dipole.

Then the energy of the array shown in Fig. 6.1 is:

$$\begin{aligned}
\mathcal{E}_\lambda &= -\frac{1}{2}\sum_{\substack{\mathbf{x},\mathbf{y}\in\mathcal{L}_\lambda\\ \mathbf{y}\neq\mathbf{x}}} q_\lambda(\mathbf{x})\left(\frac{1}{|\mathbf{x}-\mathbf{y}-\lambda\epsilon\hat{\mathbf{d}}|}-\frac{1}{|\mathbf{x}-\mathbf{y}|}\right)q_\lambda(\mathbf{y})\\
&\quad+\frac{1}{2}\sum_{\substack{\mathbf{x},\mathbf{y}\in\mathcal{L}_\lambda\\ \mathbf{y}\neq\mathbf{x}}} q_\lambda(\mathbf{x})\left(\frac{1}{|\mathbf{x}-\mathbf{y}|}-\frac{1}{|\mathbf{x}-\mathbf{y}+\lambda\epsilon\hat{\mathbf{d}}|}\right)q_\lambda(\mathbf{y})\\
&\quad-\sum_{\mathbf{x}\in\mathcal{L}_\lambda}\frac{q_\lambda^2(\mathbf{x})}{\lambda\epsilon}\\
&= -\frac{1}{2}\sum_{\substack{\mathbf{x},\mathbf{y}\in\mathcal{L}_\lambda\\ \mathbf{y}\neq\mathbf{x}}} q_\lambda(\mathbf{x})\left(\frac{1}{|\mathbf{x}-\mathbf{y}-\lambda\epsilon\hat{\mathbf{d}}|}-\frac{2}{|\mathbf{x}-\mathbf{y}|}+\frac{1}{|\mathbf{x}-\mathbf{y}+\lambda\epsilon\hat{\mathbf{d}}|}\right)q_\lambda(\mathbf{y})\\
&\quad-\sum_{\mathbf{x}\in\mathcal{L}_\lambda}\frac{q_\lambda^2(\mathbf{x})}{\lambda\epsilon}
\end{aligned}\tag{6.15}$$

Our goal is to understand this energy. We first estimate the last term in Eq. (6.15). We assume $d_\lambda \to d$ as $\lambda \to 0$, by Lemma 8 and Eq. (6.8), we obtain

$$d_\lambda = \int_{\mathbf{x}+\lambda U} p_\lambda(\mathbf{z})\,d\mathbf{z}, \tag{6.16}$$

$$q_\lambda = \int_{\mathbf{x}+\lambda U} \rho_\lambda(\mathbf{z})\,d\mathbf{z} \tag{6.17}$$

with

$$p_\lambda(\mathbf{z}) = \lambda\epsilon\rho_\lambda(\mathbf{z}) \tag{6.18}$$

and

$$p_\lambda \to p \quad \text{in} \quad L^2(\mathbb{R}^3, \mathbb{R}). \tag{6.19}$$

The convergence of p_λ to p indicates that p_λ is bounded. For ϵ being constant, we obtain,

$$\rho_\lambda(\mathbf{z}) \sim \frac{O(1)}{\lambda}. \tag{6.20}$$

Therefore,

$$\begin{aligned}
&\sum_{\mathbf{x}\in\mathcal{L}_\lambda} \frac{q_\lambda^2(\mathbf{x})}{\lambda\epsilon} \\
&= \frac{1}{\lambda\epsilon} \sum_{\mathbf{x}\in\mathcal{L}_\lambda} \left(\int_{\mathbf{x}+\lambda U} \rho_\lambda(\mathbf{z})\, d\mathbf{z} \right)^2 \\
&\le \frac{1}{\lambda\epsilon} \sum_{\mathbf{x}\in\mathcal{L}_\lambda} \lambda^3 \int_{\mathbf{x}+\lambda U} \rho_\lambda^2(\mathbf{z})\, d\mathbf{z} \\
&= \frac{\lambda^2}{\epsilon} \int_{\mathbb{R}^3} \rho_\lambda^2(\mathbf{z})\, d\mathbf{z}.
\end{aligned} \tag{6.21}$$

Notice we use Jensen's inequality in the above derivation. In view of Eq. (6.20) and (6.21), we conclude that the energy of charge-charge interaction is finite if $d_\lambda \to p$ as $\lambda \to 0$ and ϵ being constant.

Therefore, from now on, we only consider:

$$\mathcal{E}_\lambda = -\frac{1}{2} \sum_{\substack{\mathbf{x},\mathbf{y}\in\mathcal{L}_\lambda \\ \mathbf{y}\neq\mathbf{x}}} q_\lambda(\mathbf{x}) \left(\frac{1}{\left|\mathbf{x}-\mathbf{y}-\lambda\epsilon\hat{\mathbf{d}}\right|} - \frac{2}{|\mathbf{x}-\mathbf{y}|} + \frac{1}{|\mathbf{x}-\mathbf{y}+\lambda\epsilon\hat{\mathbf{d}}|} \right) q_\lambda(\mathbf{y}) \tag{6.22}$$

Eq. (6.22) can be rewritten as

$$\mathcal{E}_\lambda = -\frac{1}{2} \sum_{\substack{\mathbf{x},\mathbf{y}\in\mathcal{L}_\lambda \\ \mathbf{y}\neq\mathbf{x}}} d_\lambda(\mathbf{x}) K_\lambda(\mathbf{x}-\mathbf{y}) d_\lambda(\mathbf{y}) \tag{6.23}$$

where

$$K_\lambda(\mathbf{x}-\mathbf{y}) = \frac{1}{(\lambda\epsilon)^2} \left(\frac{1}{|\mathbf{x}-\mathbf{y}+\lambda\epsilon\hat{\mathbf{d}}|} - \frac{2}{|\mathbf{x}-\mathbf{y}|} + \frac{1}{|\mathbf{x}-\mathbf{y}-\lambda\epsilon\hat{\mathbf{d}}|} \right). \tag{6.24}$$

Before we proceed to derive the energy in terms of macroscopic quantities, we first briefly review some mathematical concepts and a few kernels which will be used in the derivation.

6.3 Preliminaries

6.3.1 Field of Monopoles and Dipoles

The field of a unit charge (monopole) in a vacuum is [§]:

$$\mathbf{u} = \frac{\mathbf{x}}{|\mathbf{x}|^3}, \quad \mathbf{x} \in \mathbb{R}^3. \tag{6.25}$$

Except at the origin where it has a r^{-2} singularity, $\mathbf{u}$ is smooth and satisfies

$$\mathbf{u}(\mathbf{x}) = -\nabla\phi = -\nabla\left(\frac{1}{|\mathbf{x}|}\right) \tag{6.26}$$

where

$$\phi = \frac{1}{|\mathbf{x}|} \tag{6.27}$$

is the electric potential of a monopole.

The field of a unit dipole in a vacuum is

$$\mathbb{K}(\mathbf{x}) = \frac{1}{|\mathbf{x}|^3}\left\{\mathbf{I} - 3\frac{\mathbf{x}}{|\mathbf{x}|} \otimes \frac{\mathbf{x}}{|\mathbf{x}|}\right\}, \quad \mathbf{x} \in \mathbb{R}^3. \tag{6.28}$$

$\mathbb{K}$ has a r^{-3} singularity at the origin; else where it is smooth and satisfies

$$\mathbb{K}(\mathbf{x}) = -\nabla\mathbf{u} = \nabla\nabla\phi. \tag{6.29}$$

6.3.2 Dipole Field in the Sense of Distribution

Since the dipole field has a r^{-3} singularity, it is not a locally integrable function. An integral or a volume average of in a classical sense is meaningless. We therefore introduce the concept of distribution (See for example, Mitrović and Žubrinić, 1998, Ch. 4).

We denote $C_0^\infty(\mathbb{R}^n)$ as the space of all infinitely differentiable function with compact support on $\mathbb{R}^n$. A sequence of function (φ_m), $m \in \mathbb{N}$, converges to zero in $C_0^\infty(\mathbb{R}^n)$ if

1. $\varphi_m \in C_0^\infty(\mathbb{R}^n)$ for every $m \in \mathbb{N}$;

[§] $1/\epsilon_0$ should be added in the expression in order to be consistent with the unit we use in previous chapters. However, for simplicity and without causing much confusion, we omit it here and in the discussion that follows.

2. there exists a compact set $K \subset \mathbb{R}^n$ independent of m, such that $\text{supp}(\varphi_m) \subseteq K$ for all $m \in \mathbb{N}$;

3. for every multi-index $\alpha = (\alpha_1, \ldots, \alpha_n)$, the sequence of partial derivatives $(D^\alpha \varphi_m(x))$ converges uniformly to zero on K (and therefore on $\mathbb{R}^n$), that is

$$\max_{\mathbb{R}^n} |D^\alpha \varphi_m(x))| \to 0 \quad \text{as} \quad m \to \infty. \tag{6.30}$$

Also, we say that $\varphi_m \to \varphi$ in $C_0^\infty(\mathbb{R}^n)$ if $\varphi - \varphi_m \to 0$ in $C_0^\infty(\mathbb{R}^n)$ as $m \to \infty$.

We denote $D(\mathbb{R}^n)$ as the space $C_0^\infty(\mathbb{R}^n)$ equipped with such a topology of convergence. A *distribution* is any linear and continuous functional defined on $D(\mathbb{R}^n)$ with values in $\mathbb{R}$. The space of all distributions defined on $D(\mathbb{R}^n)$ is denoted by $D'(\mathbb{R}^n)$.

Briefly, the continuity of a distribution T means:

$$\varphi_m \to \varphi \quad \text{in} \quad D(\mathbb{R}^n) \quad \Rightarrow \quad < T, \varphi_m > \to < T, \varphi > \quad \text{in} \quad \mathbb{C} \quad \text{as} \quad m \to \infty. \tag{6.31}$$

And a sequence of distributions T_k converges to T in $D'(\mathbb{R}^n)$ if and only if

$$< T_k, \varphi > \to < T, \varphi > \quad \text{as} \quad k \to \infty, \quad \forall \quad \varphi \in D(\mathbb{R}^n). \tag{6.32}$$

Let $u : \mathbb{R}^n \to \mathbb{R}$ be a locally integrable function, then a functional $T_u : D(\mathbb{R}^n) \to \mathbb{C}$ defined by

$$< T_u, \varphi >= \int_{\mathbb{R}^n} u(\mathbf{x})\varphi(\mathbf{x})\, d\mathbf{x}, \quad \varphi \in D(\mathbb{R}^n), \tag{6.33}$$

is a distribution. Any distribution that is representable in form (6.33) is called *regular distribution*, otherwise it is called *singular distribution*.

As an example of singular distribution and also for later use, we introduce *Dirac's delta distribution* $\delta_{\mathbf{a}}$ here. Let $\mathbf{a} \in \mathbb{R}^n$, $\delta_{\mathbf{a}}$ is defined by

$$< \delta_{\mathbf{a}}, \varphi >= \varphi(\mathbf{a}) \tag{6.34}$$

for every $\varphi \in D(\mathbb{R}^n)$.

Given any distribution $T \in D'(\mathbb{R}^n)$ and multi-index $\alpha \in \mathbb{N}_0^n$ [¶], the derivative of order α

[¶] $\mathbb{N}_0 = \mathbb{N} \cup 0$ denotes the set of nonnegative integers.

of the distribution T is the distribution $D^\alpha T$ defined by

$$< D^\alpha T, \varphi >:= (-1)^{|\alpha|} < T, D^\alpha \varphi >, \quad \forall \quad \varphi \in D(\mathbb{R}^n). \tag{6.35}$$

The convolution of a distribution T with $\varphi \in D(\mathbb{R}^n)$ is the function $T * \varphi : \mathbb{R}^n \to \mathbb{R}$ defined by

$$(T * \varphi)(\mathbf{x}) =< T_{\mathbf{y}}, \varphi(\mathbf{x} - \mathbf{y}) > . \tag{6.36}$$

More clearly, if T is a regular distribution representable by a locally integrable function $u : \mathbb{R}^n \to \mathbb{R}$, then,

$$(T * \varphi)(\mathbf{x}) = \int_{\mathbb{R}^n} u(\mathbf{y})\varphi(\mathbf{x} - \mathbf{y})\, d\mathbf{y}. \tag{6.37}$$

We define

$$T(\varphi)(\mathbf{x}) =< T(\mathbf{x}, \mathbf{y}), \varphi(\mathbf{y}) >, \quad \varphi \in D(\mathbb{R}^n), \tag{6.38}$$

if T defined on $\mathbb{R}^m \times \mathbb{R}^n$ is a distribution on $D(\mathbb{R}^n)$ for each $\mathbf{x} \in \mathbb{R}^m$.

The domain of distribution T can also be extend from $D(\mathbb{R}^n)$ to L^2 [‖] if

$$\|T(\varphi)\|_{L^2} \le c \|\varphi\|_{L^2} \quad \forall \quad \varphi \in D(\mathbb{R}^n) \tag{6.39}$$

for some constant c [**]. This is because if $\varphi_k \in D$ is a Cauchy sequence in L^2, then

$$\|T(\varphi^k) - T(\varphi^j)\|_{L^2} \le c \|\varphi^k - \varphi^j\|_{L^2}, \tag{6.40}$$

which means $T(\varphi^k)$ is a Cauchy sequence in L^2. Thus, for any $\varphi \in L^2$, we define

$$T(\varphi) := \lim_{k \to \infty} T(\varphi^k) \tag{6.41}$$

where $\varphi^k \in D(\mathbb{R}^n)$ and $\varphi^k \to \varphi$ in L^2.

Now, let's return to our subject. Since the monopole field $\mathbf{u}$ is a locally integrable function, we can review it as a vector-valued distribution (a distribution in each component). Further, since $\mathbb{K} = -\nabla \mathbf{u}$ in $\mathbb{R}^3$ except at the origin, we can review $\mathbb{K}$ as a matrix-valued

[‖] Or any normed linear space in which $C_0^\infty(\mathbb{R}^n)$ is dense.

[**] The same argument also applies to convolution of a distribution.

distribution, which is a gradient of a distribution $-\mathbf{u}$, and

$$\mathbb{K}(\varphi) := \int_{\mathbb{R}^3} \mathbf{u} \otimes \nabla\varphi(\mathbf{x})\, d\mathbf{x}, \quad \varphi \in D(\mathbb{R}^3). \tag{6.42}$$

With this interpretation, $\mathbb{K}$ is well defined.

6.3.3 A Few Kernels

Define

$$\mathbb{P}^{(r)}_{MS}(\mathbf{x}) = \begin{cases} \mathbb{K}(\mathbf{x}) & |\mathbf{x}| > r, \\ \mathbf{0} & |\mathbf{x}| \le r. \end{cases} \tag{6.43}$$

Lemma 1.

$$\int_{\partial B(\varrho)} \mathbb{P}^{(r)}_{MS}(\mathbf{x})\, d\mathbf{a} = \mathbf{0}, \tag{6.44}$$

$$\int_{B(\varrho)} \mathbb{P}^{(r)}_{MS}(\mathbf{x})\, d\mathbf{x} = \mathbf{0}. \tag{6.45}$$

Proof. (i). When $\varrho \le r$, obviously, $\int_{\partial B(\varrho)} P^{(r)}_{MS}(\mathbf{x})\, d\mathbf{a} = \mathbf{0}$.

when $\varrho > r$,

$$\begin{aligned} \int_{\partial B(\varrho)} \mathbb{P}^{(r)}_{MS}(\mathbf{x})\, d\mathbf{a} &= -\frac{1}{\varrho^3}\left[4\pi\varrho^2\mathbf{I} - 3\int_{\partial B(\varrho)} \hat{\mathbf{n}} \otimes \hat{\mathbf{n}}\, d\mathbf{a}\right] \\ &= -\frac{1}{\varrho^3}\left[4\pi\varrho^2\mathbf{I} - 3\frac{4\pi\varrho^2}{3}\mathbf{I}\right] \\ &= \mathbf{0}. \end{aligned}$$

Notice that in the above derivation we use the fact that

$$\int_{\partial B(\varrho)} \hat{\mathbf{n}} \otimes \hat{\mathbf{n}}\, d\mathbf{a} = \frac{4\pi\varrho^2}{3}\mathbf{I}. \tag{6.46}$$

(ii). When $\varrho \le r$, obviously, $\int_{B(\varrho)} P^{(r)}_{MS}(\mathbf{x})\, d\mathbf{x} = \mathbf{0}$.

When $\varrho > r$,

$$\begin{aligned}\int_{B(\varrho)} \mathbb{P}_{MS}^{(r)}(\mathbf{x})\, d\mathbf{x} &= \int_{B(\varrho)\setminus B(r)} \mathbb{P}_{MS}^{(r)}(\mathbf{x})\, d\mathbf{x} \\ &= \int_{B(\varrho)\setminus B(r)} -\nabla\left(\frac{\mathbf{x}}{|\mathbf{x}|^3}\right) d\mathbf{x} \\ &= \int_{\partial B(r)} \frac{\hat{\mathbf{n}}\otimes\hat{\mathbf{n}}}{|\mathbf{x}|^2}\, d\mathbf{x} - \int_{\partial B(\varrho)} \frac{\hat{\mathbf{n}}\otimes\hat{\mathbf{n}}}{|\mathbf{x}|^2}\, d\mathbf{x} \\ &= \mathbf{0}.\end{aligned}$$

□

Lemma 2. *let $\mathbb{K}(\mathbf{x})$ and $\mathbb{P}_{MS}^{(r)}(\mathbf{x})$ be defined as Eq. (6.28) and Eq. (6.43) respectively, we have $\mathbb{P}_{MS}^{(r)}(\mathbf{x})$ converges to $\mathbb{K}(\mathbf{x}) + \frac{1}{3}\mathbf{I}\delta_0$ in the sense of distribution, i.e.*

$$\mathbb{P}_{MS}^{(r)}(\mathbf{x}) \to \mathbb{K}(\mathbf{x}) + \frac{1}{3}\mathbf{I}\delta_0 \tag{6.47}$$

in $\mathcal{D}'$ as $r \to 0$.

Proof. This proof follows James and Müller (1994) page 298. □

Lemma 3. *Let $\overline{\mathbb{K}}(\mathbf{x})$ and $\overline{\mathbb{P}}_{MS}^{(r)}(\mathbf{x})$ be defined as*

$$\overline{\mathbb{K}}(\mathbf{x}) = \hat{\mathbf{d}}\cdot\mathbb{K}(\mathbf{x})\hat{\mathbf{d}} \tag{6.48}$$

$$\overline{\mathbb{P}}_{MS}^{(r)}(\mathbf{x}) = \hat{\mathbf{d}}\cdot\mathbb{P}_{MS}^{(r)}(\mathbf{x})\hat{\mathbf{d}} \tag{6.49}$$

then

$$\int_{\partial B(\varrho)} \overline{\mathbb{P}}_{MS}^{(r)}(\mathbf{x})\, d\mathbf{x} = 0, \tag{6.50}$$

$$\int_{B(\varrho)} \overline{\mathbb{P}}_{MS}^{(r)}(\mathbf{x})\, d\mathbf{x} = 0. \tag{6.51}$$

and

$$\overline{\mathbb{P}}_{MS}^{(r)}(\mathbf{x}) \to \overline{\mathbb{K}}(\mathbf{x}) + \frac{1}{3}\delta_0 \tag{6.52}$$

Proof. (i).

$$\int_{\partial B(\varrho)} \overline{\mathbb{P}}_{MS}^{(r)}(\mathbf{x})\, d\mathbf{x} = \hat{\mathbf{d}}\cdot\left(\int_{\partial B(\varrho)} \mathbb{P}_{MS}^{(r)}(\mathbf{x})\, d\mathbf{x}\right)\hat{\mathbf{d}} = 0,$$

$$\int_{B(\varrho)} \overline{\mathbb{P}}^{(r)}_{MS}(\mathbf{x})\, d\mathbf{x} = \hat{\mathbf{d}} \cdot \left(\int_{B(\varrho)} \mathbb{P}^{(r)}_{MS}(\mathbf{x})\, d\mathbf{x} \right) \hat{\mathbf{d}} = 0.$$

(ii). We have by Lemma 2

$$\mathbb{P}^{(r)}_{MS}(\mathbf{x}) \to \mathbb{K}(\mathbf{x}) + \frac{1}{3}\mathbf{I}\delta_0,$$

thus

$$\overline{\mathbb{P}}^{(r)}_{MS}(\mathbf{x}) = \hat{\mathbf{d}} \cdot \mathbb{P}^{(r)}_{MS}(\mathbf{x})\hat{\mathbf{d}} \to \hat{\mathbf{d}} \cdot \left(\mathbb{K}(\mathbf{x}) + \frac{1}{3}\mathbf{I}\delta_0 \right) \hat{\mathbf{d}} = \overline{\mathbb{K}}(\mathbf{x}) + \frac{1}{3}\delta_0$$

as $r \to 0$.

□

6.4 From Discrete to Continuum

6.4.1 Energy in Integral Form

By defining

$$J_\lambda(\mathbf{x}, \mathbf{y}) = \sum_{\substack{\mathbf{v},\mathbf{w} \in \mathcal{L}_\lambda \\ \mathbf{v} \neq \mathbf{w}}} \chi_{\mathbf{v}+\lambda U}(\mathbf{x}) \left\{ \frac{1}{(\lambda\epsilon)^2} \left(\frac{1}{\left|\mathbf{v} - \mathbf{w} + \lambda\epsilon\hat{\mathbf{d}}\right|} - \frac{2}{|\mathbf{v} - \mathbf{w}|} + \frac{1}{\left|\mathbf{v} - \mathbf{w} - \lambda\epsilon\hat{\mathbf{d}}\right|} \right) \right\} \chi_{\mathbf{w}+\lambda U}(\mathbf{y}), \tag{6.53}$$

we can rewrite the energy expression in Eq. (6.23) as

$$\mathcal{E}_\lambda = -\frac{1}{2} \int_{\mathbb{R}^3} \int_{\mathbb{R}^3} p_\lambda(\mathbf{x}) J_\lambda(\mathbf{x}, \mathbf{y}) p_\lambda(\mathbf{y})\, d\mathbf{x}\, d\mathbf{y}. \tag{6.54}$$

Or,

$$\mathcal{E}_\lambda = -\frac{1}{2} < p_\lambda, T_\lambda p_\lambda >_{L^2} \tag{6.55}$$

where

$$T_\lambda p := \int_{\mathbb{R}^3} J_\lambda(\mathbf{x}, \mathbf{y}) p(\mathbf{y})\, d\mathbf{y} \tag{6.56}$$

Proposition 4. *The map*

$$T_\lambda : p \to \int_{\mathbb{R}^3} J_\lambda(., \mathbf{y}) p(\mathbf{y})\, d\mathbf{y} \tag{6.57}$$

defined on $C_0^\infty(\mathbb{R}^3,\mathbb{R})$ *extends to a bounded linear map from* $L^2(\mathbb{R}^3,\mathbb{R})$ *to* $L^2(\mathbb{R}^3,\mathbb{R})$. *Moreover,*

$$\|T_\lambda\|_{\mathcal{L}(L^2,L^2)} = \|T_1\|_{\mathcal{L}(L^2,L^2)}, \quad \forall \quad \lambda > 0. \tag{6.58}$$

Proof. First, we assume that T_1 is a bounded linear map from $L^2(\mathbb{R}^3,\mathbb{R})$ to $L^2(\mathbb{R}^3,\mathbb{R})$. From the definition of $J_\lambda(\mathbf{x},\mathbf{y})$, it is easy to see

$$J_\lambda(\mathbf{x},\mathbf{y}) = \frac{1}{\lambda^3} J_1(\frac{\mathbf{x}}{\lambda},\frac{\mathbf{y}}{\lambda}). \tag{6.59}$$

Set

$$\left(S_\lambda f\right)(\mathbf{x}) := \lambda^{\frac{3}{2}} f(\lambda\mathbf{x}), \quad \mathbf{x}\in\mathbb{R}^3. \tag{6.60}$$

It is easy to prove that

$$\|f(\mathbf{x})\|_{L^2} = \|\lambda^{\frac{3}{2}} f(\lambda\mathbf{x})\|_{L^2}$$

so that

$$\|f\|_{L^2} = \|Sf\|_{L^2}$$

and S is an isometry from $L^2(\mathbb{R}^3,\mathbb{R})$ to $L^2(\mathbb{R}^3,\mathbb{R})$.

Therefore,

$$\begin{aligned}
(T_\lambda p)(\mathbf{x}) &= \int_{\mathbf{R}^3} J_\lambda(\mathbf{x},\mathbf{y}) p(\mathbf{y})\, d\mathbf{y} \\
&= \int_{\mathbf{R}^3} \frac{1}{\lambda^3} J_1(\frac{\mathbf{x}}{\lambda},\frac{\mathbf{y}}{\lambda}) p(\mathbf{y})\, d\mathbf{y} \\
&= \int_{\mathbf{R}^3} \frac{1}{\lambda^3} J_1(\frac{\mathbf{x}}{\lambda},\mathbf{z}) p(\lambda\mathbf{z})\, d\lambda\mathbf{z} \\
&= \int_{\mathbf{R}^3} J_1(\frac{\mathbf{x}}{\lambda},\mathbf{z}) p(\lambda\mathbf{z})\, d\mathbf{z} \\
&= \int_{\mathbf{R}^3} J_1(\frac{\mathbf{x}}{\lambda},\mathbf{z}) \lambda^{-\frac{3}{2}} S_\lambda p(\mathbf{z})\, d\mathbf{z} \\
&= T_1(\lambda^{-\frac{3}{2}} S_\lambda p)(\frac{\mathbf{x}}{\lambda}) \\
&= \lambda^{-\frac{3}{2}} T_1(S_\lambda p)(\frac{\mathbf{x}}{\lambda}).
\end{aligned}$$

From the definition of S_λ in (6.60), we have

$$S_\lambda^{-1}\left(\lambda^{\frac{3}{2}} f(\lambda\mathbf{x})\right) = f(\mathbf{x}),$$

$$S_\lambda^{-1}\left(f(\lambda \mathbf{x})\right) = \lambda^{-\frac{3}{2}} f(\mathbf{x}),$$

$$S_\lambda^{-1}\left(f(\mathbf{y})\right) = \lambda^{-\frac{3}{2}} f(\frac{\mathbf{y}}{\lambda}).$$

Thus

$$(T_\lambda p)(\mathbf{x}) = \lambda^{-\frac{3}{2}} T_1(S_\lambda p)(\frac{\mathbf{x}}{\lambda}) = S_\lambda^{-1} T_1(S_\lambda p)(\mathbf{x}).$$

Therefore,

$$\|T_\lambda\|_{\mathcal{L}(L^2,L^2)} = \|T_1\|_{\mathcal{L}(L^2,L^2)}, \quad \forall \quad \lambda > 0.$$

We now prove that T_1 extends to a bounded linear map from $L^2(\mathbb{R}^3,\mathbb{R})$ to $L^2(\mathbb{R}^3,\mathbb{R})$. From the review in Section 6.3.2, we need to prove:

$$\|T_1 p\,\|_{L^2} \leq c\|p\|_{L^2}, \quad \forall \quad p \in C_0^\infty(\mathbb{R}^3,\mathbb{R}) \quad \text{for some constant } c. \tag{6.61}$$

In order to prove Eq. (6.61), we first define

$$L^{(r)}(\mathbf{x},\mathbf{y}) := J_1(\mathbf{x},\mathbf{y}) - \overline{\mathbb{P}}_{MS}^{(r)}(\mathbf{x}-\mathbf{y}). \tag{6.62}$$

We will prove in Lemma 9 that there exists a function $g^{(r)} \in L^1(\mathbb{R}^3,\mathbb{R})$, such that

$$\left|L^{(r)}(\mathbf{x},\mathbf{y})\right| \leq g^{(r)}(|\mathbf{x}-\mathbf{y}|). \tag{6.63}$$

By a standard result on convolution (See for example, Wheeden and Zygmund, 1977, Ch. 9),

$$\begin{aligned}\left\|\int_{\mathbb{R}^3} L^{(r)}(\mathbf{x},\mathbf{y})p(\mathbf{y})\,d\mathbf{y}\right\|_{L^2} &\leq \left\|\int_{\mathbb{R}^3} g^{(r)}(|\mathbf{x}-\mathbf{y}|)p(\mathbf{y})\,d\mathbf{y}\right\|_{L^2} \\ &\leq \left\|g^{(r)}\right\|_{L_1} \|p\|_{L_2}\,, \qquad \forall \quad p \in C_0^\infty(\mathbb{R}^3,\mathbb{R}).\end{aligned} \tag{6.64}$$

In Lemma 3, we prove that

$$\int_{\partial B(r)} \overline{\mathbb{P}}_{MS}^{(r)}(\mathbf{x})\,d\mathbf{x} = 0.$$

By a standard result in singular integral (For example, Stein, 1970, Ch. 2), we obtain,

$$\left\| \int_{\mathbb{R}^3} \overline{\mathbb{P}}_{MS}^{(r)}(\mathbf{x}-\mathbf{y}) p(\mathbf{y})\, d\mathbf{y} \right\|_{L^2} \leq A\|p\|_{L^2} \tag{6.65}$$

where A is a constant and independent of p.

The results follows by combining Eq. (6.64) and Eq. (6.65). □

Theorem 5. *Let*

$$d_\lambda(\mathbf{x}) = \int_{\mathbf{x}+\lambda U} p_\lambda(\mathbf{z})\, d\mathbf{z} \tag{6.66}$$

and suppose

$$p_\lambda \to p \quad in \quad L^2(\mathbb{R}^3, \mathbb{R}). \tag{6.67}$$

Let T_λ be defined as Eq. (6.56), and let $\mathcal{E}_\lambda$ be given as Eq. (6.55), then

$$T_\lambda p_\lambda \to \overline{\mathbb{K}} * p + \left(\frac{1}{3} + \overline{\mathbb{S}}\right) p \quad in \quad L^2(\mathbb{R}^3, \mathbb{R}) \tag{6.68}$$

and

$$\mathcal{E}_\lambda \to -\frac{1}{2}\left(< p, \overline{\mathbb{K}} * p >\right) + \frac{1}{3}\|p\|^2 + < p, \overline{\mathbb{S}} p > \tag{6.69}$$

where $\overline{\mathbb{K}}$ is the kernel defined in Eq. (6.48) and

$$\overline{\mathbb{S}} := \lim_{\varrho \to \infty} \sum_{\mathbf{y} \in (\mathcal{L}_1 \cap B(\varrho)) \setminus \{o\}} K_1(\mathbf{y}) \tag{6.70}$$

Proof. Since

$$\|T_\lambda(p_\lambda - p)\| \leq \|T_\lambda\|\, \|p_\lambda - p\| = \|T_1\|\, \|p_\lambda - p\| \tag{6.71}$$

we obtain

$$\lim_{\lambda \to 0} T_\lambda(p_\lambda - p) \to 0. \tag{6.72}$$

Hence,

$$\lim_{\lambda \to 0} T_\lambda p_\lambda = \lim_{\lambda \to 0} \left(T_\lambda p + T_\lambda(p_\lambda - p)\right) = \lim_{\lambda \to 0} T_\lambda p = \lim_{k \to \infty} \lim_{\lambda \to 0} T_\lambda p^k \tag{6.73}$$

where

$$p^k \to k \quad \text{in} \quad L^2(\mathbb{R}^3, \mathbb{R}), p^k \in C_0^\infty(\mathbb{R}^3, \mathbb{R}). \tag{6.74}$$

Therefore, we only need to consider $p \in C_0^\infty(\mathbb{R}^3, \mathbb{R})$.

Now, by recourse to Eq. (6.59) and (6.62), we have

$$\begin{aligned} J_\lambda(\mathbf{x},\mathbf{y}) &= \lambda^{-3}\overline{\mathbb{P}}^{(r)}_{MS}\left(\frac{\mathbf{x}-\mathbf{y}}{\lambda}\right) + \lambda^{-3}L^{(r)}\left(\frac{\mathbf{x}}{\lambda},\frac{\mathbf{y}}{\lambda}\right) \\ &= \overline{\mathbb{P}}^{(r\lambda)}_{MS}\left(\mathbf{x}-\mathbf{y}\right) + \lambda^{-3}L^{(r)}\left(\frac{\mathbf{x}}{\lambda},\frac{\mathbf{y}}{\lambda}\right) \end{aligned} \tag{6.75}$$

Since the limiting behavior of $\overline{\mathbb{P}}^{(r\lambda)}_{MS}$ as $\lambda \to 0$ is known by Lemma 3, we only need to consider $L^{(r)}$.

First, we write

$$\begin{aligned} &\lambda^{-3}\int_{\mathbb{R}^3} L^{(r)}\left(\frac{\mathbf{x}}{\lambda},\frac{\mathbf{y}}{\lambda}\right)p(\mathbf{y})\,d\mathbf{y} \\ &= \int_{\mathbb{R}^3} \lambda^{-3}\text{Ł}^{(r)}\left(\frac{\mathbf{x}}{\lambda},\frac{\mathbf{y}}{\lambda}\right)\,d\mathbf{y}p(\mathbf{x}) \\ &\quad - \int_{|\mathbf{x}-\mathbf{y}\geq R\lambda|} \lambda^{-3}L^{(r)}\left(\frac{\mathbf{x}}{\lambda},\frac{\mathbf{y}}{\lambda}\right)\,d\mathbf{y}p(\mathbf{x}) \\ &\quad + \int_{|\mathbf{x}-\mathbf{y}\leq R\lambda|} \lambda^{-3}L^{(r)}\left(\frac{\mathbf{x}}{\lambda},\frac{\mathbf{y}}{\lambda}\right)\left(p(\mathbf{y})-p(\mathbf{x})\right)d\mathbf{y} \\ &\quad + \int_{|\mathbf{x}-\mathbf{y}\geq R\lambda|} \lambda^{-3}L^{(r)}\left(\frac{\mathbf{x}}{\lambda},\frac{\mathbf{y}}{\lambda}\right)p(\mathbf{y})\,d\mathbf{y}. \end{aligned} \tag{6.76}$$

We now consider the limit of Eq. (6.76). First let $\lambda \to 0$ with R fixed, we have

$$\lim_{\lambda\to 0}\int_{|\mathbf{x}-\mathbf{y}\leq R\lambda|} \lambda^{-3}L^{(r)}\left(\frac{\mathbf{x}}{\lambda},\frac{\mathbf{y}}{\lambda}\right)\left(p(\mathbf{y})-p(\mathbf{x})\right)d\mathbf{y} \to 0 \tag{6.77}$$

since $p \in C_0^\infty(\mathbb{R}^3,\mathbb{R})$.

We also notice that for any $R > 0$, we have

$$\begin{aligned} &\int_{|\mathbf{x}-\mathbf{y}\geq R\lambda|} \lambda^{-3}\left|L^{(r)}\left(\frac{\mathbf{x}}{\lambda},\frac{\mathbf{y}}{\lambda}\right)\right|\,d\mathbf{y} \\ &\leq C\lambda\int_{|\mathbf{x}-\mathbf{y}|\geq R\lambda}\frac{1}{|\mathbf{x}-\mathbf{y}|^4}\,d\mathbf{y} \\ &= C\lambda\int_{|\mathbf{z}|\geq R\lambda}\frac{1}{|\mathbf{z}|^4}\,d\mathbf{z} \\ &= 4\pi C\lambda\left(-\frac{1}{r}\right)\Bigg|_{R\lambda}^{\infty} = \frac{4\pi C}{R} = \frac{C'}{R} \end{aligned} \tag{6.78}$$

where C, C' are independent of λ.

Thus,

$$\int_{|\mathbf{x}-\mathbf{y}|\geq R\lambda} \lambda^{-3} L^{(r)}\left(\frac{\mathbf{x}}{\lambda}, \frac{\mathbf{y}}{\lambda}\right) d\mathbf{y} p(\mathbf{x}) \leq \frac{C'}{R} \max_{\mathbb{R}^3} |p(\mathbf{x})| \to 0 \quad \text{as} \quad R \to \infty, \tag{6.79}$$

and

$$\begin{aligned} &\left| \int_{|\mathbf{x}-\mathbf{y}|\geq R\lambda} \lambda^{-3} L^{(r)}\left(\frac{\mathbf{x}}{\lambda}, \frac{\mathbf{y}}{\lambda}\right) p(\mathbf{y})\, d\mathbf{y} \right| \\ &\leq \left| \int_{|\mathbf{x}-\mathbf{y}\geq R\lambda|} \lambda^{-3} L^{(r)}\left(\frac{\mathbf{x}}{\lambda}, \frac{\mathbf{y}}{\lambda}\right) d\mathbf{y} \right| \max_{\mathbb{R}^3} |p(\mathbf{y})| \\ &= \frac{C'}{R} \max_{\mathbb{R}^3} |p(\mathbf{x})| \to 0 \quad \text{as} \quad R \to \infty. \end{aligned} \tag{6.80}$$

Combining Eq. (6.76), (6.77), (6.79) and (6.80), we obtain

$$\begin{aligned} &\lambda^{-3} \int_{\mathbb{R}^3} L^{(r)}\left(\frac{\mathbf{x}}{\lambda}, \frac{\mathbf{y}}{\lambda}\right) p(\mathbf{y})\, d\mathbf{y} \\ &= \int_{\mathbb{R}^3} \lambda^{-3} L^{(r)}\left(\frac{\mathbf{x}}{\lambda}, \frac{\mathbf{y}}{\lambda}\right) d\mathbf{y} p(\mathbf{x}) \\ &= \int_{\mathbb{R}^3} L^{(r)}\left(\frac{\mathbf{x}}{\lambda}, \mathbf{y}\right) d\mathbf{y} p(\mathbf{x}) \\ &= \int_{\mathbb{R}^3} L^{(r)}(0, \mathbf{y})\, d\mathbf{y} p(\mathbf{x}). \end{aligned} \tag{6.81}$$

The last equality comes from Lemma 10 which we will prove shortly.

Finally, we define

$$\overline{\mathbb{S}} = \int_{\mathbb{R}^3} L^{(r)}(0, \mathbf{y})\, d\mathbf{y}, \tag{6.82}$$

it can be rewritten as

$$\begin{aligned} \overline{\mathbb{S}} &= \int_{\mathbb{R}^3} L^{(r)}(0, \mathbf{y})\, d\mathbf{y} \\ &= \lim_{\varrho \to \infty} \int_{B(\varrho)} L^{(r)}(0, \mathbf{y})\, d\mathbf{y} \\ &= \lim_{\varrho \to \infty} \int_{B(\varrho)} J_1(0, \mathbf{y}) - \overline{\mathbb{P}}^{(r)}_{MS}(-\mathbf{y})\, d\mathbf{y} \\ &= \lim_{\varrho \to \infty} \int_{B(\varrho)} J_1(0, \mathbf{y})\, d\mathbf{y} \\ &= \lim_{\varrho \to \infty} \sum_{\mathbf{y} \in (L_1 \cap B(\varrho)) \setminus \{\mathbf{0}\}} K_1(\mathbf{y}) \end{aligned} \tag{6.83}$$

By combining Eq. (6.52), (6.56), (6.75), (6.81), and also by the argument we have at the beginning of the proof, we conclude that as $\lambda \to 0$,

$$T_\lambda p_\lambda \to \overline{\mathbb{K}} * p + \left(\frac{1}{3} + \overline{\mathbb{S}}\right) p \quad \text{in} \quad L^2(\mathbb{R}^3, \mathbb{R}),$$

and

$$\mathcal{E}_\lambda \to -\frac{1}{2}\left(< p, \overline{\mathbb{K}} * p >\right) + \frac{1}{3}\|p\|^2 + < p, \mathbb{S}p > .$$

□

Theorem 6. *Let*

$$d_\lambda(\mathbf{x}) = \int_{\mathbf{x}+\lambda U} p_\lambda(\mathbf{z})\, d\mathbf{z} \tag{6.84}$$

and suppose

$$p_\lambda \to p \quad \textit{in} \quad L^2(\mathbb{R}^3, \mathbb{R}). \tag{6.85}$$

Let $\mathcal{E}_\lambda$ be given as Eq. (6.55), and define

$$\mathbf{p}_\lambda = p_\lambda\, \hat{\mathbf{d}} \quad \textit{and} \quad \mathbf{p} = p\, \hat{\mathbf{d}}, \tag{6.86}$$

then

$$\mathcal{E}_\lambda \to -\frac{1}{2}\left(< \mathbf{p}, \mathbb{K} * \mathbf{p} >\right) + \frac{1}{3}\|\mathbf{p}\|^2 + < \mathbf{p}, \mathbb{S}\mathbf{p} > \tag{6.87}$$

where $\mathbb{K}$ is the field of a dipole defined in Eq. (6.28) and

$$\mathbb{S} := \lim_{\varrho \to \infty} \sum_{\mathbf{y} \in (\mathcal{L}_1 \cap B(\varrho)) \setminus \{o\}} K_1(\mathbf{y}) \hat{\mathbf{d}} \otimes \hat{\mathbf{d}}. \tag{6.88}$$

Proof. The proof is straightforward following Theorem 5, and the definition of $\overline{\mathbb{K}}$ and $\overline{\mathbb{S}}$. □

Remark 7. *The expression in Eq. 6.87 consists a long-range term*

$$-\frac{1}{2}\left(< \mathbf{p}, \mathbb{K} * \mathbf{p} >\right) \tag{6.89}$$

and a local contribution

$$\frac{1}{3}\|\mathbf{p}\|^2 + < \mathbf{p}, \mathbb{S}\mathbf{p} > . \tag{6.90}$$

which is the energy caused by Lorentz local field, and can be incorporated into the deformation

energy as we have discussed before.

The long-range term is equal to

$$\int_{\mathbb{R}^3} \frac{\epsilon_0}{2} |\nabla \phi|^2 \, d\mathbf{x} \tag{6.91}$$

which is exactly the field energy we used in Chapter 3. This can be easily seen by looking at the weak form of Maxwell equation

$$-\int_{\mathbb{R}^3} (-\epsilon_0 \nabla \phi + \mathbf{p}) \cdot \nabla \psi \, d\mathbf{x} = 0, \quad \forall \quad \psi \in H^1(\mathbb{R}^3) \tag{6.92}$$

and setting $\psi = \phi$.

6.4.2 Technical Lemmas

It remains to prove the following technical lemmas.

Lemma 8. *Let* d_λ *defined on* $\mathcal{L}_\lambda$, *and* $d_\lambda^\sim$ *defined by*

$$d_\lambda^\sim(\mathbf{z}) = \lambda^{-3} d_\lambda(\mathbf{x}) \quad \textit{for} \quad \mathbf{z} \in \mathbf{x} + \lambda U \quad \textit{and} \quad \mathbf{x} \in \mathcal{L}_\lambda. \tag{6.93}$$

If

$$d_\lambda^\sim \to p \quad \textit{in} \quad L^2(\mathbb{R}^3, \mathbb{R}), \tag{6.94}$$

then there exists a background field $p_\lambda \in L^2(\mathbb{R}^3, \mathbb{R})$ *with*

$$d_\lambda(\mathbf{x}) = \int_{\mathbf{x}+\lambda U} p_\lambda(\mathbf{z}) \, d\mathbf{z} \tag{6.95}$$

and

$$p_\lambda \to p \quad \textit{in} \quad L^2(\mathbb{R}^3, \mathbb{R}). \tag{6.96}$$

Conversely, if there exists a background field $p_\lambda \in L^2(\mathbb{R}^3, \mathbb{R})$ *with*

$$d_\lambda(\mathbf{x}) = \int_{\mathbf{x}+\lambda U} p_\lambda(\mathbf{z}) \, d\mathbf{z}$$

is convergent to some p *in* $L^2(\mathbb{R}^3, \mathbb{R})$, *then* $d_\lambda^\sim$ *defined by*

$$d_\lambda^\sim(\mathbf{z}) = \lambda^{-3} d_\lambda(\mathbf{x}) \quad \textit{for} \quad \mathbf{z} \in \mathbf{x} + \lambda U \quad \textit{and} \quad \mathbf{x} \in \mathcal{L}_\lambda. \tag{6.97}$$

is convergent to p in $L^2(\mathbb{R}^3, \mathbb{R})$.

Proof. This proof follows James and Müller (1994) page 301-303. □

Lemma 9. *Let*

$$L^{(r)}(\mathbf{x}, \mathbf{y}) := J_1(\mathbf{x}, \mathbf{y}) - \overline{\mathbb{P}}^{(r)}_{MS}(\mathbf{x} - \mathbf{y}), \tag{6.98}$$

with $J_1(\mathbf{x}, \mathbf{y})$ *and* $\overline{\mathbb{P}}^{(r)}_{MS}$ *defined by Eq. (6.53) and Eq. (6.49) respectively, then there exists a function* $g^{(r)} \in L^1(\mathbb{R}^3, \mathbb{R})$*, such that*

$$\left| L^{(r)}(\mathbf{a}, \mathbf{b}) \right| \leq g^{(r)}(|\mathbf{a} - \mathbf{b}|), \quad \forall\, \mathbf{a}, \mathbf{b} \in \mathbb{R}^3. \tag{6.99}$$

Proof. We prove the Lemma in two steps.

(i). We first prove that for any R satisfying $\operatorname{diam} U + r < R < \infty$, any $\mathbf{a}$, $\mathbf{b}$ satisfying $|\mathbf{a} - \mathbf{b}| < R$, $\exists\ g_1 \in L_1(B(R), \mathbb{R})$, such that

$$\left| L^{(r)}(\mathbf{a} - \mathbf{b}) \right| \leq g_1(|\mathbf{a} - \mathbf{b}|). \tag{6.100}$$

(a) When $|\mathbf{a} - \mathbf{b}| < r$, and $\mathbf{a}$, $\mathbf{b}$ are in the same cell, then $\overline{\mathbb{P}}^{(r)}_{MS} = 0$, $K_1(\mathbf{a}, \mathbf{b}) = 0$, thus

$$L^{(r)}(\mathbf{a}, \mathbf{b}) = 0.$$

(b) When $|\mathbf{a} - \mathbf{b}| < r$, but $\mathbf{a}$, $\mathbf{b}$ are not in the same cell, then $\overline{\mathbb{P}}^{(r)}_{MS} = 0$, and

$$\left| L^{(r)}(\mathbf{a}, \mathbf{b}) \right| = |J_1(\mathbf{a}, \mathbf{b})| = |K_1(\mathbf{x}_1(\mathbf{a}) - \mathbf{x}_1(\mathbf{b}))| < \infty.$$

Here, $\mathbf{x}_1(\mathbf{a})$ is the *corner map* defined as

$$\mathbf{x}_\lambda(\mathbf{y}) = \mathbf{x} \quad \text{for} \quad \mathbf{y} = \mathbf{x} + \lambda U, \quad , \mathbf{x} \in L_\lambda. \tag{6.101}$$

(c) When $|\mathbf{a} - \mathbf{b}| > r$, and $\mathbf{a}$, $\mathbf{b}$ are in the same cell, then $K_1(\mathbf{a}, \mathbf{b}) = 0$, and

$$\left| L^{(r)}(\mathbf{a}, \mathbf{b}) \right| = \left| \overline{\mathbb{P}}^{(r)}_{MS}(\mathbf{a} - \mathbf{b}) \right| < \infty, \tag{6.102}$$

(d) When $|\mathbf{a} - \mathbf{b}| > r$, but $\mathbf{a}$, $\mathbf{b}$ are not in the same cell, by definition of $\overline{\mathbb{P}}^{(r)}_{MS}$ and

$K_1(\mathbf{a},\mathbf{b})$, we still have

$$\left|L^{(r)}(\mathbf{a},\mathbf{b})\right| = \left|K_1(\mathbf{x}_1(\mathbf{a})-\mathbf{x}_1(\mathbf{b})) - \overline{\mathbb{P}}^{(r)}_{MS}(\mathbf{a}-\mathbf{b})\right| < \infty, \tag{6.103}$$

Therefore, when $\operatorname{diam} U + r < R < \infty$ and $|\mathbf{a}-\mathbf{b}| < R$, $\left|L^{(r)}(\mathbf{a},\mathbf{b})\right|$ is always bounded. We can always pick some function $g_1 \in L_\infty(B(R),\mathbb{R}) \subset L_1(B(R),\mathbb{R})$, such that

$$\left|L^{(r)}(\mathbf{a},\mathbf{b})\right| \le g_1(|\mathbf{a}-\mathbf{b}|). \tag{6.104}$$

(ii). We now prove that for R large enough satisfying $\operatorname{diam} U + r < R < \infty$, any $\mathbf{a}$, $\mathbf{b}$ satisfying $|\mathbf{a}-\mathbf{b}| > R$, $\exists\ g_2(|\mathbf{x}|) \in L_1(\mathbb{R}^3/B(R),\mathbb{R})$ such that

$$\left|L^{(r)}(\mathbf{a}-\mathbf{b})\right| \le g_2(|\mathbf{a}-\mathbf{b}|). \tag{6.105}$$

According to the definition of $L^{(r)}$,

$$\begin{aligned}\left|L^{(r)}(\mathbf{a},\mathbf{b})\right| = \Bigg|&\frac{1}{\epsilon^2}\left(\frac{1}{|\mathbf{x}_1(\mathbf{a})-\mathbf{x}_1(\mathbf{b})+\epsilon\hat{\mathbf{d}}|} - \frac{2}{|\mathbf{x}_1(\mathbf{a})-\mathbf{x}_1(\mathbf{b})|} + \frac{1}{|\mathbf{x}_1(\mathbf{a})-\mathbf{x}_1(\mathbf{b})-\epsilon\hat{\mathbf{d}}|}\right)\\ &-\frac{3}{|\mathbf{a}-\mathbf{b}|^3}\frac{\hat{\mathbf{d}}\cdot(\mathbf{a}-\mathbf{b})}{|\mathbf{a}-\mathbf{b}|}\otimes\frac{(\mathbf{a}-\mathbf{b})\cdot\hat{\mathbf{d}}}{|\mathbf{a}-\mathbf{b}|} + \frac{1}{|\mathbf{a}-\mathbf{b}|^3}\Bigg|\end{aligned} \tag{6.106}$$

In Lemma 10, we will prove that

$$|(\mathbf{x}_1(\mathbf{a})-\mathbf{x}_1(\mathbf{b})) - (\mathbf{a}-\mathbf{b})| \le 2\operatorname{diam} U, \quad \forall \quad \mathbf{a},\mathbf{b} \in \mathbb{R}^3.$$

Thus, if we let $\mathbf{x} = \mathbf{a}-\mathbf{b}$, we can denote

$$\mathbf{x}_1(\mathbf{a})-\mathbf{x}_1(\mathbf{b}) = \mathbf{x} + \triangle, \tag{6.107}$$

where $|\triangle| \le 2\operatorname{diam} U$.

Therefore, we can rewrite Eq. (6.106) as

$$\begin{aligned}\left|L^{(r)}(\mathbf{a},\mathbf{b})\right| = \Bigg|\frac{1}{\epsilon^2}\left(\frac{1}{|\mathbf{x}+\triangle+\epsilon\hat{\mathbf{d}}|}-\frac{2}{|\mathbf{x}+\triangle|}+\frac{1}{|\mathbf{x}+\triangle-\epsilon\hat{\mathbf{d}}|}\right)\\ -\frac{3}{|\mathbf{x}|^3}\frac{\hat{\mathbf{d}}\cdot\mathbf{x}}{|\mathbf{x}|}\otimes\frac{\mathbf{x}\cdot\hat{\mathbf{d}}}{|\mathbf{x}|}+\frac{1}{|\mathbf{x}|^3}\Bigg|.\end{aligned} \tag{6.108}$$

Also, we can choose R big enough such that $\mathbf{x}$, $\mathbf{x}+\triangle+\epsilon\hat{\mathbf{d}}$, $\mathbf{x}+\triangle-\epsilon\hat{\mathbf{d}}$ are far away from zero.

Since

$$\left(\frac{1}{|\mathbf{x}|}\right)' = -\frac{\mathbf{x}}{|\mathbf{x}|^3}, \tag{6.109}$$

$$\left(\frac{1}{|\mathbf{x}|}\right)'' = -\frac{3\mathbf{x}\otimes\mathbf{x}}{|\mathbf{x}|^5}-\frac{\mathbf{I}}{|\mathbf{x}|^3}, \tag{6.110}$$

$$\left(\frac{1}{|\mathbf{x}|}\right)'''_{ijk} = -\frac{15x_ix_jx_j}{|\mathbf{x}|^7}+\frac{3(x_i\delta_{jk}+x_j\delta_{ik}+x_k\delta_{ij})}{|\mathbf{x}|^5}, \tag{6.111}$$

by Taylor expansion around $\mathbf{x}+\triangle$, we obtain

$$\begin{aligned}\frac{1}{|\mathbf{x}+\triangle+\epsilon\hat{\mathbf{d}}|} = \frac{1}{|\mathbf{x}+\triangle|}-\frac{1}{|\mathbf{x}+\triangle|^3}(\mathbf{x}+\triangle)\cdot\epsilon\hat{\mathbf{d}}\\ +\frac{3}{2|\mathbf{x}+\triangle|^5}\epsilon\hat{\mathbf{d}}\cdot(\mathbf{x}+\triangle)\otimes(\mathbf{x}+\triangle)\cdot\epsilon\hat{\mathbf{d}}-\frac{|\epsilon\hat{\mathbf{d}}|}{2|\mathbf{x}+\triangle|^3}+f_1,\end{aligned} \tag{6.112}$$

where

$$f_1 = \frac{1}{6}\left\{(-15)\frac{[(\mathbf{x}+\triangle+\theta_1\epsilon\hat{\mathbf{d}})\cdot\epsilon\hat{\mathbf{d}}]^3}{|\mathbf{x}+\triangle+\theta_1\epsilon\hat{\mathbf{d}}|^7}+\frac{9\epsilon^2(\mathbf{x}+\triangle+\theta_1\epsilon\hat{\mathbf{a}})\cdot\epsilon\hat{\mathbf{d}}}{|\mathbf{x}+\triangle+\theta_1\epsilon\hat{\mathbf{d}}|^5}\right\} \tag{6.113}$$

with $0<\theta_1<1$. And

$$\begin{aligned}\frac{1}{|\mathbf{x}+\triangle-\epsilon\hat{\mathbf{d}}|} = \frac{1}{|\mathbf{x}+\triangle|}+\frac{1}{|\mathbf{x}+\triangle|^3}(\mathbf{x}+\triangle)\cdot\epsilon\hat{\mathbf{d}}\\ +\frac{3}{2|\mathbf{x}+\triangle|^5}\epsilon\hat{\mathbf{d}}\cdot(\mathbf{x}+\triangle)\otimes(\mathbf{x}+\triangle)\cdot\epsilon\hat{\mathbf{d}}-\frac{|\epsilon\hat{\mathbf{d}}|}{2|\mathbf{x}+\triangle|^3}+f_2,\end{aligned} \tag{6.114}$$

where

$$f_2 = -\frac{1}{6}\left\{(-15)\frac{[(\mathbf{x}+\triangle-\theta_2\epsilon\hat{\mathbf{d}})\cdot\epsilon\hat{\mathbf{d}}]^3}{|\mathbf{x}+\triangle-\theta_2\epsilon\hat{\mathbf{d}}|^7}+\frac{9\epsilon^2(\mathbf{x}+\triangle-\theta_2\epsilon\hat{\mathbf{a}})\cdot\epsilon\hat{\mathbf{d}}}{|\mathbf{x}+\triangle-\theta_2\epsilon\hat{\mathbf{d}}|^5}\right\} \tag{6.115}$$

with $0 < \theta_2 < 1$.

Substituting Eq. (6.112), (6.114) into Eq. (6.108), we have

$$\begin{aligned}
&\left|L^{(r)}(\mathbf{a}-\mathbf{b})\right| \\
&\leq \left|\left(\frac{3}{|\mathbf{x}+\triangle|^5}\hat{\mathbf{d}}\cdot(\mathbf{x}+\triangle)\otimes(\mathbf{x}+\triangle)\cdot\hat{\mathbf{d}}-\frac{1}{|\mathbf{x}+\triangle|^3}\right)-\frac{3}{|\mathbf{x}|^5}\hat{\mathbf{d}}\cdot\mathbf{x}\otimes\mathbf{x}\cdot\hat{\mathbf{d}}+\frac{1}{|\mathbf{x}|^3}\right| \\
&\quad+\left|\frac{f_1}{\epsilon^2}\right|+\left|\frac{f_2}{\epsilon^2}\right|
\end{aligned} \tag{6.116}$$

In light of Eq. (6.113), we have

$$\frac{f_1}{\epsilon^2} \leq \frac{1}{6}\left\{\frac{15\epsilon\left|(\mathbf{x}+\triangle+\theta_1\epsilon\hat{\mathbf{d}})\cdot\hat{\mathbf{d}}\right|^3}{|\mathbf{x}+\triangle+\theta_1\epsilon\hat{\mathbf{d}}|^7}+\frac{9\epsilon\left|(\mathbf{x}+\triangle+\theta_1\epsilon\hat{\mathbf{a}})\cdot\hat{\mathbf{d}}\right|}{|\mathbf{x}+\triangle+\theta_1\epsilon\hat{\mathbf{d}}|^5}\right\} \tag{6.117}$$

The first term on the right-hand side of Eq. (6.117) can be estimated as follows.

$$\begin{aligned}
\frac{15\epsilon\left|(\mathbf{x}+\triangle+\theta_1\epsilon\hat{\mathbf{d}})\cdot\epsilon\hat{\mathbf{d}}\right|^3}{|\mathbf{x}+\triangle+\theta_1\hat{\mathbf{d}}|^7} &= 15\epsilon\frac{\left|(\hat{\mathbf{x}}+\frac{\triangle}{\mathbf{x}}+\frac{\theta_1\epsilon\hat{\mathbf{d}}}{|\mathbf{x}|})\cdot\epsilon\hat{\mathbf{d}}\right|^3}{|\mathbf{x}|^4\left|\hat{\mathbf{x}}+\frac{\triangle}{\mathbf{x}}+\frac{\theta_1\epsilon\hat{\mathbf{d}}}{|\mathbf{x}|})\right|^7} \\
&\leq 15\epsilon\frac{\left||\hat{\mathbf{x}}\cdot\hat{\mathbf{d}}|+\frac{|\triangle\cdot\hat{\mathbf{d}}|}{|\mathbf{x}|}+\frac{\theta_1\epsilon}{|\mathbf{x}|}\right|^3}{|\mathbf{x}|^4\left|(\hat{\mathbf{x}}+\frac{\triangle}{|\mathbf{x}|}+\frac{\theta_1\epsilon\hat{\mathbf{d}}}{|\mathbf{x}|}\right|^7} \\
&\leq \frac{1+\frac{2\mathrm{diam}U}{\mathrm{diam}U}+\frac{\theta\epsilon}{\mathrm{diam}U}}{|\mathbf{x}|^4\left|\hat{\mathbf{x}}+\frac{\triangle}{|\mathbf{x}|}+\frac{\theta_1\epsilon\hat{\mathbf{d}}}{|\mathbf{x}|}\right|^7} \\
&\leq \frac{c_1}{|\mathbf{x}|^4}
\end{aligned} \tag{6.118}$$

for some constant $c_1 > 0$, since we can always choose R big enough, such that

$$\frac{|\triangle|}{|\mathbf{x}|} << 1, \quad \frac{\theta\epsilon}{|\mathbf{x}|} << 1, \tag{6.119}$$

thus

$$\left|\hat{\mathbf{x}}+\frac{\triangle}{|\mathbf{x}|}+\frac{\theta_1\epsilon\hat{\mathbf{d}}}{|\mathbf{x}|}\right| \geq \text{some constant} \sim 1. \tag{6.120}$$

We apply similar argument to the the second term on the right-hand side of Eq. (6.117),

and therefore obtain

$$\left|\frac{f_1}{\epsilon^2}\right| \leq \frac{A_1}{|\mathbf{x}|^4} \tag{6.121}$$

for some constant $A_1 > 0$.

Similarly, we can prove that

$$\left|\frac{f_2}{\epsilon^2}\right| \leq \frac{A_2}{|\mathbf{x}|^4} \tag{6.122}$$

for some constant $A_2 > 0$.

We now estimate the first term on the right-hand side of Eq. (6.116).

$$\begin{aligned}
&\left|\left(\frac{3}{|\mathbf{x}+\triangle|^5}\hat{\mathbf{d}}\cdot(\mathbf{x}+\triangle)\otimes(\mathbf{x}+\triangle)\cdot\hat{\mathbf{d}} - \frac{1}{|\mathbf{x}+\triangle|^3}\right) - \frac{3}{|\mathbf{x}|^5}\hat{\mathbf{d}}\cdot\mathbf{x}\otimes\mathbf{x}\cdot\hat{\mathbf{d}} + \frac{1}{|\mathbf{x}|^3}\right| \\
&= \left|\left(\frac{3}{|\mathbf{x}+\triangle|^5}\left(\hat{\mathbf{d}}\cdot\mathbf{x}\otimes\mathbf{x}\cdot\hat{\mathbf{d}}\right) - \frac{3}{|\mathbf{x}|^5}\left(\hat{\mathbf{d}}\cdot\mathbf{x}\otimes\mathbf{x}\cdot\hat{\mathbf{d}}\right)\right)\right. \\
&\quad + \left(\frac{1}{|\mathbf{x}|^3} - \frac{1}{|\mathbf{x}+\triangle|^3}\right) \\
&\quad + \left(\frac{3}{|\mathbf{x}+\triangle|^5}\hat{\mathbf{d}}\cdot(\mathbf{x}\otimes\triangle+\triangle\otimes\mathbf{x})\cdot\hat{\mathbf{d}}\right) \\
&\quad \left. + \left(\frac{3}{|\mathbf{x}+\triangle|^5}\hat{\mathbf{d}}\cdot(\triangle\otimes\triangle)\cdot\hat{\mathbf{d}}\right)\right| \\
&\leq \left|3\left(\frac{1}{|\mathbf{x}+\triangle|^5} - \frac{1}{|\mathbf{x}|^5}\right)\hat{\mathbf{d}}\cdot\mathbf{x}\otimes\mathbf{x}\cdot\hat{\mathbf{d}}\right| + \left|\frac{1}{|\mathbf{x}|^3} - \frac{1}{|\mathbf{x}+\triangle|^3}\right| \\
&\quad + \frac{3}{|\mathbf{x}+\triangle|^5}\left|\hat{\mathbf{d}}\cdot(\mathbf{x}\otimes\triangle+\triangle\otimes\mathbf{x})\cdot\hat{\mathbf{d}}\right| + \frac{3\left|\hat{\mathbf{d}}\cdot\triangle\right|^2}{|\mathbf{x}+\triangle|^5}
\end{aligned} \tag{6.123}$$

Obviously,

$$\frac{3}{|\mathbf{x}+\triangle|^5}\left|\hat{\mathbf{d}}\cdot(\mathbf{x}\otimes\triangle+\triangle\otimes\mathbf{x})\cdot\hat{\mathbf{d}}\right| \leq \frac{c_2}{|\mathbf{x}|^4}, \tag{6.124}$$

$$\frac{3|\hat{\mathbf{d}}\cdot\triangle|^2}{|\mathbf{x}+\triangle|^5} \leq \frac{c_3}{|\mathbf{x}|^4} \tag{6.125}$$

for some constant c_2, $c_3 > 0$.

By Taylor expansion of $\frac{1}{|\mathbf{x}+\triangle|^5}$ near $\mathbf{x}$, we obtain

$$\left|3\left(\frac{1}{|\mathbf{x}+\triangle|^5} - \frac{1}{|\mathbf{x}|^5}\right)\hat{\mathbf{d}}\cdot\mathbf{x}\otimes\mathbf{x}\cdot\hat{\mathbf{d}}\right| \leq \frac{c_4}{|\mathbf{x}|^4} \tag{6.126}$$

for some constant $c_4 > 0$.

Similarly, by Taylor expansion of $\frac{1}{|\mathbf{x}+\triangle|^3}$ near $\mathbf{x}$, we obtain

$$\left| \frac{1}{|\mathbf{x}|^3} - \frac{1}{|\mathbf{x}+\triangle|^3} \right| \leq \frac{c_5}{|\mathbf{x}|^4} \tag{6.127}$$

for some constant $c_5 > 0$.

Combining Eq. (6.123), (6.124), (6.125), (6.126), (6.127), we have

$$\left| \left(\frac{3}{|\mathbf{x}+\triangle|^5} \hat{\mathbf{d}} \cdot (\mathbf{x}+\triangle) \otimes (\mathbf{x}+\triangle) \cdot \hat{\mathbf{d}} - \frac{1}{|\mathbf{x}+\triangle|^3} \right) - \frac{3}{|\mathbf{x}|^5} \hat{\mathbf{d}} \cdot \mathbf{x} \otimes \mathbf{x} \cdot \hat{\mathbf{d}} + \frac{1}{|\mathbf{x}|^3} \right| \leq \frac{A_3}{|\mathbf{x}|^4} \tag{6.128}$$

for some constant $A_3 > 0$.

In light of Eq. (6.116), (6.121), (6.122) and (6.128), we conclude that for large enough R satisfying $\operatorname{diam} U + r < R < \infty$, and any $\mathbf{a}$, $\mathbf{b}$ satisfying $|\mathbf{a} - \mathbf{b}| > R$,

$$\left| L^{(r)}(\mathbf{a} - \mathbf{b}) \right| \leq \frac{C}{|\mathbf{x}|^4} \in L_1(\mathbb{R}^3 / B(R), \mathbb{R}). \tag{6.129}$$

That is, $\exists\ g_2(|\mathbf{x}|) \in L_1(\mathbb{R}^3/B(R), \mathbb{R})$, such that

$$\left| L^{(r)}(\mathbf{a} - \mathbf{b}) \right| \leq g_2(|\mathbf{x}|). \tag{6.130}$$

This completes Step (ii).

We complete the proof by combining Step (i) and Step (ii).

□

Lemma 10. *Let* $\mathbf{x}_1(\mathbf{y})$ *defined as corner map in Eq. (6.101), then*

$$|(\mathbf{x}_1(\mathbf{a}) - \mathbf{x}_2(\mathbf{b})) - (\mathbf{a} - \mathbf{b})| \leq 2\, diam\, U, \quad \forall \quad \mathbf{a}, \mathbf{b} \in \mathbb{R}^3. \tag{6.131}$$

Proof. From Fig. 6.3, we can see

$$\overrightarrow{\mathrm{AB}} + \overrightarrow{\mathrm{BC}} = \overrightarrow{\mathrm{AD}} + \overrightarrow{\mathrm{DC}}$$

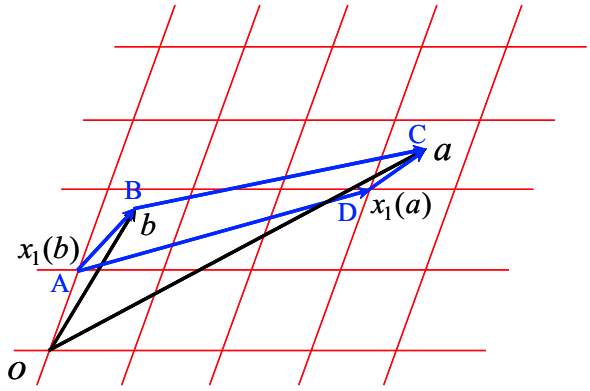

Figure 6.3: Corner map.

which implies

$$(\mathbf{b} - \mathbf{x}_1(\mathbf{b})) + (\mathbf{a} - \mathbf{b}) = (\mathbf{x}_1(\mathbf{a}) - \mathbf{x}_1(\mathbf{b})) + (\mathbf{a} - \mathbf{x}_1(\mathbf{a})),$$

or

$$(\mathbf{x}_1(\mathbf{a}) - \mathbf{x}_1(\mathbf{b})) - (\mathbf{a} - \mathbf{b}) = (\mathbf{b} - \mathbf{x}_1(\mathbf{b})) - (\mathbf{a} - \mathbf{x}_1(\mathbf{a})).$$

Therefore,

$$\begin{aligned} |(\mathbf{x}_1(\mathbf{a}) - \mathbf{x}_1(\mathbf{b})) - (\mathbf{a} - \mathbf{b})| &= |(\mathbf{b} - \mathbf{x}_1(\mathbf{b})) - (\mathbf{a} - \mathbf{x}_1(\mathbf{a}))| \\ &\leq |(\mathbf{b} - \mathbf{x}_1(\mathbf{b}))| + |(\mathbf{a} - \mathbf{x}_1(\mathbf{a}))| \\ &\leq 2 \operatorname{diam} U. \end{aligned}$$

□

Lemma 11. *Let $L^{(r)}$ be defined by Eq. (6.62), then*

$$\int_{\mathbb{R}^3} L^{(r)}(\mathbf{x}, \mathbf{y})\, d\mathbf{y} = \int_{\mathbb{R}^3} L^{(r)}(\mathbf{0}, \mathbf{y})\, d\mathbf{y}, \quad \forall \quad \mathbf{x} \in \mathbf{R}^3. \tag{6.132}$$

Proof. This proof follows James and Müller (1994) page 312-313. □

Chapter 7

Conclusion

Being non-polar (paraelectric) above their Curie temperature but spontaneously polarized (ferroelectric) below it, ferroelectric perovskites offer a tantalizing potential for applications: large actuation through domain switching and memory storage via switchable electric polarization. Oxygen vacancies, commonly present and mobile at high temperature, are the primary defects and thus play a central role in these applications. In this thesis, we have systematically investigated the role of oxygen vacancies in determining the properties and domain patterns of ferroelectric perovskites by developing a model that combines the ferroelectric and semiconducting nature of ferroelectric perovskites together. The key step – and departure from prior work – is to treat ferroelectric perovskites as polarizable semiconducting solids rather than polarizable dielectrics, with oxygen vacancies acting as n-type dopants.

The continuum theory developed in Chapter 3 provides a unified treatment of the ferroelectric and semiconducting nature of ferroelectric perovskites. This theory treats the polarization density, space charge density, dopant density and deformation as state variables, and derives their evolution/equilibrium laws consistent with second law of thermodynamics. This theory recovers the traditional theories of insulating ferroelectrics and nonpolarizable semiconductors in separate limits, but more importantly fully accounts for the interaction between these two aspects. It shows that the diffusion of oxygen vacancies depends on the domain pattern, the concentration as well as the choice of electrodes.

This theory is then used to study ferroelectric-electrode interface and domain walls through two-dimensional and one-dimensional simulations. It shows the formation of depletion layers – regions of enhanced space charges – at ferroelectric-electrode interfaces and the formation of space charge double layers at 90^o domain walls. These space charge dis-

tributions are accompanied by complicated internal electric fields which drive the diffusion of oxygen vacancies. The simulation results also show that the 180° domain walls have no significant electronic interaction. All of these provide important insight into various experimental observations concerning fatigue and domain wall pinning.

The formation of depletion layers at ferroelectric-electrode interfaces is shown in Fig. 5.7 and elaborated in Section 5.2. These layers and thus the propensity for failure depend on the choice of electrodes. This is consistent with the experimental observations (Burcsu, 2001; Scott, 2000). Further, it depends on dopant concentration. Greater the concentration, narrower the layers and higher the propensity for failure. Furthermore, at high temperature which may be present during deposition, the vacancies are mobile and tend to accumulate close to the electrodes (See Fig. 5.12 and Fig. 5.13). This promotes failure. Note that this persists even when the total oxygen vacancies are conserved. This has important consequences. Nuffer et al. (2001) studies the amount of oxygen released as a means of evaluating the role of oxygen vacancies in fatigue. Our results show that such an experiment would not probe an important aspect of fatigue.

We find that 180° domain walls are essentially uncharged, and have no electronic interaction with oxygen vacancies (See Figs. 5.7, 5.14, and Sections 5.1.2, 5.3.2.1 and 5.3.3 for detail). This is consistent with the low fatigue of SBT which has only 180° domain walls (Harnagea, 2001).

In contrast, 90° domain walls have a close interaction with space charges and oxygen vacancies. In a perfect crystal, a 90° domain wall has a voltage drop across it as shown in Figs. 5.6, 5.15 and 5.16. This drives the formation of a space charge double layer in a doped crystal (Fig. 5.7). In other words, 90° domain walls promote electronic charge injection and trapping. In turn, this can drive the diffusion of oxygen vacancies at high temperatures (See Figs. 5.17-5.22). This rearrangement gives a concrete mechanism for the domain memory observed by Ren (2004) and provides a potentially new mechanism for large electrostriction. Further, the formation of the space charge double layers means that 90° domain walls promote charge injection into the ferroelectric, and thus promote fatigue. Furthermore, the redistribution of oxygen vacancies near 90° domain walls may likely pin the domain walls and thus also promotes fatigue. Finally, all of these show that the two mechanisms – electronic charge injection and ionic charge trapping through oxygen vacancy diffusion – believed to be independent and the subject of some controversy (Scott, 2000;

Damjanovic, 1998; Shaw et al., 2000; Tagantsev et al., 2001) are in fact related.

Fig. 5.7 shows that the electronic and oxygen vacancies profile of 90^o domain walls is not symmetric (with respect to $\mathbf{p}$ to $-\mathbf{p}$). This implies that the transient conduction and capacitance across these domain walls is not symmetric. It would be interesting to verify this experimentally.

In the thesis, we have also extended the Lorentz calculation* of the energy due to a lattice of dipoles to a bi-lattice of charges. We find an interesting difference in the short range contribution: it does not vanish for a cubic lattice, instead a contribution reflecting the dipole is retained. This contribution is consistent with the symmetry of the bi-lattice. However, the long range contribution is identical in both situation.

This thesis also motivates various questions for the future. First, it motivates a systematic exploration of the transient conduction and evolution of leakage current under cyclic loading. The formation of depletion layers near electrodes and charge layers at 90^o domain walls shows that this is a nontrivial problem. Studying this problem will provide a better understanding of the evolution of fatigue. Second, it motivates experiments on the capacitance of domain walls and on aging at high temperatures. Finally, it motivates a detailed theoretical investigation of the definition of polarization and issues related to surface charges.

*This calculation was made rigorous by James (2002)

Bibliography

Ahluwalia, R. and Cao, W. (1991). Computer simulation of domain pattern formation in ferroelectrics. In Krakauer, H., editor, *Fundamental Physical Ferroelectrics, Proceedings of AIP Conference on Fundamental Physics of Ferroelectrics*, pages 185–190.

Ahluwalia, R. and Cao, W. (2001). Size dependence of domain patterns in a constrained ferroelectric system. *J. Appl. Phys.*, 89(12):8105–9109.

Arias, I., Serebrinsky, S., and Ortiz, M. (2004). A cohesive model of fatigue of ferroelectric materials under electro-mechanical cyclic loading. In Lagoudas, D. C., editor, *Proceedings of the SPIE Conference on Smart Structure and Materials 2004*, volume 5387, pages 371–378.

Ascher, U. and Russell, R. D. (1981). Reformulation of boundary value problems in "standard" form. *SIAM Review*, 23(2):238–254.

Ashcroft, N. W. and Mermin, N. D. (1976). *Solid State Physics*. Harcourt College Publishers.

Bobbio, S. (2000). *Electrodynamics of Materials: Forces, Stresses, and Energies in Solids and Fluids*. Academic Press, San Diego.

Bornand, V., Trolier-Mckinstry, S., Takemura, K., and Randall, C. A. (2000). Orientation dependence of fatigue behavior in relaxor ferroelectric-$PbTiO_3$ thin films. *J. Appl. Phys.*, 87(8):3965–3972.

Bratkovsky, A. M. and Levanyuk, A. P. (2000). Ferroelectric phase transitions in films with depletion charge. *Physical Review B*, 61(22):15042–15050.

Brennan, C. (1993). Model of ferroelectric fatigue due to deffect/domain interaction. *Ferroelectrics*, 150:199–208.

Brown, W. F. J. (1966). *Magnetoelastic Interactions*. Springer Tracts in Natural Philosophy, (ed. by C. Truesdell), Springer-Verlag, Berlin.

Burcsu, E. (2001). *Investigation of Large Strain Actuation in Barium Titanate*. PhD thesis, California Institute of Technology.

Burcsu, E., Ravichandran, G., and Bhattacharya, K. (2000). Large strain electrostrictive actuation in barium titanate. *Appl. Phys. Lett.*, 77(11):1698–1700.

Burcsu, E., Ravichandran, G., and Bhattacharya, K. (2004). Large electrostrictive actuation of barium titanate single crystals. *Journal of the Mechanics and Physics of Solids*, 52:823–846.

Calleja, M., Dove, M. T., and Salje, E. K. H. (2003). Trapping of oxygen vacancies on twin walls of $CaTiO_3$: A computer simulation study. *Journal of Phyics: Condensed Matter*, 15:2301–2307.

Cao, W. and Cross, L. E. (1991). Theory of tetragonal twin structures in ferroelectric perovskites with a first-order phase transition. *Physical Review B*, 44(1):5–12.

Chen, L.-Q. and Shen, J. (1998). Applications of semi-implicit fourier-spectral method to phase field equations. *Computer Physics Communications*, 108:147–158.

Cillessen, J. F. M., Prins, M. W. J., and Wolf, R. M. (1997). Thickness dependence of the switching voltage in all-oxide ferroelectric thin-film capacitors prepared by pulsed laser deposition. *J. Appl. Phys.*, 81(6):2777–2783.

Coleman, R. D. and Noll, W. (1963). The thermodynamics of elastic materials with heat conduction and viscosity. *Arch. Rational Mech. Anal.*, 13(3):167–178.

Colla, E. L., Taylor, D. V., Tagantsev, A. K., and Setter, N. (1998). Discrimination between bulk and interface scenarios for the suppression of the switchable polarization (fatigue) in Pb(Zr, Ti)O_3 thin films capacitors with Pt electrodes. *Appl. Phys. Lett.*, 72(19):2478–2480.

Damjanovic, D. (1998). Ferroelectric, dielectric and piezoelectric properties of ferroelectric thin films and ceramics. *Rep. Prog. Phys.*, 61:1267–1324.

De Araujo, C. A. P., Cuchiaro, J. D., et al. (1995). Fatigue-free ferroelectric capacitors with platinum electrodes. *Nature*, 374(6523):627–629.

DeSimone, A. and James, R. D. (2002). A constrained theory of magnetoelasticity. *Journal of the Mechanics and Physics of Solids*, 50:283–320.

DeSimone, A. and Podio-Guidugli, P. (1996). On the continuum theory of deformable ferromagnetic solids. *Arch. Rational Mech. Anal.*, 136:201–233.

Devonshire, A. F. (1949a). Theory of barium titanate: Part 1. *Phylosophical Magazine*, 40(309):1040–1063.

Devonshire, A. F. (1949b). Theory of barium titanate: Part 2. *Phylosophical Magazine*, 42(333):1065–1079.

Devonshire, A. F. (1954). Theory of ferroelectrics. *Advances in Physics*, 3(10):85–130.

Du, X. and Chen, I.-W. (1998). Model experiments on fatigue of $Pb(Zr_{0.53}Ti_{0.47})O_3$ ferroelectric thin films. *Appl. Phys. Lett.*, 72(15):1923–1925.

Egami, T., Dmowski, W., Teslic, S., Davies, P. K., Chen, I. W., and Chen, H. (1998). Nature of atomic ordering and mechanism of relaxor ferroelectric phenomena in PMN. *Ferroelectrics*, 206:231–244.

Egami, T., Teslic, S., Dmowski, W., Viehland, D., and Vakhrushev, S. (1997). Local atomic structure of relaxor ferroelectric solids determined by pulsed neutron and X-ray scattering. *Ferroelectrics*, 199:103–113.

Ericksen, J. L. (1984). The Cauchy and Born hypothesis for crystals. In Gurtin, M. E., editor, *Phase Transformation and Material Instabilities in Solids*, pages 61–78.

Gunton, J. D., San Miguel, M., and Sahni, P. S. (1972). *Phase transitions and Critical Phenomena*, volume 8, chapter The Dynamics of First-Order Phase Transitions. Academic Press.

Gütter, B., Bismayer, U., Groves, P., and Salje, E. K. H. (1995). Fatigue mechanism in thin film PZT memory materials. *Semicond. Sci. Technol.*, 10:245–248.

Harnagea, C. (2001). *Local Piezoelectric Response and Domain Structures in Ferroelectric Thin Films Investigated by Voltage-Modulated Force Microscopy.* PhD thesis, Martin-Luther-Universität Halle Wittenberg.

He, L. and Vanderbilt, D. (2003). First-principle study of oxygen-vacancy pinning of domain walls in $PbTiO_3$. *Physical Review B*, 68:134103(1–7).

Hu, H.-L. and Chen, L.-Q. (1997). Computer simulation of 90^o ferroelectric domain formation in two-dimensions. *Materials Science and Engineering*, A238:182–191.

James, R. D. (2002). Configurational forces in magnetism with application to the dynamics of a small-scale ferromagnetic shape memory cantilever. *Continuum Mech. Thermodyn.*, 14:55–86.

James, R. D. and Kinderlehrer, D. (1990). Frustration in ferromagnetic materials. *Continuum Mech. Thermodyn.*, 2:215–239.

James, R. D. and Müller, S. (1994). Internal variables and fine-scale oscillations in micromagnetics. *Continuum Mech. Thermodyn.*, 6:291–336.

Jang, J. H. and Yoon, K. H. (1999). Electric fatigue properties of sol-gel-derived $Pb(Zr,Ti)O_3/PbZrO_3$ multilayered thin films. *Appl. Phys. Lett.*, 75(1):130–132.

Jona, F. and Shirane, G. (1993). *Ferroelectric Crystals.* Dover Publications, New York.

Kim, S.-J. and Jiang, Q. (1996). Microcracking and electric fatigue of polycrystalline ferroelectric ceramics. *Smart Mater. Strut.*, 5:321–326.

King-Smith, R. D. and Vanderbilt, D. (1994). First-principles investigation of ferroelectricity in perovskite compounds. *Physical Review B*, 49(9):5828–5844.

Larsen, P. K., Dormans, G. J. M., Taylor, D. J., and van Veldhoven, P. J. (1994). Ferroelectric properties and fatigue of $Pb(Zr_{0.51}Ti_{0.49})O_3$ thin films of varying thickness: Blocking layer model. *J. Appl. Phys.*, 78(4):2405–2413.

Lorentz, H. A. (1952). *The Theory of Electrons.* Dover Publications, New York.

Lynch, C. S. (1998). Fracture of ferroelectric and relaxor electro-ceramics: Influence of electric field. *Acta Mater.*, 46(2):599–608.

Lynch, C. S., Chen, L., Suo, Z., McMeeking, R. M., and Yang, W. (1995). Crack growth in ferroelectric ceramics driven by cyclic polarization switching. *Journal of Intelligent Material Systems and Structures*, 6:191–198.

McMeeking, R. M. (2001). Towards a fracture mechanics for brittle piezoelectric and dielectric materials. *Int. J. Fracture*, 108(1):25–41.

Mitrović, D. and Žubrinić, D. (1998). *Fundamentals of Applied Functional Analysis*. Addison Wesley Longman Limited.

Mitsui, T., Hellwege, K. H., and Hellwege, A. M. (1981). Ferroelectric and related substances. In *Landolt-Boernstein Numerical Data and Functional Relationships in Science and Technology, New Series, Group III, Crystal and Solid State Physics*, volume 16A.

Moulson, A. and Herbert, J. (2003). *Electroceramics : Materials, Properties, Applications*. John Wiley & Sons, 2nd edition.

Nagaraj, B., Aggarwal, S., and Ramesh, R. (2001). Influence of contact electrodes on leakage characteristics in ferroelectric thin films. *J. Appl. Phys.*, 90(1):375–382.

Nuffer, J., Lupascu, D. C., Rödel, J., and Schroeder, M. (2001). Negligible oxygen liberation during bipolar electric cycling of ferroelectric lead zirconate titanate ceramics. *Appl. Phys. Lett.*, 79(22):3675–3677.

Padilla, J., Zhong, W., and Vanderbilt, D. (1996). First-principles investigation of 180^o domain walls in $BaTiO_3$. *Phyical Review B: Rapid Communications*, 53:R5969–R5973.

Park, S. B. and Sun, C. T. (1995). Fracture criteria for piezoelectric ceramics. *J. Am. Ceram. Soc.*, 78(6):1475–1480.

Park, S. E. and Shrout, T. R. (1997). Ultrahigh strain and piezoelectric behavior in relaxor based ferroelectric single crystals. *J. Appl. Phys.*, 82(4):1804–1811.

Porter, D. A. and Easterling, K. E. (1981). *Phase Transformations in Metals and Alloys*. Van Nostrand Reinhold (UK) Co.

Ramesh, R., Chan, W. K., Wilkens, B., et al. (1992). Fatigue and retention in ferroelectric Y-Ba-Cu-O/Pb-Zr-Ti-O/Y-Ba-Cu-O heterostructures. *Appl. Phys. Lett.*, 61(13):1537–1539.

Ren, X. (2004). Large electric-field-induced strain in ferroelectric crystals by point-defect-mediated reversible domain switching. *Nature Materials*, 3(2):91–94.

Resta, R. (1994). Macroscopic polarization in crystalline dielectrics: the geometric phase approach. *Review of Modern Physics*, 66(3):899–915.

Sanchez, L. E., Dion, D. T., Wu, S. Y., and Naik, I. K. (1991). Processing and characterization of sol-gel derived very thin film ferroelectric capacitors. *Ferroelectrics*, 116:1–17.

Schlömerkemper, A. (2002). *Magnetic Forces in Discrete and Continous Systems*. PhD thesis, Universität Leipzig.

Scott, J. F. (2000). *Ferroelectric Memories*. Springer.

Scott, J. F., Araujo, C. A., Melnick, B. M., McMillan, L. D., and Zuleeg, R. (1991). Quantititative measurement of space-charge effects in lead zirconate-titanate memories. *J. Appl. Phys.*, 70(1):382–388.

Scott, J. F., Watanabe, K., Hartmann, A. J., and Lamb, R. N. (1999). Device models for PZT/Pt, BST/Pt, SBT/Pt, and SBT/Bi ferroelectric memories. *Ferroelectrics*, 225:83–90.

Shaw, T. M., Trolier-Mckinstry, S., and McIntyre, P. C. (2000). The properties of ferroelectric films at small dimensions. *Annu. Rev. Mater. Sci.*, 30:263–298.

Shenoy, V. B. and Bhattacharya, K. (2004). Effect of doping on polarization profile and switching in ferroelectric thin films. *to be submitted*.

Shilo, D., Ravichandran, G., and Bhattacharya, K. (2004). Investigation of twin-wall struture at the nanometre scale using atomic force microscopy. *Nature Materials*, 3:453–457.

Shu, Y. C. and Bhattacharya, K. (2001). Domain patterns and macroscopic behavior of ferroelectric materials. *Phylosophical Magazine B*, 81(12):2021–2054.

Solymar, L. and Walsh, D. (1984). *Lectures on the Electrical Properties of Materials*. Oxford University Press, 3rd edition.

Stein, E. M. (1970). *Singular Integrals and Differentiability Properties of Functions*. Princeton University Press, Princeton.

Strukov, B. A. and Levanyuk, A. P. (1998). *Ferroelectric Phenomena in Crystals: Physical Foundations*. Springer.

Sze, S. M. (1981). *Physics of Semiconductor Devices*. Wiley, 2nd edition.

Tagantsev, A. K., Landivar, M., Colla, E., and Setter, N. (1995a). Identification of passive layer in ferroelectric thin films from their switching parameters. *J. Appl. Phys.*, 78(4):2623–2630.

Tagantsev, A. K., Pawlaczyk, C., Brooks, K., M., L., Colla, E., and Setter, N. (1995b). Depletion and depolarizing effects in ferroelectric thin films and their manifestations in switching and fatigue. *Integrated Ferroelectrics*, 6:309–320.

Tagantsev, A. K., Stolichnov, I., Colla, E. L., and Setter, N. (2001). Polarization fatigue in ferroelectric films: Basic experimental findings, phenomenological scenarios, and microscopic features. *J. Appl. Phys.*, 90(3):1387–1402.

Tiersten, H. F. (1990). *A Development of the Equations of Electromagnetism in Material Continua*. Springer Tracts in Natural Philosophy 36, (ed. by C. Truesdell), Springer-Verlag, New York.

Toupin, R. A. (1956). The elastic dielectric. *J. Rational Mech. Anal.*, 5:849–915.

Warren, W. L., Dimos, D., et al. (1994). Electronic domain pinning in Pb(Zr,Ti)O_3 thin films and its role in fatigue. *Appl. Phys. Lett.*, 65(8):1018–1020.

Warren, W. L., Dimos, D., et al. (1995). Polarization suprresion in Pb(Zr,Ti)O_3 thin filmes. *J. Appl. Phys.*, 77(12):6695–6702.

Waser, R. (1991). Bulk conductivity and defect chemistry of acceptor-doped strontium-titanate in the quenched state. *Journal of The American Ceramic Society*, 74(8):1934–1940.

Watanabe, Y. (1998a). Theoretical investigation of the thickness effect of ferroelectric incorporating semiconducting properties. *Applied Surface Science*, 130-132:610–615.

Watanabe, Y. (1998b). Theoretical stability of the polarization in a thin semiconducting ferroelectric. *Physical Review*, 57(2):789–804.

Watanabe, Y. (1998c). Theoretical stability of the polarization in insulating ferroelectric/semiconductor structures. *J. Appl. Phys.*, 83(4):2179–2193.

Watanabe, Y. and Sawamura, D. (1997). Thermodynamics stability of the spontaneous polarization and the space charge layer in ferroelectric/semiconductor heterostructures. *Jpn. J. Appl. Phys.*, 36:6162–6166.

Wheeden, R. D. and Zygmund, A. (1977). *Measure and Integral: An Introduction to Real Analysis*. Marcel Dekker, Inc.

Wittborn, J., Canalias, C., Rao, K. V., et al. (2002). Nanoscale imaging of domains and domain walls in periodically poled ferroelectrics using atomic force microscopy. *Appl. Phys. Lett.*, 80(9):1622–1624.

Zhang, Q. (2004a). *private discussion*.

Zhang, R. (2004b). *in preparation*.

Zhang, W. and Bhattacharya, K. (2003). Modeling large strain eletrostriction of ferroelectrics under combined electromechanical loads. In Lagoudas, D. C., editor, *Proceedings of the SPIE Conference on Smart Structure and Materials 2003*, volume 5053.

Zhang, W. and Bhattacharya, K. (2004a). A computational model of ferroelectric domains. part I: Model formulation and domain switching. *Acta Mater.*, in press.

Zhang, W. and Bhattacharya, K. (2004b). A computational model of ferroelectric domains. part II: Grain boundaries and defect pinning. *Acta Mater.*, in press.

Zhu, T. and Yang, W. (1999). Fatigue crack growth in ferroelectrics driven by cyclic electric loading. *Journal of the Mechanics and Physics of Solids*, 47(1):81–97.